MECHANICAL RESPONSE OF POLYETHER POLYURETHANE FOAMS UNDER MULTIAXIAL STRESS AND THE INITIAL YIELDING OF ULTRATHIN FILMS

BY

XIANGYU DAI

DISSERTATION

Submitted in partial fulfillment of the requirements
for the degree of Doctor of Philosophy in Theoretical and Applied Mechanics
in the Graduate College of the
University of Illinois at Urbana-Champaign, 2010

Urbana, Illinois

Doctoral Committee:

Associate Professor Gustavo Gioia, Chair, Director of Research
Professor Nancy Sottos
Professor James W. Phillips
Assistant Professor Amy Wagoner Johnson

Abstract

In the first part of this thesis, we study the mechanical response of elastic polyether polyurethane (EPP) foams by means of experiments, theory, and modeling. The experiments include five loading cases: uniaxial compression along the rise direction; uniaxial compression along two mutually perpendicular transverse directions; uniaxial tension along the rise direction; shear combined with compression along the rise direction; and hydrostatic pressure combined with compression along the rise direction. We use a commercial series of five EPP foams of apparent densities (mass per unit volume of foam) 50.3, 63.0, 77.0, 162.9 and 220.5 $\mathrm{kg/m^3}$. We perform a test for each foam in the series and each loading case. In every test we measure the mechanical response in the form of a stress–strain curve or a force–displacement curve; in several tests we use a Digital Image Correlation (DIC) technique to compute the strain fields on the surface of the specimen.

For some loading cases, including uniaxial compression along the rise direction, the mechanical response of the three foams of lower density exhibits a stress plateau. This stress plateau has been commonly interpreted as a manifestation of a bifurcation of equilibrium (Euler buckling of the microstruture of the foam), a global phenomenon that encompasses the entire microstructure of the foam at once. In this interpretation, the plateau stress (i.e., the value of stress on the stress plateau) is the eigenvalue associated with the bifurcation of equilibrium. Nevertheless, our experimental results indicate that a stress plateau is invariably accompanied by heterogeneous, two-phase strain fields, consistent with the occurrence of a configurational phase transition. Thus we argue that the plateau stress is the Maxwell stress associated with the attainment of a limit point (snap-through buckling of a cell of the foam), a local phenomenon which progressively sweeps through the microstructure of the foam.

For other loading cases, including uniaxial compression along a transverse direction, the mechanical response does not exhibit a stress plateau, and the stress-strain curves harden monotonically regardless of the density of the foam. The strain fields remain homogeneous, even for the least dense foam.

We use our experimental results to calibrate a mean-field model of EPP foams. In this model, a unit cell composed of several bars is cut off from an idealized, perfectly periodic foam microstrusture. The tips of the bars of the cell are subjected to a set of displacements affine with the applied mean deformation

gradient, and left to rotate freely. The unit cell is characterized using a few physically meaningful material and geometric parameters whose values may be readily estimated for any given foam.

We verify that under uniaxial loading the model predicts configurational phase transitions, stress plateaus, and two-phase fields for low-density foams; a critical point for foams of a critical density; and monotonically hardening stress-strain curves for foams of density higher than the critical density. The critical exponents associated with the critical point are the same as in other mean-field models such as the Van der Walls model of a fluid.

With a suitable choice of parameters, the model gives predictions that compare favorably with our experimental results for all loading cases. In particular, the model gives a nonconvex strain energy function where (and only where) the experiments exhibit a stress plateau and two-phase strain fields.

We conclude that the mechanical response of EPP foams is dominated at large strains by either one of two mechanisms at the level of a foam cell: snap-through buckling, which leads to nonconvex strain energy functions, stress plateaus, and two-phase strain fields; or bending, which leads to convex strain energy functions, monotonically increasing stresses, and homogeneous strain fields.

This conclusion allows us to interpret an extensive series of experiments in which EPP foam specimens are penetrated with a wedge-shaped punch. For low-density foams, we find experimentally that the mechanical response is linear up to a penetration of the punch of about 40% of the height of the specimen. We surmise that the strain field in the specimen consists of a high-strain phase in a region close to the tip, where a phase transition has taken place, and a low-strain phase in a region far from the tip, where the phase transition is yet to take place. The two regions are separated by a sharp interface, where the strain is discontinuous. We use DIC to trace the sharp interface as it grows and sweeps through the specimen during a test.

By studying theoretically the self-similar growth of a sharp interface, we predict a linear response within the self-similar regime, in accord with our experimental findings. We then apply the same theory to the case of a conical punch, predict a quadratic response within the self-similar regime, and verify our prediction by performing experiments with a conical punch. We conclude that in the self-similar regime the mechanical response is ruled entirely by geometry and depends only on the dimensionality of the punch and the plateau stress of the low-density foam.

In the second part of this thesis, we study the initial yielding of ultrathin metallic films (thickness of a fraction of a μm). Recent experiments indicate that in free-standing metallic films of constant grain size the initial yield stress increases as the film becomes thinner, it peaks for a thickness on the order of 100 nm, and then starts to decrease. This reversing (first hardening, then softening) size effect poses two challenges: (1) It cannot be explained using currently available models and (2) it appears to contradict the little-known

but remarkable experimental results of J. W. Beams [1959], in which the size effect in bulge tests did not reverse even for a thickness of 20 nm.

We show that the reversing size effect can be explained and the contradiction dispelled by taking into account the effect of the surface stress on the initial yielding. We also predict that the mode of failure of a film changes from ductile to brittle for a thickness on the order of 100 nm, in accord with experiments. Our successful application of methods of continuum mechanics to films as thin as 100 times a typical lattice parameter adds to a growing realization of the robustness of these methods at ultrasmall length scales.

To Father and Mother.

Acknowledgments

This research would not have been possible without the support of many people. I thank my advisor, Prof. Gustavo Gioia for his guidance and support throughout my graduate study. His knowledge and wisdom inspired me in every step of this research. I thank Prof. James W. Phillips for providing me with some experimental equipment and much valuable advice. I thank my groupmate Tapan Sabuwala for his precious help with the numerical simulations, and Prof. Scott M. Olson and his student Abouzar Sadrekarimi for their help with the triaxial test.

The financial support from the National Science Foundation under grant CMS-0092849 (Ken P. Chong, program director) is acknowledged with gratitude. The General Plastics Manufacturing Company donated the foam specimens and the National Center for Supercomputing Applications granted access to the finite element packages ABAQUS and PATRAN.

Last but not least, I thank my wife, parents, brother and numerous friends who accompanied me in this long process, always offering support and love.

Table of Contents

List of Tables . . . . . **ix**

List of Figures . . . . . **x**

Part I Mechanical response of polyether polyurethane foams under multiaxial stress . . . **1**

Chapter 1 Introduction **2**
1.1 Microstructure of foams 3
1.2 Foam mechanics 5
1.3 Elastic Polyether Polyurethane foams under uniaxial compressive loading along the rise direction 6
1.4 Statement of the major goals of this research 10

Chapter 2 Uniaxial mean-field models and the critical point **12**
2.1 Introduction 12
2.2 A simplified mean-field model 13
2.3 Critical exponents 19
2.3.1 Critical exponents for the simplified mean-field model 20
2.3.2 Critical exponents for a Kármán-beam mean-field model 22
2.4 Discussion 23

Chapter 3 Experiments **26**
3.1 Introduction 26
3.2 Experimental set-ups 28
3.2.1 Error estimation 29
3.3 Mullins effect 30
3.4 Global digital image correlation and its applications to foams 32
3.4.1 Translation calibration test 34
3.4.2 Rotation calibration test 35
3.4.3 A translation test performed on our experimental setup 36
3.5 Experimental results 37
3.5.1 Uniaxial compression along the rise direction 37
3.5.2 Uniaxial compression along transverse directions 43
3.5.3 Tension 45
3.5.4 Combined compression and shear loading 47
3.5.5 Triaxial testing 52
3.6 The bulging of foam specimens elucidated via the global DIC method 53
3.7 Discussion 57

Chapter 4 A 3D mean-field model of EPP foams . . . 59
4.1 Introduction . . . 59
4.2 Formulation . . . 60
4.2.1 Geometry of the model . . . 60
4.2.2 Parameters of the model . . . 61
4.2.3 Boundary conditions . . . 62
4.2.4 Computational implementation . . . 62
4.3 Calibration . . . 63
4.3.1 Calibration criteria . . . 63
4.3.2 Calibration parameters . . . 64
4.3.3 Uniaxial compression along the rise direction . . . 64
4.3.4 Uniaxial compression along the transverse directions . . . 66
4.3.5 Shear combined with compression along the rise direction . . . 69
4.3.6 Uniaxial tension along the rise direction . . . 71
4.3.7 Triaxial loading . . . 72
4.4 Discussion . . . 74

Chapter 5 Punching elastic foams in the self-similar regime . . . 77
5.1 Introduction . . . 77
5.2 Experimental set-up . . . 77
5.3 Wedge punching test . . . 79
5.4 The self-similar regime . . . 80
5.4.1 Strain fields and the mechanical behavior of foam cells . . . 80
5.4.2 The self-similar regime . . . 81
5.4.3 Observation of the sharp interface via global DIC . . . 84
5.4.4 The self-similar regime and the plateau stress . . . 85
5.4.5 Predictions for the self-similar regime . . . 87
5.5 Conical punching test . . . 90
5.6 Discussion . . . 93

***Part II Initial yielding of ultrathin films* . . . 94**

Chapter 6 Surface stress and reversing size effect in the initial yielding of ultrathin films 95
6.1 Introduction . . . 95
6.2 Surface stress . . . 97
6.3 The surface stress in thin films . . . 98
6.4 Apparent yield stress . . . 99
6.4.1 Size effects and the yield condition . . . 102
6.4.2 Comparison with experiments . . . 103
6.4.3 A note on the values of the surface stress used in the comparison with experiments . . . 104
6.5 Failure and the ductile-to-brittle transition . . . 105
6.6 Biaxial loading . . . 108
6.7 Discussion . . . 109

Chapter 7 Summary and conclusions . . . 111

References . . . 117

List of Tables

3.1 Measured Young's modulus for each specimen 32
3.2 The applied and measured horizontal displacement 35
3.3 The rotation angle measured with global DIC 35
3.4 Vertical displacements measured with Global DIC and the transducer 36

4.1 The cross sectional area A for different foams 64

List of Figures

1.1 SEM microphotographs of two cross sections in an EPP foam of measured apparent density $\rho_a = 51.6\,\mathrm{kg/m^3}$ (General Plastics EF-4003). a) Section parallel to the rise direction. b) Section normal to the rise direction. (Sabuwala, Dai, and Gioia, unpublished.) 3

1.2 Typical idealized microstructures. a) An hexagonal honeycomb. b) Five tetrakaidecahedrons (Laroussi et al., 2002). 4

1.3 Mechanical response of the low-density EPP foam of Fig. 1.1 subject to uniaxial compressive stretch along the rise direction (Gioia et al., 2001). A stretch $\lambda = 1$ corresponds to the undeformed geometry, whereas stretches $\lambda < 1$ correspond to compressed geometries. 6

1.4 Typical displacement field on the surface of a low-density foam. Measured during the uniaxial test that gave the stress–stretch curve of Fig. 1.3 (Gioia et al., 2001). The foam is the low-density EPP foam of Fig. 1.1, and the applied average stretch is $\bar{\lambda} = 0.74$, within the stress plateau of Fig. 1.3. The surface shown in the figure is $3.72\,\mathrm{cm} \times 2.54\,\mathrm{cm}$, and the height of $2.54\,\mathrm{cm}$ is aligned with the rise direction, which coincides with the X-axis and the direction of loading. The units of X and Y are pixels, and the geometry is the underformed geometry. The displacement field is given in the form of a contour plot. Each contour in the figure corresponds to a constant value of the displacement u_X in the rise direction. The value of u_X on any given contour differs by a fixed increment from the value of u_X on an adjacent contour. The contours in the figure indicate the existence of two preferred values of $\partial u_X/\partial X$, which correspond to two characteristic values of stretch and two configurational phases of the microstructure of the foam (Gioia et al., 2001). 7

1.5 Snap-through buckling of the microstructure of Fig. 1.1 (Gioia et al., 2001). Stretching is along the rise direction, which in this figure is the vertical direction. The sequence goes from left to right and top to bottom. The cells appear to be equiaxed (cf. Fig. 1.1b) because the line of view is not perpendicular to the rise direction. 9

2.1 The simplified mean-field model of EPP foams. (a) Undeformed network of bars. (b) A four-bar cell. (c) For uniaxial stretch along the rise direction, the four-bar cell may be thought of as a two-bar cell. 14

2.2 (a) The stress-stretch curve for a low-density foam. (b) The attendant energy curve, which is nonconvex. 16

2.3 The stretch distribution in a low-density foam specimen. (a) Original geometry of the specimen. (b) Current geometry of the specimen; $\bar{\lambda}$ is the applied average stretch. (C) Two-phase stretch distribution in the specimen. 16

2.4 The network of bars before and after buckling. (a) The low-density phase L (schematic). (b) The high-density phase H 16

2.5 Stress-stretch curves. The dashed grey lines are experimental data from (Gioia et al., 2001). These data are for six EPP foams of measured apparent densities ρ_a=51.6, 57.7, 80.2, 159, 219 and 280 kg/m^3. The calculate the relative densities rho, we use $\rho_s = 1700\,\mathrm{kg/m^3}$ (for the 3 foams of lower density) or $\rho_s = 2200\,\mathrm{kg/m^3}$ (for the 3 foams of higher density). The specimens have a cross-section of 10.2 cm × 10.2 cm, and a height of 5.08 cm. The solid black lines are predicted from (2.6) and (2.9). For the foams of density lower than the critical density (i.e., for the low-density foams), the predicted mechanical reponse has been properly convexified in accord with the Erdman equilibrium eq. (2.12), so that the stress-stretch curves display the stress plateaus. 18
2.6 (a) λ_L and λ_H in a region very close to the critical point. (b) $\lambda_L - \lambda_H$ vs. $|\rho - \rho_c|$ in log-log scale. 20
2.7 (a) $\sigma - \sigma_c$ vs. $\lambda - \lambda_c$ for $\rho = \rho_c = 0.05507$ and $0.76 \le \lambda \le 0.86$. (b) $|\sigma - \sigma_c|$ vs. $|\lambda - \lambda_c|$ in log-log scale. 21
2.8 $-\frac{1}{\lambda}\frac{\partial \lambda}{\partial \sigma}$ vs. $|\rho - \rho_c|$ in log-log scale. 22
2.9 (a) λ_H and λ_L in a region very close to critical point. (b) $\lambda_H - \lambda_L$ vs. $\rho - \rho_c$ in log-log scale. 22
2.10 (a) $\sigma - \sigma_c$ vs. $\lambda - \lambda_c$ for $\rho = \rho_c = 0.05507$ and $0.76 \le \lambda \le 0.86$. (b) $|\sigma - \sigma_c|$ vs. $|\lambda - \lambda_c|$ in log-log scale. 23

3.1 ATS testing machine setup 28
3.2 (a) Photograph of the TurePath Automated Stress Path System. (b) Sketch of the TurePath Automated Stress Path System. 29
3.3 Stress-strain curves of 6 load-unload cycles, for an EPP foam of relative density $\rho = 0.046$ subjected to uniaxial compression along the rise direction. 31
3.4 The modulus of foams specimens vs. the density 32
3.5 The foam specimen and the frame for global DIC 34
3.6 Axial stress vs. axial strain curves of foam specimens of five densities under uniaxial compression along the rise direction. 38
3.7 Axial stress vs. axial strain curve of the low density foam specimen under uniaxial compression along the rise direction. 39
3.8 Contours of displacement along the rise direction for the foam of lower density. 40
3.9 Plots of displacements in y direction of points on the foam surface along the dashed line drawn in Fig. 3.8a, corresponding to strain values of point A to F in Fig. 3.7. 41
3.10 Axial stress vs. axial strain curve of the high density foam specimen under uniaxial compression along the rise direction. 42
3.11 Contours of displacement along the rise direction for the foam of higher density under uniaxial compression along the rise direction. 42
3.12 Axial stress vs. axial strain of foam specimens of five densities for uniaxial compression along one of the transverse direction 43
3.13 Axial stress vs. axial strain of the least dense foam specimen for uniaxial compression along the rise and transverse directions. 44
3.14 Displacement field for compression along the transverse direction. 45
3.15 (a) Tension test specimen and set up. (b) Sketch of the set up. 46
3.16 Axial stress vs. axial strain of foam specimens of five densities for uniaxial tension along the rise direction. 46
3.17 (a) Compression loading test set-up. (b) Sketch of the set up 47
3.18 Vertical force vs. vertical displacement for foam specimens of five different densities for the compression and shear combined loading. 48
3.19 Vertical force vs. vertical displacement curves for specimens with dimensions 10 cm × 10 cm × 10 cm and 10 cm × 10 cm × 5 cm, subjected to compression and shear combined loading. The displacement is normalized by dividing the specimen height. 49
3.20 Displacement field for compression and shear combined loading of low density foam specimen of size 10 cm × 10 cm × 10 cm 50

3.21 Plots of displacements in the y direction of points on the foam surface along the dashed line drawn in Fig. 3.20b, corresponding to strain values of point A to F in Fig. 3.19. 50
3.22 Vertical force vs. vertical displacement curves for triaxial loading 51
3.23 The bulging that occurs during uniaxial compression of a foam specimen of density $50.3\,\mathrm{kg/m^3}$ and dimensions $10\,\mathrm{cm} \times 10\,\mathrm{cm} \times 10\,\mathrm{cm}$. The pictures in (a) to (e) are the deformed foam surface at average stretch (the height of the deformed specimen divided by the original height) of 1 (undeformed), 0.910, 0.790, 0.701, 0.591 and 0.481, respectively 54
3.24 The foam specimen and the finite element mesh used for global DIC. 54
3.25 The deformed mesh calculated with global DIC. Figures (a) to (e) correspond to the deformed foam surfaces (a) to (e) in Fig. 3.23, respectively 55
3.26 Contours of constant displacement in the loading direction. The displacement of one contour differs from the displacement of a contiguous contour by 0.1 cm; the displacement of some of the contours are marked (in cm). The contour plot (a) to (e) corresponds to the deformed foam surface (a) to (e) of Fig. 3.23 respectively 56

4.1 The idealized foam representative microstructure. (a) 3D view of the foam microstructure. (b) Front view. (c) Side view. (d) Top view. 60
4.2 The boundary faces of the substructure 62
4.3 The deformed substructure under uniaxial loading along the rise direction (a) Front view. (b) Side view 66
4.4 The experimental and predicted response of foam specimens for uniaxial compression along the rise direction 67
4.5 The deformed substructure under uniaxial loading along the transverse direction (a) Top view. (b) Side view 68
4.6 The experimental and predicted response of foam specimens for uniaxial compression along one of the transverse direction 69
4.7 The deformed substructure under uniaxial loading along the transverse direction (a) Front view. (b) Side view 70
4.8 The experimental and predicted response of foam specimens for Compression-shear combined loading 71
4.9 The experimental and predicted response for uniaxial tension along the rise direction 72
4.10 The normalized axial stress vs axial strain curves for the triaxial loading case (a) For specimen with relative density $\rho = 0.038$. (b) For specimen with relative density $\rho = 0.046$. (c) For specimen with relative density $\rho = 0.065$. (ed) For specimen with relative density $\rho = 0.086$. . 73

5.1 Experimental setup for wedge-punching 78
5.2 Plots of the force vs. the penetration displacement measured in five experiments with the wedge-shaped punch. (a) The three experiments correspond to foams of low densities ($EF-4003, EF-4004, EF-4005$). (b) The two experiments correspond to foams of high densities ($TF5070-10$ and $TF5070-13$). For comparison, the height of the specimen is 10 cm. . . . 79
5.3 Schematic of a strain field with a smooth transition from a high strain close to the tip of the punch to a low strain far from the tip. 80
5.4 Microphotographs of an array of cells in a polyether polyurethane foam and the cap of a shampoo bottle. The cap and a foam cell are examples of bi-stable elastic structures. (a) Plane perpendicular to the rise direction. (b) Plane parallel to the rise direction. (c) An Idealized array of cells. (d) The array of cells after snap-through buckling. (e) Closed cap. (f) Open cap. 82
5.5 Schematic strain field with a sharp transition. (a) 3-D view. (b) Front view. As the penetration increases, the radius of the sharp interface increases proportionally. 82
5.6 DIC frame for wedge punching on a low density ($\rho = 0.038$) cubic specimen 84
5.7 Contours of displacement along the rise direction for the foam of lower density 85
5.8 The normalized force-penetration depth curves for low density cubic foam specimens 88

5.9 The curves of loading force vs. the penetration depth for wedge punching on low density foam specimens with a geometry of a cross section $10\,\text{cm} \times 10\,\text{cm}$ and a height of $5.0\,\text{cm}$. (a) Force vs. indentation depth curves. (b) Normalized curves 89
5.10 (a) Conical punching experimental setting. (b) Sketch of the 3-D interface 90
5.11 Conical punching on cubic specimens. (a) Loading force vs. penetration depth curves. (b) Corresponding normalized curves 91
5.12 Conical punching on shorter specimens. (a) Loading force vs. penetration depth curves. (b) Corresponding normalized curves 91
5.13 Loading force vs. penetration depth curve in log-log space for conical punching on short specimens 92

6.1 (a) A free-standing thin film. C_1 and C_2 are cuts performed for stress analysis. (b) The surface stress T acting on the perimeter of C_1. (c) The compressive stress induced by T on the surface of C_1. (d) The compressive stress induced by T on the surface of C_2. (e) Applied traction that gives the same stresses as T. 98
6.2 A plot of the dimensionless apparent yield stress σ_a^y/σ_y vs. the dimensionless thickness $h\sigma_y/T$. See eq. (6.1). The points F, R, M, and V are referred to in the text. The size effect of the apparent tensile yield stress reverses from hardening to softening at the point R. 100
6.3 A plot of the dimensionless quantities s_1, s_2, and s_3 vs. the dimensionless thickness, $h\sigma_y/T$. See eqs. (6.2–6.4). 106
6.4 A plot of the normalized plastic strain at failure in the direction of the applied stress vs. the dimensionless thickness, $h\sigma_y/T$. See eq. (6.6). 107

Part I

Mechanical response of polyether polyurethane foams under multiaxial stress

Chapter 1

Introduction

Solid foams are cellular materials which may be described as numerous cells joined together to fill space. The cells can consist of bars (open-cell foams) or membranes (closed-cell foams). Solid foams have been manufactured out of polymers, metals, carbon, graphite and ceramics. Solid foams also occur in the form of natural materials such as wood, cork, cancellus bone, sponge, and coral.

Here we concentrate on open-cell, elastic (or "flexible") polymeric foams, and in particular on elastic polyether polyurethane foams. We will frequently refer to the foams of this type as "EPP foams."

EPP foams are widely employed in engineering applications. For example, in the aeronautical industry, EPP foams are among the most commonly used materials in the cores of sandwich panels. Due to their ability to absorb impact energy at relatively low compressive stresses, EPP foams are also widely used in packaging to protect fragile products from the jolts associated with transportation and handling. For the same reason, EPP foams are used in car seats to provide comfort and safety to passengers.

The first EPP foam was made by Otto Bayer and coworkers in the laboratory in 1941 (Bayer, 1947). Industrial production started in Germany in 1952. Since then, polymeric foams have been developing steadily to become a large global industry. According to a report published recently by Global Industry Analysts, Inc. (2008), the worldwide market of polymeric foams is to reach 20.5 million tons by 2010.

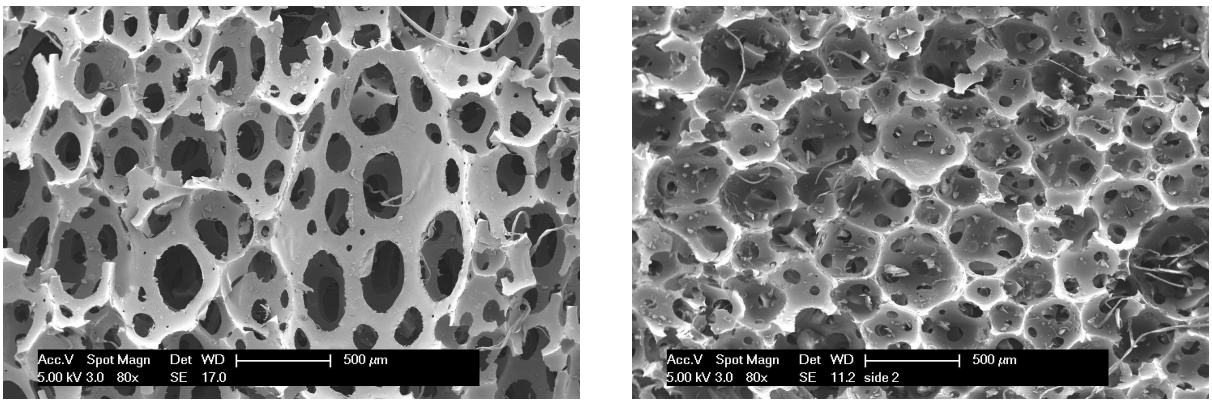

(a) (b)

Figure 1.1: SEM microphotographs of two cross sections in an EPP foam of measured apparent density $\rho_a = 51.6\,\mathrm{kg/m^3}$ (General Plastics EF-4003). a) Section parallel to the rise direction. b) Section normal to the rise direction. (Sabuwala, Dai, and Gioia, unpublished.)

1.1 Microstructure of foams

Polymeric foams are manufactured by promoting the growth of numerous gas bubbles within a liquid or solid layer of polymer, which expands anisotropically, predominantly along a direction normal to its mid-plane—the so-called rise direction (Artavia et al., 1994). Depending on the polymer and the processing conditions, the outcome is a foam, which can be open-cell or closed-cell. EPP foams are open-cell and elastic.

Figure 1.1 shows the microstructure of an EPP foam of low relative density. The relative density is defined as $\rho \equiv \rho_a/\rho_s$, where ρ_a is the apparent density of the foam (i.e., the mass per unit volume of foam) and ρ_s is the density of the solid bulk material of which the foam is made. (In the case of Fig. 1.1, the solid bulk material is polyether polyurethane.) The cross section of Fig. 1.1a is parallel, whereas the cross section of Fig. 1.1b is normal, to the rise direction. We can aptly describe the microstructure of Fig. 1.1 as a three-dimensional network of bars of similar length and cross section.

In modeling a foam, it is common to define an idealized microstructure of the foam. A typical idealized microstructure in two dimensions is an hexagonal honeycomb (Fig. 1.2a) (Patel and Finnie, 1970; Gibson et al., 1982a; Warren and Kraynik, 1987; Overaker et al., 1998). A typical idealized microstructure in three dimensions is made of tetrakaidecahedrons,

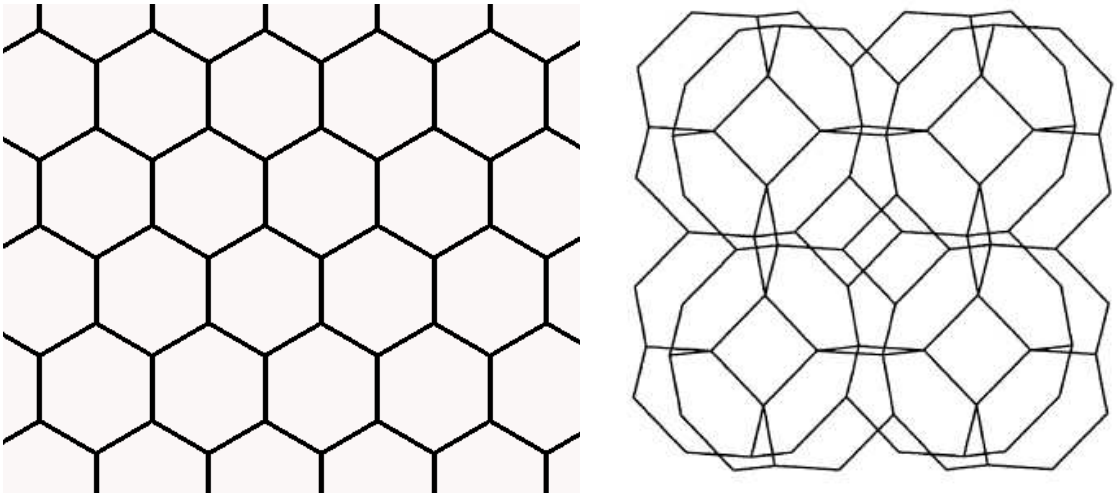

(a) (b)

Figure 1.2: Typical idealized microstructures. a) An hexagonal honeycomb. b) Five tetrakaidecahedrons (Laroussi et al., 2002).

i.e., 14-sided polyhedrons with eight hexagonal and six quadrilateral faces (Fig. 1.2b) (Zhu et al., 1997; Laroussi et al., 2002; Gong and Kyriakides, 2005).

The idealized microstructures of Fig. 1.2 satisfy the rules of Plateau (Plateau, 1873). According to these rules, if a uniform surface tension is the dominant force during the foaming process, three films meet at equal angles of 120° to form cell edges, and four edges join at each vertex at the tetrahedral angle, $\arccos(-1/3) \approx 109.47°$.

The tetrakaidecahedron is widely known as the Kelvin foam model, as it was William Thomson (Lord Kelvin) (Thomson, 1887) who identified the tetrakaidecahedron (with slightly curved faces) as the only polyhedron that packs to fill space and minimize the surface area per unit volume (Gibson and Ashby, 1997). Note, however, that there exists a compound structure which packs to fill space with about 0.4% lower surface per unit volume than the Kelvin model. This compound structure was found by Weaire and Phelan (1994) using the computer software Surface Evolver (Brakke, 1992).

Foams have also been modeled in 3D using simple cubes (Gent et al., 1963; Gibson et al., 1982b), tetrahedral elements (Warren and Kraynik, 1988), pentagonal dodecahedrons (Menges Knipschild, 1975; Patel and Finnie, 1970), and elongated tetrakaidecahedrons (Gong and Kyrikides et al., 2005; Sullivan et al., 2008; Jang et al., 2008).

1.2 Foam mechanics

Since Gent et al. (1963) proposed one of the first mechanical models of cellular materials, there has been much research on the mechanics of cellular materials. Gibson and Ashby (1997) give an extensive review. More detailed studies include the book by Weaire and Hutzler (1999), and the PhD dissertations of Wang (2001), Daxner (2003) and Gong (2005).

The mechanical models of foams can be divided into two categories. The first category includes the cell-scale models, which are based on the simplified mechanics of a single, idealized cell or set of idealized cells. These models relate the structural mechanics of the cell or set of cells to the mechanical response of an equivalent continuum; both two-dimensional (Patel and Finnie, 1970; Gibson et al., 1982a; Warren and Kraynik, 1987) and three-dimensional cell-scale models (Gibson et al., 1982b; Warren and Kraynik, 1988; Zhu et al., 1997; Wang and Cuitiño, 2000; Sullivan et al., 2008) have been proposed. With suitable boundary conditions, cell-scale models have been used to great advantage. For example, Gibson and Ashby (1997) have used cell-scale models to identify the relative density as the most important parameter of foams, and to establish the scaling law that relates the Young's modulus of a foam to the relative density of the foam.

The second category includes the statistical models of foams. In these models, a "statistically meaningful" (Schraad and Harlow, 2006) set of cells is used to account for the effect of irregular foam microstructures. Thus, for example, statistical models have been used by Papka and Kyriakides to study irregular aluminum honeycombs under uniaxial (1994) and biaxial (1999a; 1999b) in-plane loading; by Triantafyllidis and Schraad (1998), Chen et al. (1999), Zhu et al. (2001), Okumura et al. (2004), and Zhu et al. (2006) to ascertain the deformation mechanism of ideal and Voronoi honeycombs; and by Laroussi et al. (2002) to study the nonlinear mechanical response of 3D open-cell foams. Other studies of the effect of irregular foam microstructures have been performed by Zhu et al. (2000) and (2002). More recently, Gong and Kyriakides (2005) have studied the effects of the shear deformation and the cross-sectional shape of the struts of open-cell foams. Using X-ray tomography (Maire

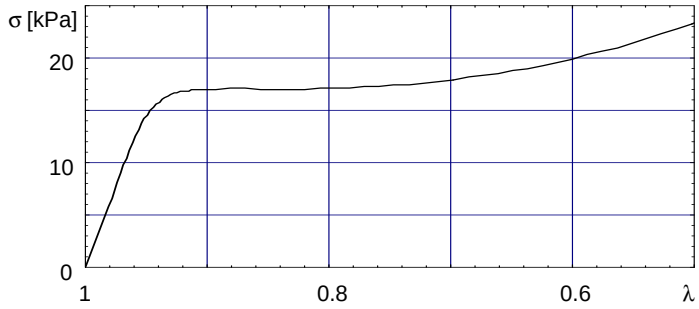

Figure 1.3: Mechanical response of the low-density EPP foam of Fig. 1.1 subject to uniaxial compressive stretch along the rise direction (Gioia et al., 2001). A stretch $\lambda = 1$ corresponds to the undeformed geometry, whereas stretches $\lambda < 1$ correspond to compressed geometries.

et al., 2003), Jang et al. (2008) have been able to ascertain the effect of geometrical details such as the cell size and ligament length distributions, and the geometry of the nodes.

1.3 Elastic Polyether Polyurethane foams under uniaxial compressive loading along the rise direction

In this section, we present a brief review of the mechanical response of EPP foams under uniaxial compressive loading along the rise direction. As part of this brief review, we introduce a number of concepts which will recur throughout the present work, starting from the following section, in which we state the major goals of the work.

In Fig. 1.3 we show the typical mechanical response of a low-density EPP foam subject to uniaxial compressive stretch along the rise direction. The stress-stretch (σ-λ) curve of Fig. 1.3 consists of a linear portion, a stress plateau, and a hardening portion. The most interesting feature of this σ-λ curve is the stress plateau.

The stress plateau of Fig. 1.3 occurs only in low-density EPP foams. If the density of a foam is higher than a certain critical density, there is no stress plateau, and the σ-λ curve hardens monotonically throughout the experiment. Thus the mechanical response of an EPP foam depends not just quantitatively but qualitatively on the density of the foam.

A crucial point that has frequently been overlooked concerns the stretch (or strain) fields that accompany a stress plateau. These stretch fields are highly heterogenous (Fig. 1.4).

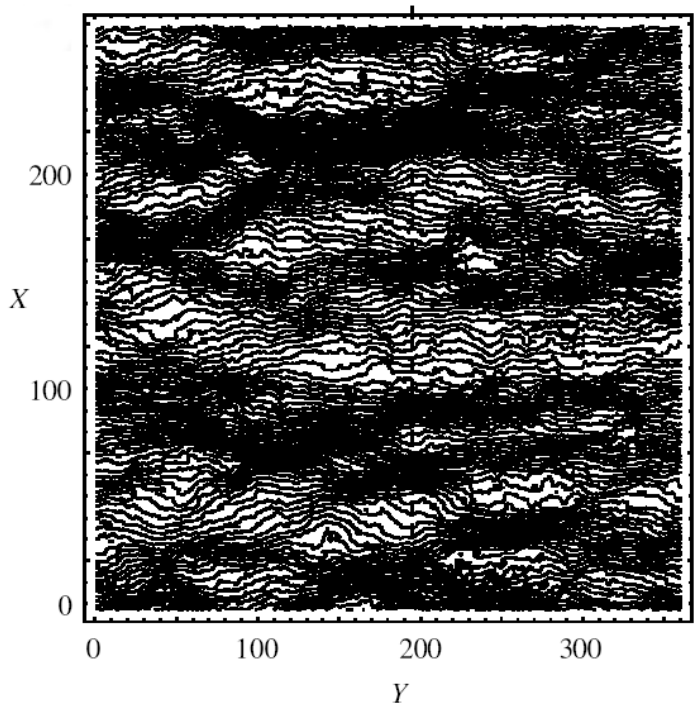

Figure 1.4: Typical displacement field on the surface of a low-density foam. Measured during the uniaxial test that gave the stress–stretch curve of Fig. 1.3 (Gioia et al., 2001). The foam is the low-density EPP foam of Fig. 1.1, and the applied average stretch is $\bar{\lambda} = 0.74$, within the stress plateau of Fig. 1.3. The surface shown in the figure is $3.72\,\text{cm} \times 2.54\,\text{cm}$, and the height of $2.54\,\text{cm}$ is aligned with the rise direction, which coincides with the X-axis and the direction of loading. The units of X and Y are pixels, and the geometry is the underformed geometry. The displacement field is given in the form of a contour plot. Each contour in the figure corresponds to a constant value of the displacement u_X in the rise direction. The value of u_X on any given contour differs by a fixed increment from the value of u_X on an adjacent contour. The contours in the figure indicate the existence of two preferred values of $\partial u_X/\partial X$, which correspond to two characteristic values of stretch and two configurational phases of the microstructure of the foam (Gioia et al., 2001).

Therefore, the values of λ in Fig. 1.3 must be interpreted as as values of the applied average (or mean) stretch.

Further, the stretch fields of Fig. 1.4 reveal the existence of two preferred values of stretch. These preferred values of stretch remain invariant as the σ–λ curve traces the stress plateau. The changing values of the applied average stretch are accommodated by suitable changes in the relative volume fraction of the preferred values of stretch. Values of stretch in between the two preferred values of stretch appear be excluded from the measured stretch fields.

It is widely thought that the stress plateau of Fig. 1.3 is related to a buckling of the network of bars of Fig. 1.1. A number of authors have proposed that this is conventional,

or Euler, buckling—that is to say, bifurcation of equilibrium (Papka and Kyriakides, 1994; Gong and Kyriakides, 2005). However, the buckling process has been documented at the microstructural level by Gioia et al. (2001) (Fig. 1.5), who concluded that the microstructure undergoes snap-through buckling, a limit-point phenomenon without bifurcation of equilibrium.

If the microstructure of a foam undergoes Euler buckling, the attendant stretch field will correspond to an eigenfunction of arbitrary amplitude. As the applied average stretch is decreased following buckling, the stress-stretch curve traces a stress plateau, and the stretch field remains invariant except for the amplitude, which increases to accommodate the applied average stretch. Thus the mechanism of Euler buckling does not appear to be consistent with the observed stretch fields, where two preferred values of stretch are present in association with the stress plateau, and intermediate values of stretch are excluded.

Where a cell of a low-density EPP foam undergoes snap-through buckling, the cell switches discontinuously between a geometric configuration associated with a characteristic, high value of stretch (or low value of strain) to a geometrical configuration associated with a characteristic, low value of stretch (or high value of strain). Therefore, the cell behaves as a bistable elastic structure, and the two characteristic values of stretch (or strain) can be identified with the two preferred values of stretch observed in experiments, and ascribed to two distinct configurational phases of the foam. The heterogenous stretch fields observed in experiments are two-phase fields. In these two-phase fields, the applied average stretch is accommodated by mixing the two configurational phases of the foam in accord with the rule of mixtures. The stress plateau corresponds to a Maxwell stress.

We conclude that the mechanism of snap-through buckling provides a straightforward theoretical interpretation of the stretch fields and the stress plateau observed in experiments Gioia et al. (2001). In this interpretaion, the basic physics of large deformation in low-density EPP foams is the physics of phase transitions.

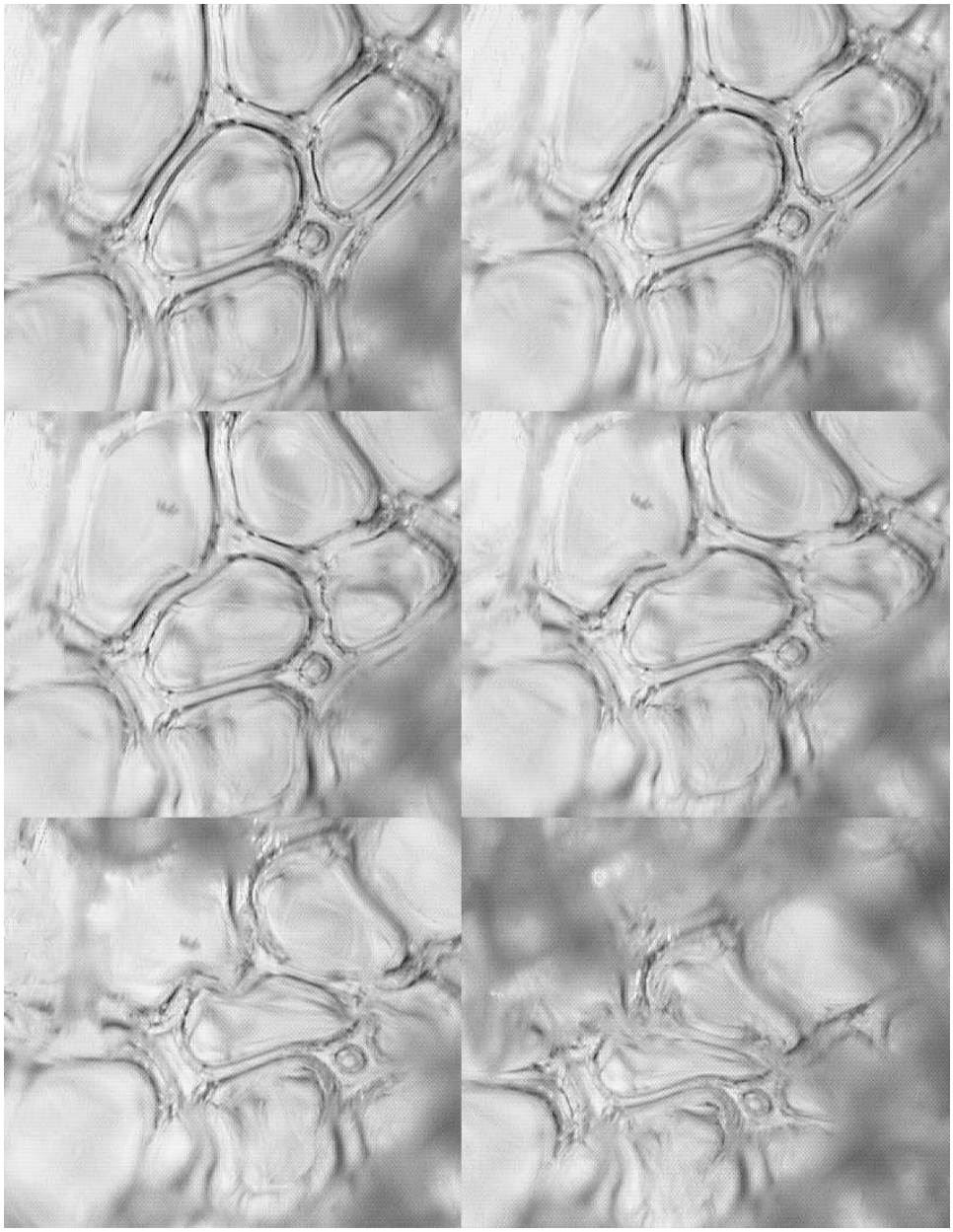

Figure 1.5: Snap-through buckling of the microstructure of Fig. 1.1 (Gioia et al., 2001). Stretching is along the rise direction, which in this figure is the vertical direction. The sequence goes from left to right and top to bottom. The cells appear to be equiaxed (cf. Fig. 1.1b) because the line of view is not perpendicular to the rise direction.

1.4 Statement of the major goals of this research

In spite of much research into the mechanical behavior of elastic foams, much remains to be done, and the state of the art in models of elastic foams is far from satisfactory.

1. Most practical applications of foams involve multiaxial loading, but there has been little experimental and theoretical work on the mechanical response of elastic foams subjected to multiaxial states of stress. In particular, there is a need for a model capable of predicting the mechanical response of elastic foams under arbitrary triaxial states of stress. Such a model must be calibrated by comparison with suitable experimental measurements of the mechanical response of elastic foams under multiaxial state of stress.

2. The mechanical response of an elastic foam depends not just quantitatively but also qualitatively on the relative density of the foam. Yet no model has been used to make predictions for sets of foams of widely differing densities, and calibrated using experimental measurements for a complete series of commercially available elastic foams.

3. The scant comparisons with experiments have been limited to the value of the stress plateau, and no model has been tested over the entire mechanical response as a function of the strain, and for widely differing densities.

4. A stress plateau appears to be invariably accompanied by heterogeneous, two-phase strain fields, yet little attention has been paid to whether a model is capable of predicting heterogenous two-phase strain fields.

Here we investigate the deformation mechanism of open-cell elastic foams, more specifically elastic polyether polyurethane (EPP) foams, by means of theory, experiments and computations. In applications, under service conditions, EPP foams are commonly subjected to large strains, in a regime where nonlinear geometrical effects dominate the mechanical response. Therefore, the mechanical behavior of EPP foams under large strains is of special interest to us, and the mechanical response under small strains of relatively minor interest.

Our main goal is to develop and calibrate a model of EPP foams capable of addressing points 1 to 4 above. A crucial component of this endeavor is to obtain suitable experimental data for the purpose of calibrating the model. The experimental data must include stress–strain or force–displacement curves for a variety of loading conditions and foam densities, as well as full strain fields, which will allow us to ascertain the character of the strain fields associated with a given loading condition.

Thus, as part of the calibration of our model, we will verify not just that the model predict a stress plateau where a stress plateau has been observed in experiments, but also that the model predict the two-phase strain fields associated with a stress plateau. To this end, the model must embody the basic physics of large-strain deformation in EPP foms: the physics of phase transitions.

In the chapter that follows (Chapter 2), we seek to provide a suitable theoretical framework for our research. To that end, we discuss a few mean-field models of EPP foams. The class of mean-field models is the class to which our model of Chapter 4 belongs, but in Chapter 2 we focus on foams subjected to uniaxial loading and discuss a number of specialized versions of our model of Chapter 4. These specialized versions of our model of Chapter 4 afford us an opportunity to highlight the two most salient characteristics of mean-field models in general: that, in accord with experimental results, these models may undergo configurational phase transitions and exhibit a critical point.

Chapter 2

Uniaxial mean-field models and the critical point

2.1 Introduction

It has been shown experimentally that where an elastic polyether polyurethane (EPP) foam of relatively low density is compressed along the rise direction, the foam displays two preferred values of stretch which may be interpreted as configurational phases of the microstructure of the foam (Gioia et al., 2001). If a foam of higher density is compressed, the two preferred values of stretch are closer together, and there exists a critical density for which the two preferred values of stretch coincide at a critical point.

In thermodynamics, the critical point is the apex of a coexistence curve which separates two distinct phases. Above the critical point, it is possible to pass from one phase to the other without discontinuities (Goldenfeld, 1992). Power-law behavior governs second-order phase transitions (also called continuous phase transitions) in the immediate vicinity of a critical point (Goldenfeld, 1992), and the exponents that appear in the power laws are known as critical exponents. For example, experiments indicate that in the liquid-gas transition of sulphur hexafluoride (SF_6),

$$\mid \rho_+ - \rho_- \mid \propto \mid T - T_c \mid^{0.327 \pm 0.006} \tag{2.1}$$

near critical point, where T is the temperature, T_c is the critical temperature, ρ_+ and ρ_- are the values of the density on the two branches of the coexistence curve below T_c—that is to say, the preferred values of density, and 0.327 ± 0.006 is the critical exponent. Similarly, experiments indicate that at the onset of magnetization in the antiferromagnet $DyAlO_3$, the

magnetization behaves in the form:

$$M \propto (T_c - T)^{0.311 \pm 0.005}. \tag{2.2}$$

The critical exponents are frequently found to be independent of the specific system, a phenomenon known as universality (Goldenfeld, 1992). For example, for SF_6 and $DyAlO_3$ the exponents are the same within experimental resolution.

It is virtually impossible for us to study the critical point of EPP foams experimentally, because EPP foams are not available in any given relative density. In this chapter, we will use theoretical models to investigate the mechanical behavior of EPP foams close to the critical point.

2.2 A simplified mean-field model

Compressed open-cell solid foams frequently exhibit spatially heterogeneous distributions of local stretch. Gioia et al. (2001) proposed a mean-field model and studied the energetics of the model to show that the stretch heterogeneity observed in uniaxial experiments stems from the lack of convexity of the governing energy functional, which favors two characteristic values of local stretch. These characteristic values of the local strech are independent of the applied average stretch and define two configurational phases of the foam. The predicted stretch distributions correspond to stratified mixtures of the phases; stretching occurs in the form of a phase transition, by growth of the volume fraction of one of the phases at the expense of the volume fraction of other (Gioia et al., 2001).

The mean-field model of Gioia et al. (2001) yields predictions that are in good accord with experimental data for a series of EPP foams of relative densities ranging from 0.03 to 0.12. Nevertheless, in this model the microstructure of the foam is a regular network of bars governed by the von Kármán theory of beams, and the mechanical response must be calculated computationally. Here we introduce a simplified mean-field model (Dai and Gioia, 2008) for which the mechanical response can be calculate analytically.

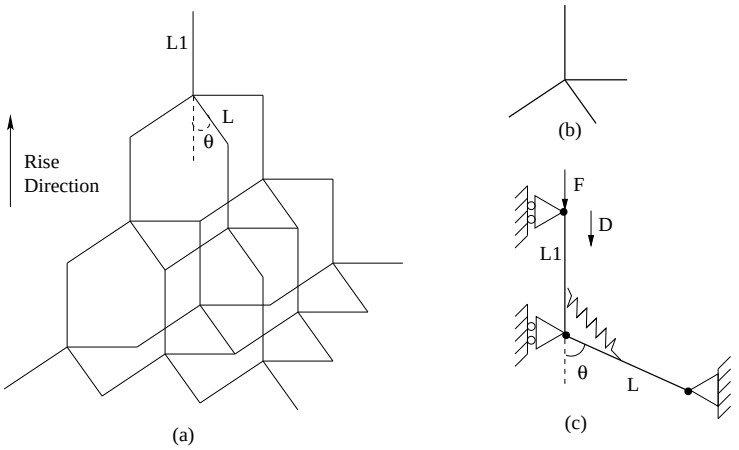

Figure 2.1: The simplified mean-field model of EPP foams. (a) Undeformed network of bars. (b) A four-bar cell. (c) For uniaxial stretch along the rise direction, the four-bar cell may be thought of as a two-bar cell.

In our model, the foam is a regular network of bars (Fig. 2.1a) made of identical four-bar tetrahedral cells. In each one of these four-bar tetrahedral cells, a bar of length L_1 is aligned with the rise direction of the foam. This bar is rigid. The other three bars, of length L and circular cross section of radius r, form an angle θ with the rise direction (Fig. 2.1b). These bars are linear elastic, have a Young's modulus E, and can only deform axially, without bending. If the foam is stretched uniaxially along the rise direction, the four-bar cell may be thought of as a two-bar cell (Fig. 2.1c).

To endow this two-bar cell with bending energy, we add a rotational spring of modulus K, so that the bending energy of the cell is given by the expression, $W_b = \frac{1}{2}K(\Delta\theta)^2$. We use $K = cEr^4/L$ (from the relation between a moment and the attendant rotation angle in a beam), where c is a dimensionless parameter and can be viewed as a material property of the foam.

The relation between the change of angle $\Delta\theta$ and the displacement D of the upper node is set by the geometry:

$$\Delta\theta = \theta - \cos^{-1}\frac{L\cos\theta - D}{\sqrt{(L\sin\theta)^2 + (L\cos\theta - D)^2}}. \tag{2.3}$$

Thus the energy stored in the cell is given by the expression,

$$W = \frac{1}{2}E\pi r^2\frac{(L-\sqrt{(L\cos\theta-D)^2+(L\sin\theta)^2})^2}{L} + \\ +\frac{1}{2}K(\theta-cos^{-1}\frac{L\cos\theta-D}{\sqrt{(L\sin\theta)^2+(L\cos\theta-D)^2}})^2. \tag{2.4}$$

The tributary volume of the cell in the undeformed geometry is given by the expression (Wang and Cuitiño, 2000),

$$V_{cell} = \frac{3\sqrt{3}}{4}(L\sin\theta)^2(L_1+L\cos\theta). \tag{2.5}$$

By introducing the normalized length of the vertical bar $\tilde{L}_1 = L_1/L$, the normalized displacement $\tilde{D} = D/L$, and the normalized radius of the cross section $\tilde{r} = r/L$, we get the strain energy per unit volume of cell:

$$\phi = \frac{3W}{2V_{cell}} = \frac{1}{\sqrt{3}(\sin\theta)^2(\tilde{L}_1+\cos\theta)}[E\pi\tilde{r}^2(1-\sqrt{(\cos\theta-\tilde{D})^2+(\sin\theta)^2}\,)^2 + \\ +cE\tilde{r}^4(\theta-cos^{-1}\frac{\cos\theta-\tilde{D}}{\sqrt{(\cos\theta-\tilde{D})^2+(\sin\theta)^2}})^2]. \tag{2.6}$$

The stretch of the cell is related to $\tilde{D}$

$$\lambda = 1-\frac{\tilde{D}}{\tilde{L}_1+\cos\theta}, \tag{2.7}$$

and the relative density of the foam can be expressed as a function of $\tilde{r}$ and L_1, namely

$$\rho = \frac{2\pi\tilde{r}^2(3+\tilde{L}_1)}{3\sqrt{3}(\tilde{L}_1+\cos\theta)(\sin\theta)^2}. \tag{2.8}$$

As expression for the stress follows from (2.6-2.8) in the form,

$$\sigma(\lambda) = \frac{d\phi}{d\lambda} = \frac{d\phi}{d\tilde{D}}\frac{d\tilde{D}}{d\lambda}. \tag{2.9}$$

The energy curve is nonconvex for a low-density foam (Fig. 2.2): for $\lambda_1 \le \lambda$ and $\lambda \ge \lambda_2$,

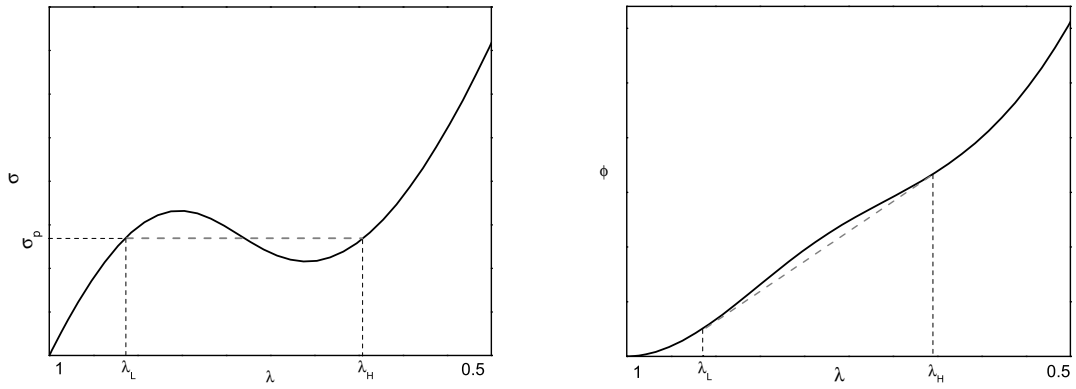

Figure 2.2: (a) The stress-stretch curve for a low-density foam. (b) The attendant energy curve, which is nonconvex.

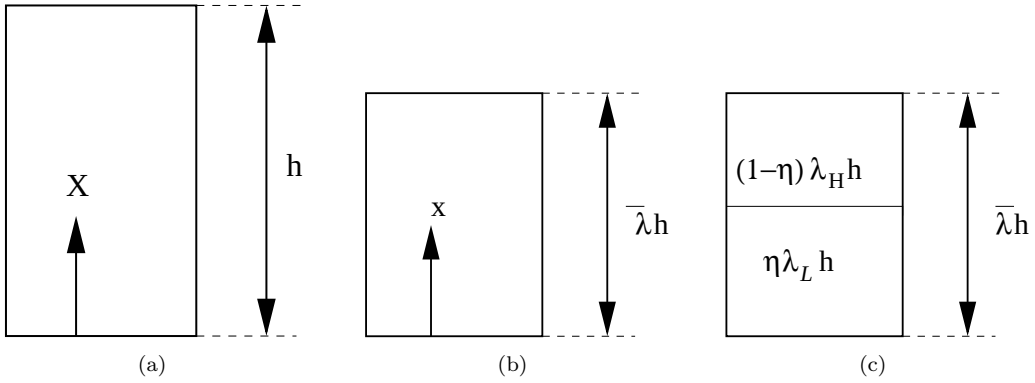

Figure 2.3: The stretch distribution in a low-density foam specimen. (a) Original geometry of the specimen. (b) Current geometry of the specimen; $\bar{\lambda}$ is the applied average stretch. (C) Two-phase stretch distribution in the specimen.

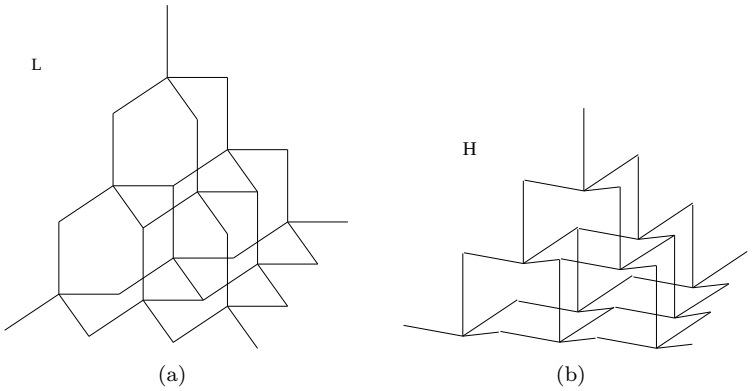

Figure 2.4: The network of bars before and after buckling. (a) The low-density phase L (schematic). (b) The high-density phase H

the curvature is positive, $\frac{d^2\phi}{d\lambda^2} > 0$, whereas for $\lambda_1 < \lambda < \lambda_2$ the curvature is negative, $\frac{d^2\phi}{d\lambda^2} < 0$. A homogeneous strain distribution cannot be realized when the applied average stretch $\bar{\lambda}$ is in the range (λ_1, λ_2). Thus a heterogeneous stretch distribution should occur (Fig. 2.3).

Assume that a volume fraction η is under a stretch $\lambda_L > \bar{\lambda}$ and the volume fraction $1-\eta$ is under a stretch $\lambda_H < \bar{\lambda}$. (The stretches λ_L and λ_H correspond to the unbuckled and buckled phases of Fig. 2.4, respectively.) For compatibility with the applied average stretch $\bar{\lambda}$, we must satisfy the rule of mixtures,

$$\eta = \frac{\lambda_L - \bar{\lambda}}{\lambda_L - \lambda_H}. \tag{2.10}$$

The average energy density of the specimen is then a function of λ_L, λ_H and η,

$$\phi^*(\lambda_L, \lambda_H, \eta) = \eta\phi(\lambda_H) + (1-\eta)\phi(\lambda_L). \tag{2.11}$$

The equilibrium can be realized by making $\phi^*(\lambda_L, \lambda_H, \eta)$ stationary subject to the subsidiary condition (2.10). Then, λ_L, λ_H, and the plateau stress σ_p (which is a Maxwell stress) follow from the Erdmann equilibrium equations (Gioia et al., 2001),

$$\sigma_p = -\frac{\phi(\lambda_L) - \phi(\lambda_H)}{\lambda_L - \lambda_H} = -\phi'(\lambda)|_{\lambda=\lambda_L} = -\phi'(\lambda)|_{\lambda=\lambda_H}. \tag{2.12}$$

Associated with the stress plateau, a two-phase stretch distribution exists for each value of overall stretch in the range $\lambda_L \geq \bar{\lambda} \geq \lambda_H$. When $\bar{\lambda}$ decreases from λ_L to λ_H, the volume fraction of the unbuckled phase, η, changes from 0 to 1 and the stress remains constant. Thus a decrease of the overall stretch $\bar{\lambda}$ is accompanied by the propagation of the interface which separates the two phases. This process is analogous to the transition of a material from the liquid phase to the gaseous phase: as the liquid/gas interface propagates, the pressure remains constant.

Equation 2.12 gives λ_L and λ_H for low-density foams. As the foam density increases, λ_L gets closer to λ_H; where ρ attains a critical value ρ_c, then $\lambda_L = \lambda_H$, the two configurational

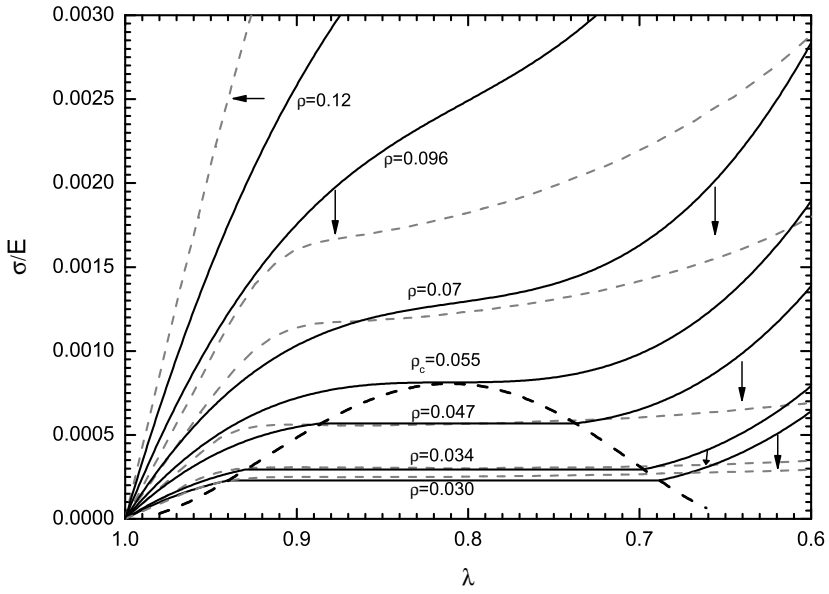

Figure 2.5: Stress-stretch curves. The dashed grey lines are experimental data from (Gioia et al., 2001). These data are for six EPP foams of measured apparent densities ρ_a=51.6, 57.7, 80.2, 159, 219 and 280 kg/m^3. The calculate the relative densities *rho*, we use $\rho_s = 1700\,\mathrm{kg/m^3}$ (for the 3 foams of lower density) or $\rho_s = 2200\,\mathrm{kg/m^3}$ (for the 3 foams of higher density). The specimens have a cross-section of $10.2\,\mathrm{cm} \times 10.2\,\mathrm{cm}$, and a height of 5.08 cm. The solid black lines are predicted from (2.6) and (2.9). For the foams of density lower than the critical density (i.e., for the low-density foams), the predicted mechanical reponse has been properly convexified in accord with the Erdman equilibrium eq. (2.12), so that the stress-stretch curves display the stress plateaus.

phases are not distinguishable, and we have reached the critical point. For foams of density higher than ρ_c, there is no phase transition and hence no stress plateau. By choosing $\theta = cos^{-1}(1/3)$, $\tilde{L_1} = 1.5$, $c = 10.2$, and $E = 42\,\mathrm{MPa}$, we obtain a good fit of the experimental data of Gioia et al. (2001) (Fig. 2.5). The critical point is apparent in Fig. 2.5; the critical density, critical stress, and critical stretch associated with this critical point are $\rho_c = 0.5507$, $\sigma_c = 7.8591 \times 10^{-4} E_m$, and $\lambda_c = 0.8103$, respectively.

2.3 Critical exponents

For liquid-gas fluid systems that are describable by the pressure p, the specific volume v, and the absolute temperature T, the following power-law relations hold close to the critical point:

$$\begin{aligned} &\frac{v - v_c}{v_c} \sim |t|^{\beta}; \qquad && \frac{p - p_c}{p_c} \sim \left(\frac{v - v_c}{v_c}\right)^{\delta}; \\ &C_v = T\frac{\partial S}{\partial T} = t^{\alpha}; \qquad && K_T \equiv \frac{1}{v}\frac{\partial v}{\partial p}\Big|_T t^{-\gamma}, \end{aligned} \tag{2.13}$$

where p_c is the critical pressure, v_c is the critical specific volume, and T_c is the critical temperature respectively, $t \equiv (T - T_c)/T_c$, S is the entropy, K_T is the compressibility at constant temperature, C_v is the specific heat capacity at constant volume, and α, β, δ and γ are critical exponents.

Van der Waals proposed an equation of state for the liquid-gas fluid system:

$$p = \frac{k_B T}{v - b} - \frac{a}{v^2}, \tag{2.14}$$

where a and b are two constants depending on the fluid system. The Van der Walls equation of state accounts for the hard core potential of the atoms (i.e. the excluded volume) and the attractive interactions between the atoms.

From (2.13) and (2.14), the critical exponents of Van der Waals fluids can be calculated analytically, and it is found that $\beta = 1/2$, $\delta = 3$, $\alpha = 0$, $\gamma = 1$ (Goldenfeld, 1992).

The experimental results of Fig. 2.5 suggest an analogy (Gioia et al., 2001) between

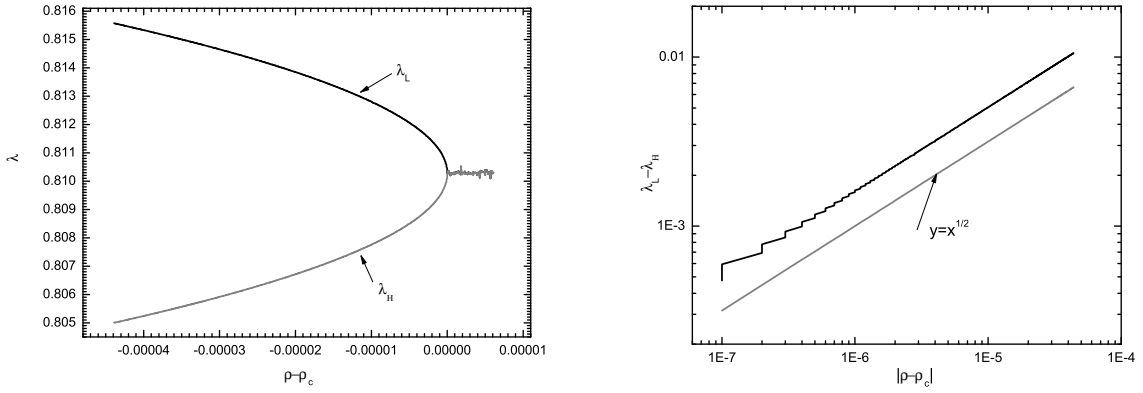

(a) (b)

Figure 2.6: (a) λ_L and λ_H in a region very close to the critical point. (b) $\lambda_L - \lambda_H$ vs. $|\rho - \rho_c|$ in log-log scale.

open-cell elastic foams and liquid-gas fluid systems. In this analogy

$$\sigma \sim p, \lambda \sim v, \rho \sim T. \tag{2.15}$$

2.3.1 Critical exponents for the simplified mean-field model

From eq. (2.13) and the analogy, we expect

$$(\lambda_L - \lambda_H) \sim (\rho - \rho_c)^{\beta}, \tag{2.16}$$

near the critical point, where λ_L and λ_H are the two preferred stretches, which for the simplified mean-field foam model can be calculated from eq. (2.12).

In Fig. 2.6a we plot λ_L and λ_H over a narrow vicinity of the critical point, $0.550 \leq \rho \leq 0.551$. A log-log plot of $\lambda_L - \lambda_H$ vs. $|\rho - \rho_c|$ is shown in Fig. 2.6b. From Fig. 2.6b, it is apparent that $\beta = 1/2$.

From eq. (2.13) and the analogy, we expect

$$\frac{\sigma - \sigma_c}{\sigma_c} \sim \ (\frac{\lambda - \lambda_c}{\lambda_c})^{\delta} \qquad (\text{as } \rho = \rho_c), \tag{2.17}$$

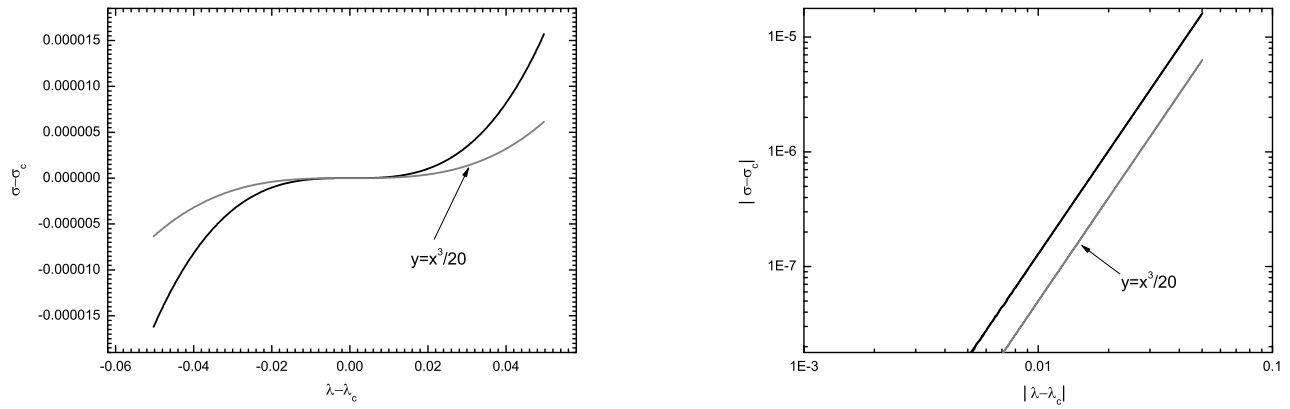

(a) (b)

Figure 2.7: (a) $\sigma - \sigma_c$ vs. $\lambda - \lambda_c$ for $\rho = \rho_c = 0.05507$ and $0.76 \leq \lambda \leq 0.86$. (b) $|\sigma - \sigma_c|$ vs. $|\lambda - \lambda_c|$ in log-log scale.

near the critical point. A plot of $\sigma - \sigma_c$ vs. $\lambda - \lambda_c$ for $\rho = \rho_c = 0.05507$ and over a narrow vicinity of the critical point $0.76 \leq \lambda \leq 0.86$ is shown in Fig. 2.7a (in linear-linear scale) and in Fig. 2.7b (in log-log scale). The power-law behavior is apparent in these two figures, and from Fig. 2.7b it is apparent that the exponent $\delta = 3$.

For γ, from (2.13) and the analogy, we expect

$$-\frac{1}{\lambda}\frac{\partial \lambda}{\partial \sigma}\bigg|_{\rho} = t^{-\gamma}, \tag{2.18}$$

near the critical point. By fixing $\lambda = \lambda_c = 0.8103$ and varying ρ in a region very close to critical point, $0.55 \leq \rho \leq 0.5507$, we obtain the curve of $-\frac{1}{\lambda}\frac{\partial \lambda}{\partial \sigma}$ vs. $|\rho - \rho_c|$ shown in Fig. 2.8. This curve is a straight line in log-log scale, and $\gamma = 1$.

On the other hand, our analogy between open-cell elastic foams and liquid-gas fluid systems does not include a foam's counterpart of the entropy of a fluid; as a result, for our model of foams, we cannot calculate a value of the critical exponent α directly from eq. (2.13). Nevertheless, the values of the 3 critical exponents that we have calculated for our model of foams ($\beta = 1/2$, $\delta = 3$, and $\gamma = 1$) coincide with the values of the analogous 3 critical exponents of a Van der Waals fluid.

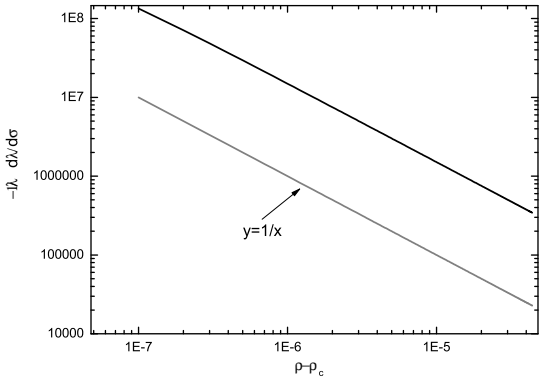

Figure 2.8: $-\frac{1}{\lambda}\frac{\partial\lambda}{\partial\sigma}$ vs. $|\rho - \rho_c|$ in log-log scale.

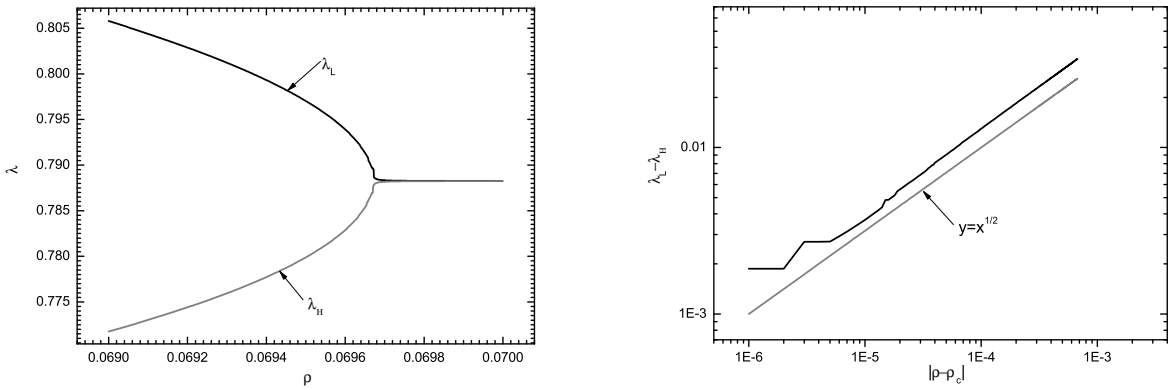

(a) (b)

Figure 2.9: (a) λ_H and λ_L in a region very close to critical point. (b) $\lambda_H - \lambda_L$ vs. $\rho - \rho_c$ in log-log scale.

2.3.2 Critical exponents for a Kármán-beam mean-field model

For Gioia's (2001) model, we find the critical point $\sigma_C = 0.0014105$ and $\lambda_c = 0.78823$. The corresponding critical density is $\rho_c = 0.069673$.

We plot λ_L and λ_H in Fig. 2.9a over a narrow vicinity of the critical point. A log-log plot of $\lambda_L - \lambda_H$ vs. $|\rho - \rho_c|$ is shown in Fig. 2.9b. From Fig. 2.9b, it is apparent that $\beta = 1/2$.

A plot of $\sigma - \sigma_c$ vs. $\lambda - \lambda_c$ for $\rho = \rho_c$ and over a narrow vicinity of the critical point is shown in Fig. 2.10a (in linear-linear scale) and in Fig. 2.10b (in log-log scale). From Fig. 2.10b, it is apparent the exponent $\delta = 3$. Again, the values of the 2 critical exponents

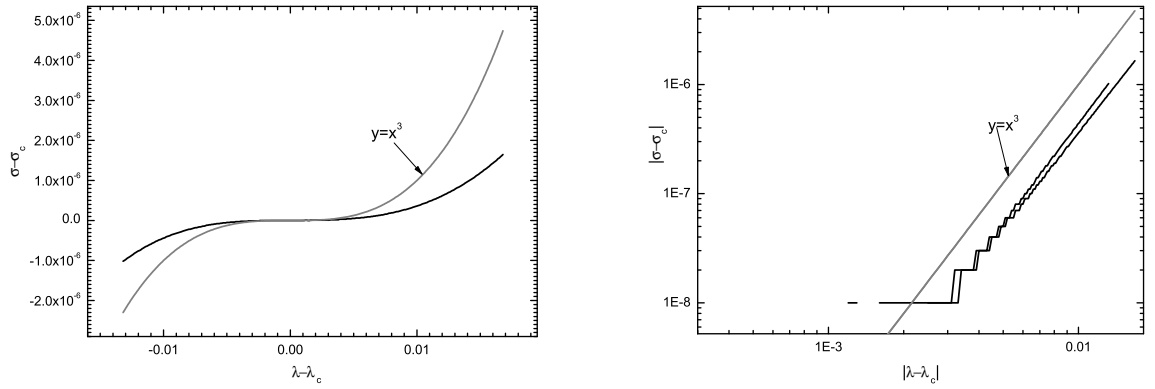

(a) (b)

Figure 2.10: (a) $\sigma - \sigma_c$ vs. $\lambda - \lambda_c$ for $\rho = \rho_c = 0.05507$ and $0.76 \leq \lambda \leq 0.86$. (b) $|\sigma - \sigma_c|$ vs. $|\lambda - \lambda_c|$ in log-log scale.

that we have calculated for the von Kármán beam cell model ($\beta = 1/2$, $\delta = 3$) coincide with the values of the 2 analogous critical exponents of a Van der Waals fluid.

2.4 Discussion

We have discussed a number of models of uniaxially stretched EPP foams. In these models, the end points of a representative cell of the foam are subjected to prescribed displacements, which are affine with the prevailing field of uniaxial stretch. Thus the models of this chapter belong to the same broad class of mean-field models as the more general, 3D model of Chapter 4. Our objective has been to highlight the most salient features of mean-field models of EPP foams.

One of these salient features is that a cell may switch between two characteristic configurations, as shown, for example, in Fig. 2.4. For a single cell it would be meaningless to speak of these characteristic configurations as phases: if one could control and gradually increase the displacememts of the end points of the cell, the cell would successively attain each of the configurations intermediate between the characteristic configurations of Fig. 2.4, but the characteristic configurations would play no special role in the process. This conclusion serves

to stress a key element of our models, namely *homogenization*, whereby the strain energy of the cell is used to compute the strain energy density of an *equivalent continuum*. Any given portion of the equivalent continuum stands for very many identical cells of the microstructure of the foam. As a result, where the equivalent continuum is subject to a an applied stretch, the individual cells that underly the equivalent continuum are free to accommodate the applied stretch in a number of ways. It is on this freedom inherent in the equivalent continuum that the energy analysis of (2.10–2.12) hinges upon. In high-density foams the strain-energy density is convex, the energy analysis selects a unimodal distribution of the local stretch, and the stretch field is homogeneous. In low-density foams, the strain-energy density is nonconvex, the energy analysis selects a bimodal distribution of local stretch, and the stretch field is heterogeneous and composed of two configurational phases.

Nonconvex strain-energy curves, and the attendant configurational phases and two-phase stretch fields, are not peculiar to mean-field models of uniaxially stretched EPP foams. As we shall show in Chapter 4, the strain-energy curves accompanying stretch tensors with at least one compressive component are generally nonconvex; and the calibration of our model of Chapter 4 will include an unprecedented constraint, that the model should predict two-phase fields in accord with the experimental results of Chapter 3.

The other salient characteristic of mean-field models of EPP foams is the critical point. The critical point corresponds to a critical density of the foam. For a foam of critical density, both the first derivative and the second derivative of the strain-energy curve vanish at the critical point.

On the basis of a straightforward analogy with a liquid-gas fluid system, we have been able to compute three critical exponents for a number of mean-field models of uniaxially stretched EPP foams, and to verify that these critical exponents are the same as the corresponding critical exponents of a Van der Waals fluid (the classical mean-field model). Although in our analogy the density of a foam acts as the counterpart of the temperature of a a Van der Waals fluid fluid, it is presently unclear to us what quantity might act as a foam's counterpart of the entropy of a Van der Waals fluid. It may be possible to identify a suitable "effective

entropy" of elastic foams, just as researchers have been able to identify a suitable effective entropy of granular systems (Mehta and Edwards, 1989; Makse and Kurchan, 2002; Coniglio et al., 2005).

Chapter 3

Experiments

In this chapter we report experimental results for a series of elastic polyether polyurethane (EPP) foams under uniaxial and multiaxial loading. We measure the mechanical response in terms of stress-strain or force-displacement data. For some loading cases and load densities, we use a digital image correlation (DIC) technique to track the evolution of the strain field on a surface of the foam specimen.

3.1 Introduction

Experimental research into the mechanical behavior of polymeric foams has been focused on two subjects. (1) The elastic properties, which are of limited interest in applications, where large strains are typically attained under service conditions; and (2) The mechanical response under uniaxial stress and up to large strains. (See, e.g. Gibson et al. (1982a), Gibson et al. (1982b), Zhu et al. (1997), Gioia et al. (2001), Gong (2005).)

Experiments with polymeric foams under multiaxial stress have been largely aimed at mapping the failure envelope in stress space of rigid (or "brittle") polymeric foams (e.g. Shaw and Sata (1966) for rigid polysterene foams; Zaslawsk (1973), Maji et al. (1995), and Triantafillou et al. (1989) for rigid polyurethane foams; Zhang et al. (1997), Deshpande et al. (2001), and Gdoutos et al. (2002) for rigid PVC foams; and Viot (2009) for rigid polypropylene foams). This failure envelope is also known by the name of *yield* envelope. This name may appear confusing, but rigid polymeric foams often undergo a progressive form of brittle failure when tested under compression. In this progressive form of brittle failure, a large deformation accumulates at a constant value of stress, which may be construed as

an apparent yield stress.

For EPP foams, extensive multiaxial tests (including uniaxial, biaxial, and hydrostatic tests) have been performed by Triantafillou et al. (1989). The purpose of these tests was to trace the yield envelope in stress space. Here the word "yield" refers to the beginning of the stress plateau that is characteristic of the stress–strain curves of some EPP foams tested under compression. As this stress plateau occurs only in low-density EPP foams, all of the foams tested by Triantafillou et al. (1989) were of very low apparent density (or weight per unit volume of foam), namely 14.3, 21.8, 28, 41.5, 51.6 $\mathrm{kg/m^3}$. Only a few stress–strain curves were published, to illustrate the method whereby the yield stress was extracted from the stress–strain curves. Thus, despite the importance of multiaxial loading in many practical applications of EPP foams, there exist no experimental data on the mechanical response of EPP foams under a variety of loading conditions and for the full range of commercially available relative densities.

Our purpose here is to conduct an extensive experimental study of the mechanical behavior of EPP foams of a broad range of relative densities, for a variety of loading conditions and up to large strains. To this end, we use a series of commercially available EPP foams of five densities ranging from 50.3 to 220.5 $\mathrm{kg/m^3}$. We subject each foam to five different loading cases, namely, uniaxial compression along the rise direction; uniaxial compression along two mutually perpendicular transverse directions (both normal to the rise direction); uniaxial tension along the rise direction; biaxial loading which combines shear and compression along the rise direction and triaxial loading which combines hydrostatic pressure with compression along the rise direction. In addition to the stress-strain response, for some foam densities and loading cases we also obtain the strain field on the surface of the foam specimen using a global digital image correlation (global DIC) technique (Gao et al., 2002).

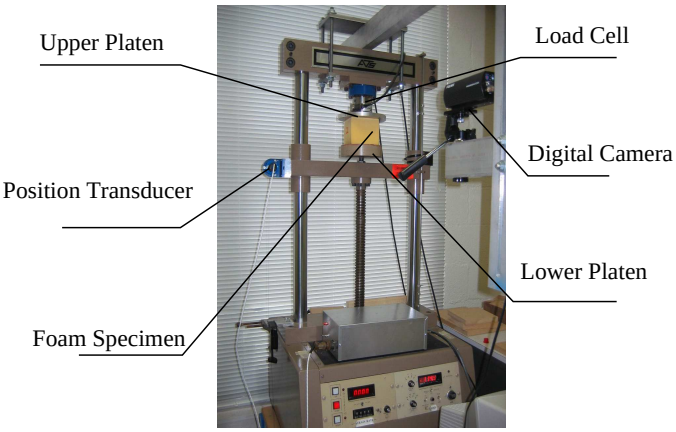

Figure 3.1: ATS testing machine setup

3.2 Experimental set-ups

We use an ATS testing machine (Universal Testing Machines 900 Series, from Applied Test Systems, Inc.) to conduct tests for the first four loading cases. For the triaxial tests, we use a TurePath Automated Stress Path System (From GEOTAC).

The ATS testing machine is shown in Fig. 3.1. For the compression tests, the lower plate is driven up at adjustable rates and compresses the specimen against the fixed upper plate. The loading force is recorded by a load cell (Interface 100 lbs and 10,000 lbs) attached to the upper plate while the displacement is measured by a position transducer (PNL022-00 from Spaceage Control Inc.) attached to the lower plate. During the test, a digital monochrome CCD camera (PULNiX TM-1300 progressive scan) with NaVITAR Zoom 700 lens can be used to obtain 8-bit digital images of 1300 by 1030 pixels for DIC analysis.

For the triaxial case, the specimen is loaded in a two-step process using the TruePath Automated Stress Path System (Fig. 3.2a). First, the specimen is immersed in a chamber filled with silicon oil (Dow Cornings 200 silicone oils, 50cSt). An oil-proof membrane wrapped around the specimen keeps the specimen dry, while the surrounding oil provides confinement pressure. To obtain low confinement pressures ($2 - 10$ KPa) we simply change the elevation of an oil reservoir connected to the oil in the chamber through a thin tube. To obtain higher confinement pressures we use an oil pump. The lower plate can be driven up by a stepping

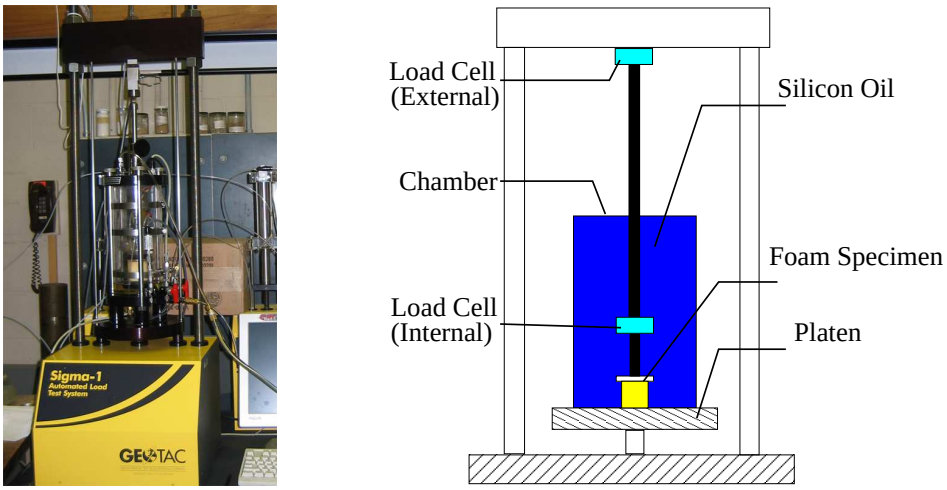

(a) (b)

Figure 3.2: (a) Photograph of the TurePath Automated Stress Path System. (b) Sketch of the TurePath Automated Stress Path System.

motor, providing uniaxial compression along the rise direction. The corresponding load is measured by an internal load cell (Interface 300 lbs range).

We use a series of five EPP foams of apparent density (mass per unit volume of foam) 50.3, 63.0, 77.0, 162.9 and 220.5 $\mathrm{kg/m^3}$. These foams are known to the manufacturer, General Plastics of Tacoma, WA, by the codes EF-4003, EF-4004, EF-4005, TF5070-10 and TF5070-13 respectively. The relative density ρ is defined as the apparent density ρ_a of the specimen divided by the density ρ_s of the base material. For the EF series, $\rho_s = 1700\,\mathrm{kg/m^3}$ whereas for the TF series $\rho_s = 2540\,\mathrm{kg/m^3}$. Thus the relative density is $\rho = 0.030$, 0.038, 0.046, 0.065, and 0.086 respectively for the EF-4003, EF-4004, EF-4005, TF5070-10 and TF5070-13 foam.

3.2.1 Error estimation

In our tests, we measure the force F with load cells and the displacement d with a transducer. For the purpose of error estimation, we consider a single characteristic length of the specimen, L, which is measured with a ruler. We define the axial stress as $\sigma = F/L^2$, and the propagation of errors gives

$$\Delta\sigma = |1/L^2|\Delta F + |2F/L^3|\Delta L.$$

The axial strain is defined as $\epsilon = d/L$, and the propagation of errors gives

$$\Delta\epsilon = |1/L|\Delta d + |d/L^2|\Delta L.$$

We estimate the error of L ($L \approx 10\,\text{cm}$) as 1 mm (relative error less than 1%), and the relative error of force and displacement as 3%. The relative error of the stress is

$$\Delta\sigma/\sigma = \Delta F/F + 2\Delta L/L = 5\%,$$

and the relative error of the strain

$$\Delta\epsilon/\epsilon = \Delta d/d + \Delta L/L = 4\%.$$

Thus the relative error of the stresses and the strains is about 5%.

3.3 Mullins effect

Polymeric foams exhibit a Mullins effect (Mullins, 1969) whereby the mechanical response in the first few loading cycles may differ from the nechanical response in successive cycles. Fig. 3.3 shows six load-unload cycles for foam specimens of relative density of $\rho = 0.046$; the specimens are subjected to uniaxial compression along the rise direction.

In the figure, the highest initial modulus and plateau stress occur during the first cycle. The second cycle exhibits a significant drop in the plateau stress, while the drop for the third and fourth cycles is relatively small. After four load-unload cycles, the response becomes stable. We find that after being at rest for 24 hours, the material recovers fully and the highest response can be repeated.

We also measure the Young's modulus for the compression along the rise direction (the slope of the initial linear part of stress-strain curve for uniaxial compression) of each foam specimen for 5 times (after 5 load-unload cycles, the measured Young's modulus are for the 6th to 10th loading), and calculate the standard deviation of the modulus. The results are

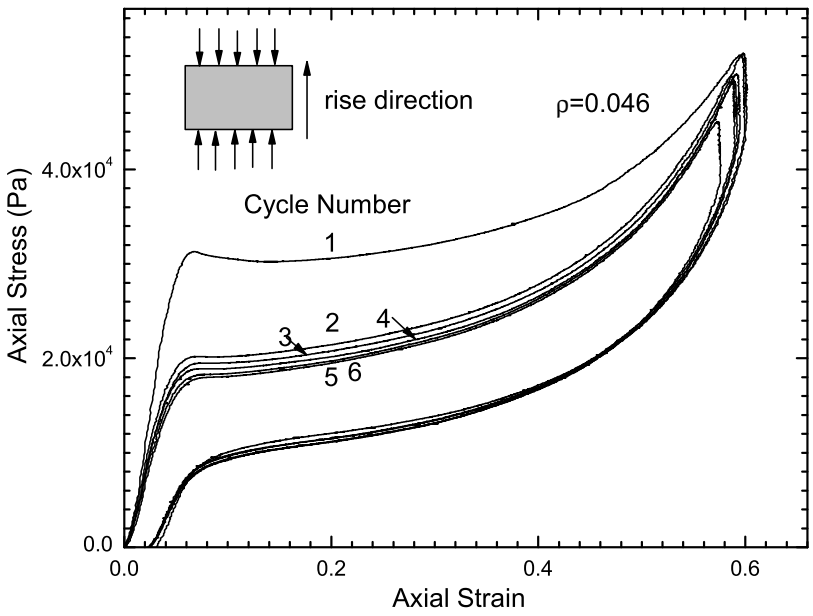

Figure 3.3: Stress-strain curves of 6 load-unload cycles, for an EPP foam of relative density $\rho = 0.046$ subjected to uniaxial compression along the rise direction.

Table 3.1: Measured Young's modulus for each specimen

Density (kg/m^3)	50.3	63.0	77.0	162.9	220.5
Modulus(KPa)	19.9 ± 0.6	31.8 ± 0.7	41.8 ± 0.5	68.0 ± 2.0	87.7 ± 2.8

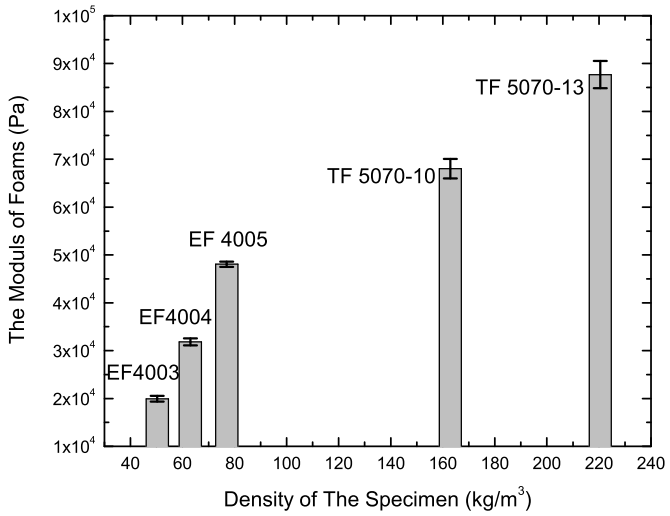

Figure 3.4: The modulus of foams specimens vs. the density

listed in table 3.1, and plotted in Fig. 3.4.

In order to eliminate the Mullins effect, in all of the experiments of Section 3.5 the specimens are subjected to at least five load-unload cycles before recording the stable response.

3.4 Global digital image correlation and its applications to foams

DIC is a non-contact, full-field surface strain-measuring method (Wang and Cuitiño, 2002). In this method, two digital images are taken before and after a deformation increment. The digital image taken before the deformation increment is mapped onto the digital image taken after the deformation increment, and a correlation function is used to quantify the goodness of the mapping. Then, the displacement field is calculated by determining the mapping that maximizes goodness. The strain field may be computed from the displacement field by taking derivatives.

Applications of DIC have included the measurement of velocity fields in seeded fluids (He

et al., 1984), the measurement of sintering shrinkage strains in powder compaction (Mizuno et al., 1995), the characterization of surface layer cracking in soils (Cardenas-Garcia et al., 1998), and the estimation of reliability in microelectronic packages (Lu , 1998). DIC has been used in conjunction with advanced instrumentation systems such as scanning electron microscope (SEM) and scanning tunneling microscope (STM) for quantitative material characterization (Lockwood et al. (1999)); Berfield et al. (2006)), and with high-speed photography for dynamic fracture studies (Chao et al., 1998). DIC has also been used for measuring strain fields in polymeric and metallic foams (Bart-Smith et al. (1998); Zhang et al. (1999); Bastawros et al. (2000); Wang and Cuitiño (2002)). Artificial speckles are commonly used to enhance the accuracy of the measurements, for example by imprinting a dot map or markers using SEM electron beams (Yongqi et al., 1996) or using Fluorescent dyes (Berfield et al., 2006), but in many cases the natural texture of the surface (of foam specimens, for example) provides enough information (speckles) to perform the correlation.

Conventionally DIC is a local method in that it is applied over a subset of pixels (the *correlation window*) of the region of interest. Thus the undeformed configuration is mapped into the undeformed configuration over a small portion of the region of interest. To cover the entire region of interest, DIC is applied over successive, partially overlapping correlation windows.

Here we use the finite-element based, global DIC method first introduced by Gao et al. (2002). In this method, a single finite-element interpolation is used to interpolate the displacement field over the entire region of interest. Both the displacement field and the strain field are smooth inside the finite elements and continuous across the boundaries of the finite elements (Gao et al., 2002). The undeformed configuration is mapped onto the undeformed configuration over the entire region of interest at once.

This global DIC method has been used is several studies, mostly involving metallic foams (Zhou et al., 2004, 2005a,b) and soft tissues (Cao et al., 2006, 2007; Gao and Desai, 2009). In the following sections, we perform a few calibration tests to ascertain the accuracy of our implementation of the method.

3.4.1 Translation calibration test

In this test, we calculate the rigid body translation of a foam specimen (of dimension 10 cm ×10 cm ×10 cm) using a global DIC code with 6-node finite elements. The foam surface is rough and textured, and we can produce a suitable speckle pattern (Fig. 3.5) by illuminating the foam surface with a stable fiber optic source (Mille Luce M1000 from StockerYale) at a low angle. We place the specimen on a modular translation stage (Newport M-460P series). The displacement of the stage can be controlled through a micrometer (SM-25 from Newport). During the test, the specimen is subjected to a horizontal displacement of 7 mm in 7 equal steps of 1 mm (10.1 pixels). For each step, we use a digital monochrome CCD camera (PULNiX TM-1300 progressive scan) with NaVITAR Zoom 700 lens to obtain 8-bit digital images of 1300 by 1030 pixels.

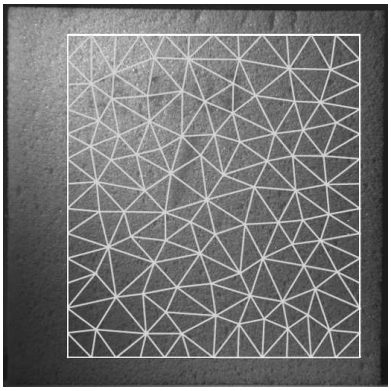

Figure 3.5: The foam specimen and the frame for global DIC

We then use the global DIC code to compute the displacement of the foam specimen from these images. In a region of 8.6 cm ×7.8 cm (863 pixels × 784 pixels) on the foam surface (see Fig. 3.5), the displacements of 6545 points are calculated. For the same set of images, we perform three computations with element sizes of 300, 150 and 65 pixels. The applied and calculated displacement for each step are listed in table 3.2. The error in the displacement is less than 1.3%, and the standard deviation is less than 1%.

Table 3.2: The applied and measured horizontal displacement

Applied Displacement (mm)		1.0	2.0	3.0	4.0	5.0	6.0
DIC results	Displacement	0.99	1.98	2.97	3.95	4.94	5.93
Element Size	Calculated (mm)	±0.01	±0.02	±0.03	±0.03	±0.04	±0.05
300 pixels	Error	1.0%	1.0%	1.0%	1.3%	1.2%	1.2%
DIC results	Displacement	0.99	1.98	2.97	3.95	4.94	5.93
Element Size	Calculated (mm)	±0.01	±0.02	±0.03	±0.03	±0.04	±0.05
150 pixels	Error	1.0%	1.0%	1.0%	1.3%	1.2%	1.2%
DIC results	Displacement	0.99	1.98	2.97	3.95	4.94	5.93
Element Size	Calculated (mm)	±0.01	±0.02	±0.03	±0.03	±0.04	±0.05
65 pixels	Error	1.0%	1.0%	1.0%	1.3%	1.2%	1.2%

Table 3.3: The rotation angle measured with global DIC

Applied rotation (°)		1.0	2.0	3.0	4.0	5.0	6.0
DIC results with	Calculated	0.99	1.95	2.94	3.95	4.92	5.93
element size	rotation(°)	±0.03	±0.04	±0.05	±0.07	±0.09	±0.10
of 300 pixels	Error	1.0%	2.5%	2.0%	1.3%	1.6%	1.2%
DIC results with	Calculated	1.00	1.97	2.96	3.97	4.94	5.95
element size	rotation(°)	±0.04	±0.05	±0.07	±0.11	±0.11	±0.13
of 150 pixels	Error	0.0%	1.5%	1.3%	0.8%	1.2%	0.8%
DIC results with	Calculated	1.00	1.98	2.97	3.98	4.95	5.95
element size	rotation(°)	±0.13	±0.18	±0.23	±0.28	±0.31	±0.38
of 95 pixels	Error	0.0%	1.0%	1.0%	0.5%	1.0%	0.8%

3.4.2 Rotation calibration test

To conduct this test, we place a foam specimen (of dimensions 10 cm × 10cm × 10 cm) on a rotation stage (RS65 from Newport). The rotation angle of the stage can be controlled through a micrometer. We apply a series of small rotations (1° for each step) and obtain digital images of the foam surface using the same set of instruments used in Translation Calibration Test. The rotation angle of each point can be calculated as

$$\gamma = \tan^{-1}[(\partial u/\partial y - \partial v/\partial x)/2],$$

where x and y are the coordinates of that point, while u and v are the displacements in x and y direction respectively. We then use the global DIC code with 6-node finite elements to calculate the rotation angle at 4970 points in a region of 7.5 cm ×7.7 cm on the foam surface.

For the same set of images, we perform three computations with element sizes of 300, 150 and 95 pixels. The results are shown in table 3.3.

The error in the rotation is less than 2.5% for all three element sizes. With a finer mesh

(decreasing element size), the global DIC gives more accurate results (mean value closer to the applied angle). However, the standard deviation increases with decreasing finite element size, a typical trade off in overdetermined problems; for the element size of 95 pixels, the standard deviation can be as high as 13%. The calculated rotation angle is more sensitive to the element size than the calculated transitional displacement.

3.4.3 A translation test performed on our experimental setup

To verify that the global DIC method can measure the displacement field accurately *in the very experimental setup to be used here*, we use the method to measure the vertical translation of a foam specimen placed in our testing system. The specimen (EF4003 of dimensions 10 cm × 10 cm ×10 cm) is put on the lower plate of ATS (Fig. 3.1) and translated upwards as a rigid body (i.e., without the specimen touching the upper plate). We take digital images of the foam surface at each position during a series of small translations.

We then calculate the displacements of 4690 points within a region of 8.0 cm × 7.6 cm on the foam surface using the global DIC code with 6-node finite elements. We also measure the displacement via the transducer mounted on the ATS machine. The results are listed in table 3.4.

From table 3.4 we see that the global DIC method captures the rigid body translation quite accurately. The largest difference between the measured and calculated displacements is about 3%. The standard deviation is less than 0.03 mm.

Table 3.4: Vertical displacements measured with Global DIC and the transducer

step	1	2	3	4	5	6	7
Displacement Measured with Transducer(mm)	2.60 ±0.02	5.05 ±0.02	6.35 ±0.01	7.45 ±0.02	9.01 ±0.01	10.1 ±0.02	11.3 ±0.01
Displacement Calculated with DIC(mm)	2.52 ±0.01	4.94 ±0.01	6.18 ±0.02	7.25 ±0.02	8.91 ±0.02	10.0 ±0.03	11.2 ±0.03
Error	3.1%	2.2%	2.7%	2.7%	1.1%	1.0%	0.9%

3.5 Experimental results

In order to eliminate the Mullins effect, in all of the experiments that follow the specimens are subjected to at least five load-unload cycles before recording the stable response (see Section 3.3 above).

All the DIC computations are performed using the global DIC code with 6-node finite elements of Section 3.4.

The estimated relative error of the stress and strain values reported here is about 5% (see Section 3.2.1 above).

3.5.1 Uniaxial compression along the rise direction

To prevent bulging (see Section 3.6 below), we use foam specimens of dimensions 5.0 cm× 10.0 cm× 10.0 cm. The height of 5.0 cm is along the rise direction.

We define the axial stress as the loading force divided by the original normal cross section area and the axial strain as the change of height divided by the original height of the specimen. We verify that the foam specimens are not strain-rate sensitive (Gioia et al., 2001), and use a constant loading rate of 0.3 cm/min for all the 5 foam specimens, which translates to a strain rate of 1×10^{-3} /s. The axial stress vs. axial strain curves are shown in Fig. 3.6.

The results clearly show a difference in the stress-strain response of low-density and high-density foams. For low-density foams ($\rho = 0.030, 0.038, 0.046$), three distinct regions of the response can be identified. For small strains ($\leq 5\%$), the stress-strain response is almost linear. This is followed by an extended stress plateau wherein the stress remains constant for increasing values of axial strain. For the lowest density specimen, the plateau is seen to extend up to almost 25% axial strain. Where the stress plateau ends, we recover a monotonically increasing stress-strain response and the stress starts to increase rapidly with increasing values of applied strain. The width of the stress plateau lessens with increasing density. For the high-density foams ($\rho = 0.065, 0.086$) no plateau is observed, and the stress

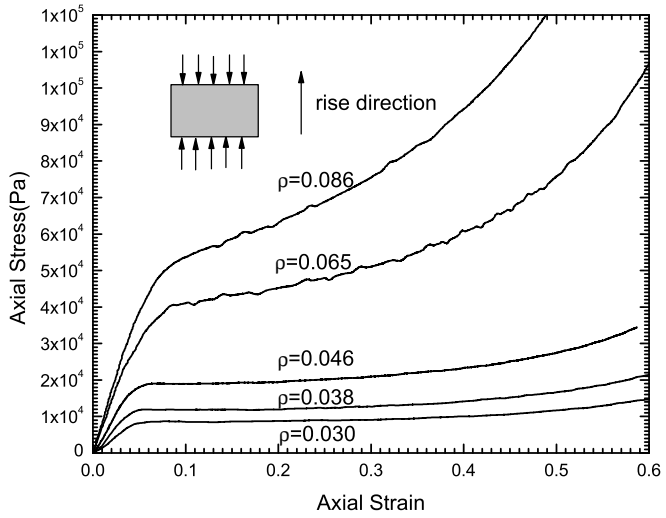

Figure 3.6: Axial stress vs. axial strain curves of foam specimens of five densities under uniaxial compression along the rise direction.

increases monotonically with the applied axial strain.

To obtain DIC data detailing the strain field evolution under uniaxial compression along the rise direction, we use specimens of dimensions 10 cm ×10 cm × 10 cm. The bigger surface of these specimens ensures that we get more comprehensive displacement field information. For low density foams with relative density $\rho = 0.038$, the stress–strain curves are similar for specimens of two sizes (Fig. 3.7).

During the loading process, we take 100 digital images of one lateral face of the specimen at equal intervals of loading path, and use the global DIC code to correlate the successive images, one pair at a time. Based on the correlation, the required displacement field is obtained for the lateral surface enclosed within a rectangular DIC frame which for this case measured 6.1 cm × 9.3 cm as shown in Fig. 3.7.. Contour plots of the vertical displacement field at different values of overall applied strain are shown in Fig. 3.8 for the low-density specimen with relative density $\rho = 0.038$. The results are obtained at axial strains of 4.5%, 9.0%, 14.8%, 22.5%, 32.1% and 44.9% which are marked with letter A to F in Fig. 3.7.

For the displacement contour plots, x and y are the horizontal and vertical coordinates

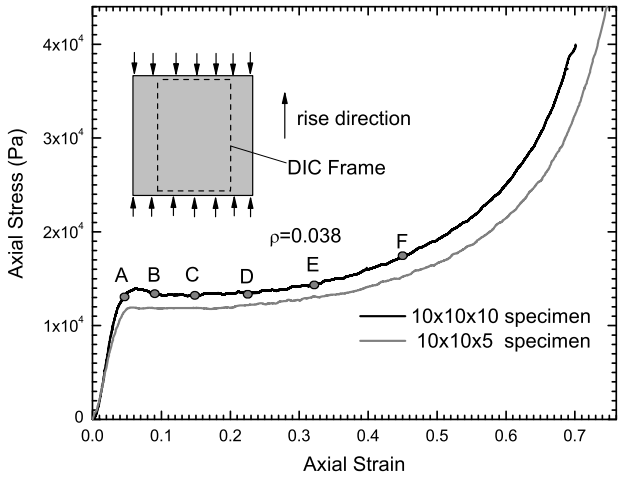

Figure 3.7: Axial stress vs. axial strain curve of the low density foam specimen under uniaxial compression along the rise direction.

of the image of the undeformed specimen face with a scale of 1 pixel = 0.1 mm. The lines within the image are contours of equal displacement plotted at increments of 0.77 mm. The minimum and maximum displacement in each plot is marked. The spacing between the contours gives an indication of the strain distribution in the specimen.

At low strains (pt. A) the contours are equidistant, indicating a homogeneous strain distribution through the sample. For strains that lie within the stress plateau (pt. B, C and D), the strain field shows a heterogeneous distribution with two preferred values of strain coexisting in the specimen. A high strain zone is seen near the center of the specimen and is bounded by two regions of relatively low strain. As the deformation proceeds, we see the volume fraction of the high strain zone growing at the expense of the volume fraction of the low strain zone. As the entire specimen switches to a high strain configuration, we recover a homogeneous field at pt. E, and the field remains homogeneous under further deformation.

To show the trend more clearly, we plot the displacement in y direction along a line on the foam surface (the dashed line shown in Fig. 3.8a). The results are shown in Fig. 3.9, For low and high values of applied strain (corresponding to pts. A and F on the stress-strain curve of Fig. 3.7), that the slopes (displacement/position) are uniform (straight lines in

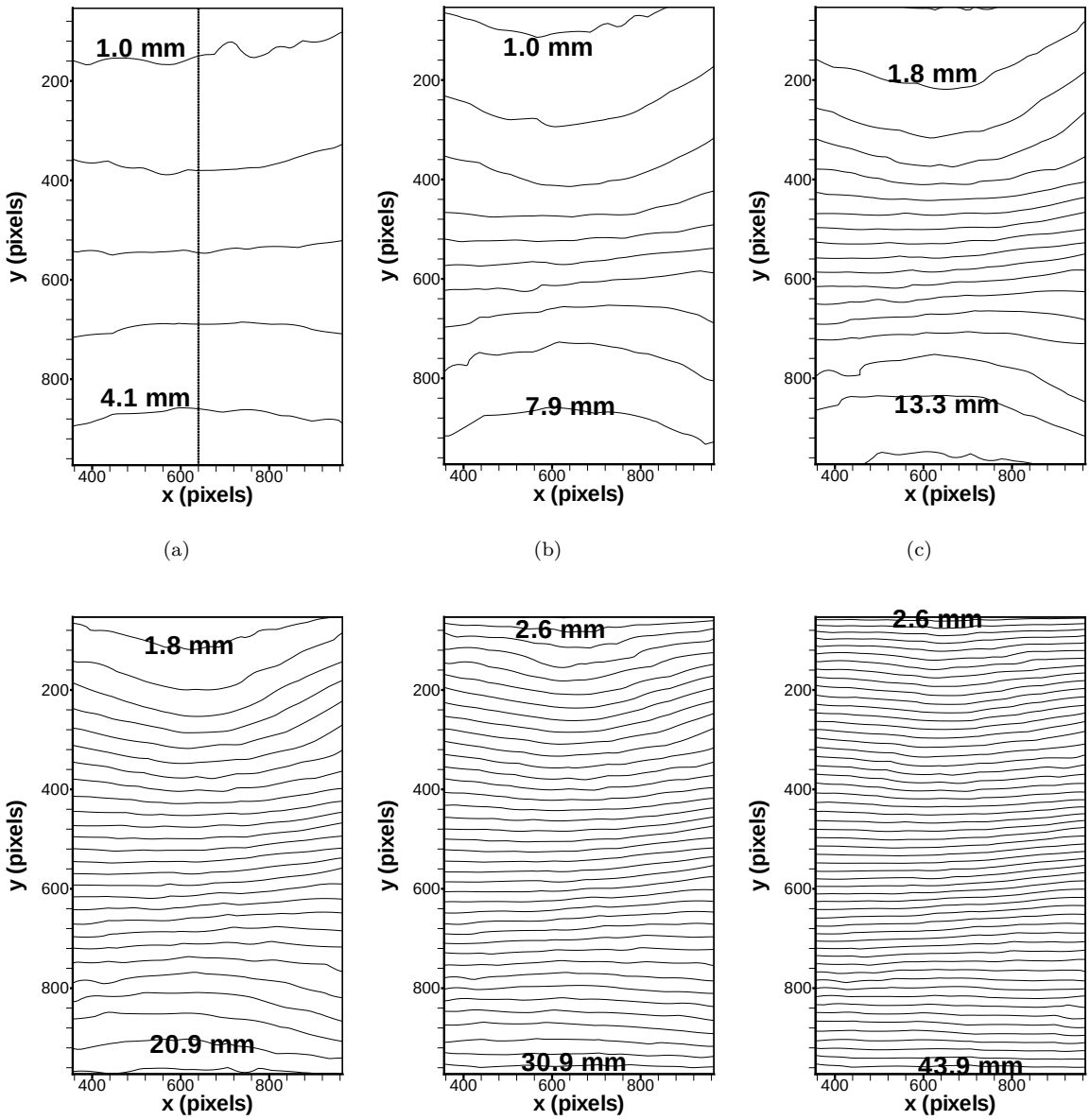

Figure 3.8: Contours of displacement along the rise direction for the foam of lower density.

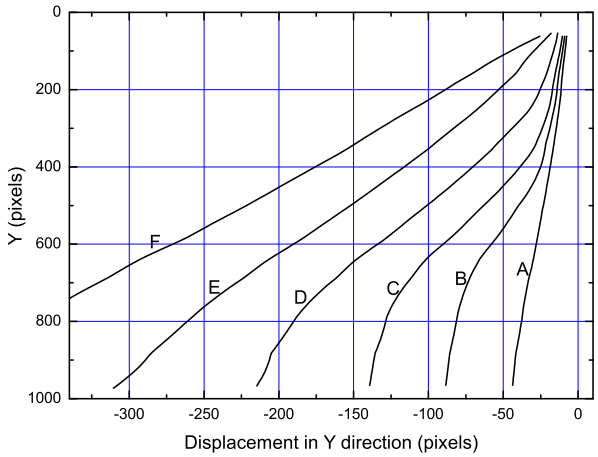

Figure 3.9: Plots of displacements in y direction of points on the foam surface along the dashed line drawn in Fig. 3.8a, corresponding to strain values of point A to F in Fig. 3.7.

Fig. 3.9), consistent with homogeneous strain fields across the whole face of the specimen. For intermediate values of applied strain (corresponding to pts. B, C, and D on the stress-strain curve of Fig. 3.7), the slopes are roughly bimodal, consistent with heterogeneous strain fields with two preferred values of local strain.

We construe the preferred values of local strain as two configurational phases of the foam (Gioia et al., 2001). These configurational phases of the foam coexist at a constant value of stress, which is the plateau stress.

The axial stress-strain curve for a high-density specimen is shown in Fig. 3.10, where the points A to F mark the axial strain, at which the corresponding DIC results shown in Fig. 3.11 were obtained. The DIC frame has a size of $7.5\,\text{cm} \times 6.0\,\text{cm}$, and the contours are plotted at intervals of 0.4 mm. The strain locations corresponding to points A to F are 4.2%, 10.3%, 16.3%, 22.3%, 28.4% and 46.4% respectively. In plots (a) to (f), the displacement field remains homogeneous throughout the specimen.

From the experimental results in this section, we conclude that a stress plateau is accompanied by two-phase strain fields, the lack of a stress plateau by homogeneous strain fields. These findings are in agreement with earlier findings under uniaxial compression along the rise direction.

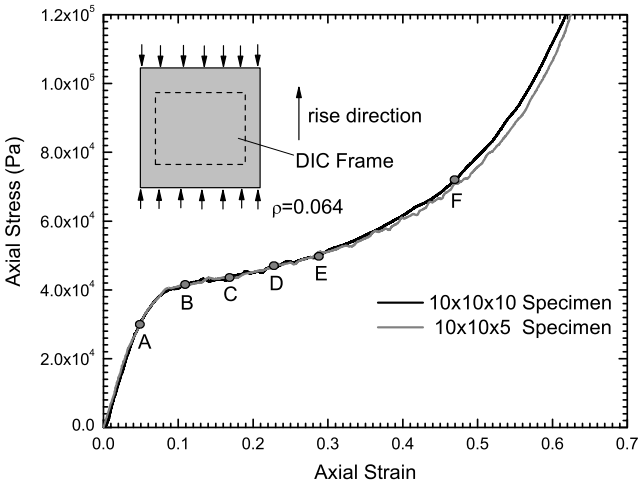

Figure 3.10: Axial stress vs. axial strain curve of the high density foam specimen under uniaxial compression along the rise direction.

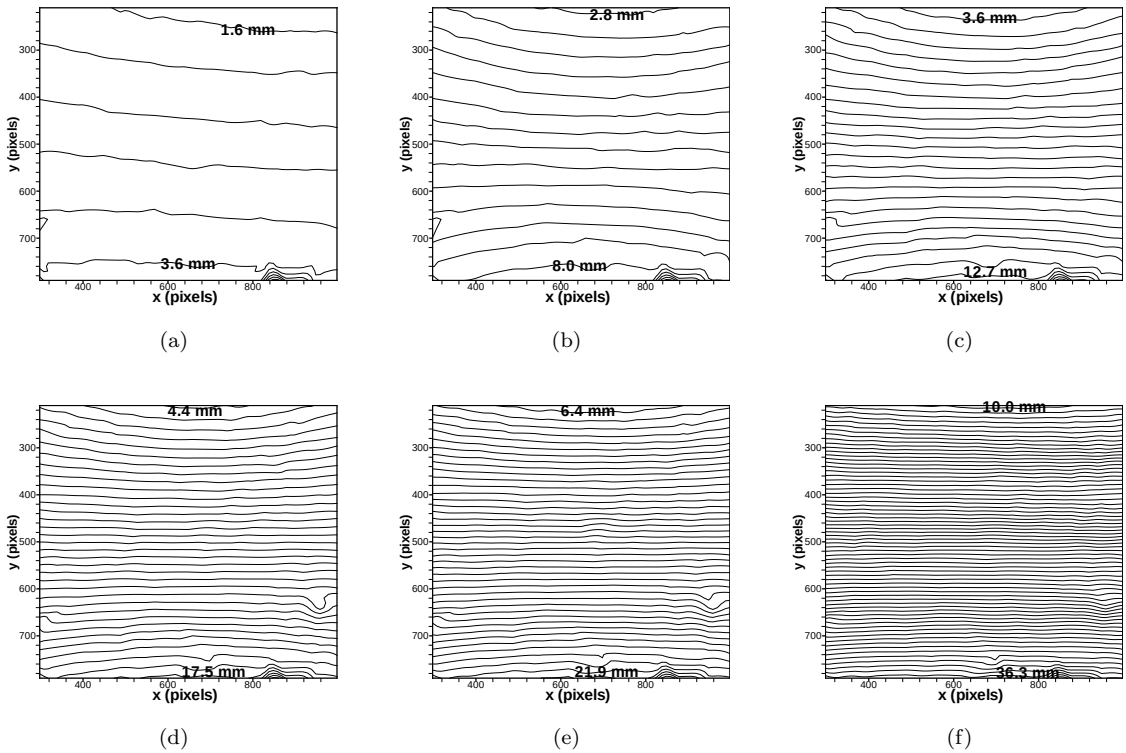

(a) (b) (c)

(d) (e) (f)

Figure 3.11: Contours of displacement along the rise direction for the foam of higher density under uniaxial compression along the rise direction.

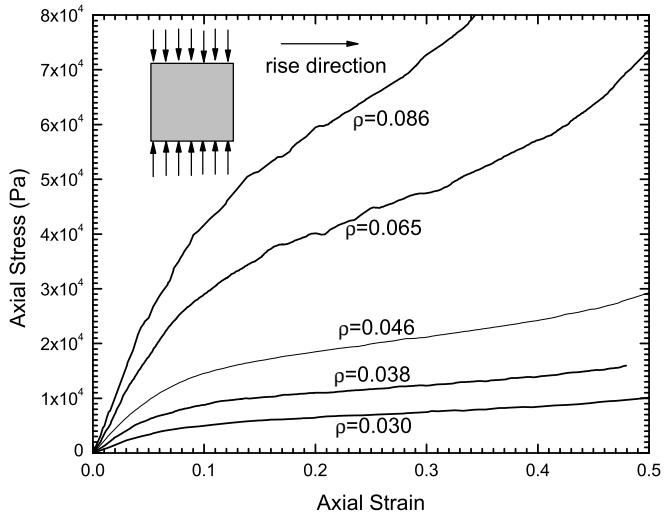

Figure 3.12: Axial stress vs. axial strain of foam specimens of five densities for uniaxial compression along one of the transverse direction

3.5.2 Uniaxial compression along transverse directions

As mentioned earlier, the manufacturing process of polymeric foams leads to an anisotropic microstructure where the bars of the cells are typically elongated along the rise direction. This leads to mechanical properties are quite different along transverse directions and along the rise direction.

In the compression tests along transverse directions, we use cubic specimens with dimensions $10\,\text{cm} \times 10\,\text{cm} \times 10\,\text{cm}$. The loading speed is $0.6\,\text{cm/min}$, and the strain rate is $1 \times 10^{-3}\,/\text{s}$, which is the same as that used for compression tests along the rise direction. The axial stress-strain curves are shown in Fig. 3.12. The stress-strain curves remain monotonically increasing in this case even for the lowest density specimens.

We compare the stress-strain response under compression along the rise direction against the stress-strain responses under compression along two mutually perperndicular transverse directions in Fig. 3.13. Fig. 3.13 indicates that the foam specimen is transversely isotropic and much stiffer under compression along the rise direction. A stress plateau is missing for loading along the transverse direction. These observation are consistent with a disparity in

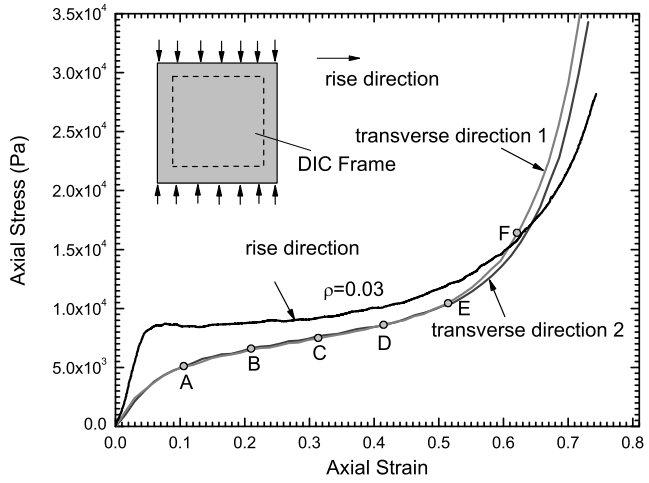

Figure 3.13: Axial stress vs. axial strain of the least dense foam specimen for uniaxial compression along the rise and transverse directions.

the deformation mechanism of the open-cell foam microstructure under compression along the rise and transverse directions.

To track the evolution of the deformation under transverse compression, we take digital images during the loading process for the least dense foam ($\rho = 0.030$), and use the global DIC code to compute the strain fields. The contour plots of vertical displacement (i.e., the displacement in the load direction) in a rectangular region of $7.6\,\text{cm} \times 7.5\,\text{cm}$ are shown in Fig. 3.14, where plots (a) to (f) correspond to average axial strains of 10.4%, 20.8%, 31.2%, 41.6%, 51.9% and 62.3% respectively. The displacement increment between the contours is 1.2 mm and the minimum and maximum displacements are labeled. Figure 3.13 shows the associated stress-strain curve. As expected, the strain is homogeneous throughout the specimen for all values of axial strain, consistent with the lack of a stress plateau.

From the experimental results in this section, we conclude that EPP foams are transversely isotropic, and their mechanical response depends not just quantitatively but also qualitatively on the direction of loading. Compression does not necessarily result in a stress plateau, even in foams of very low density. In agreement with our conclusion from the experimentl results of the previous section, the lack of a stress plateau is accompanied by

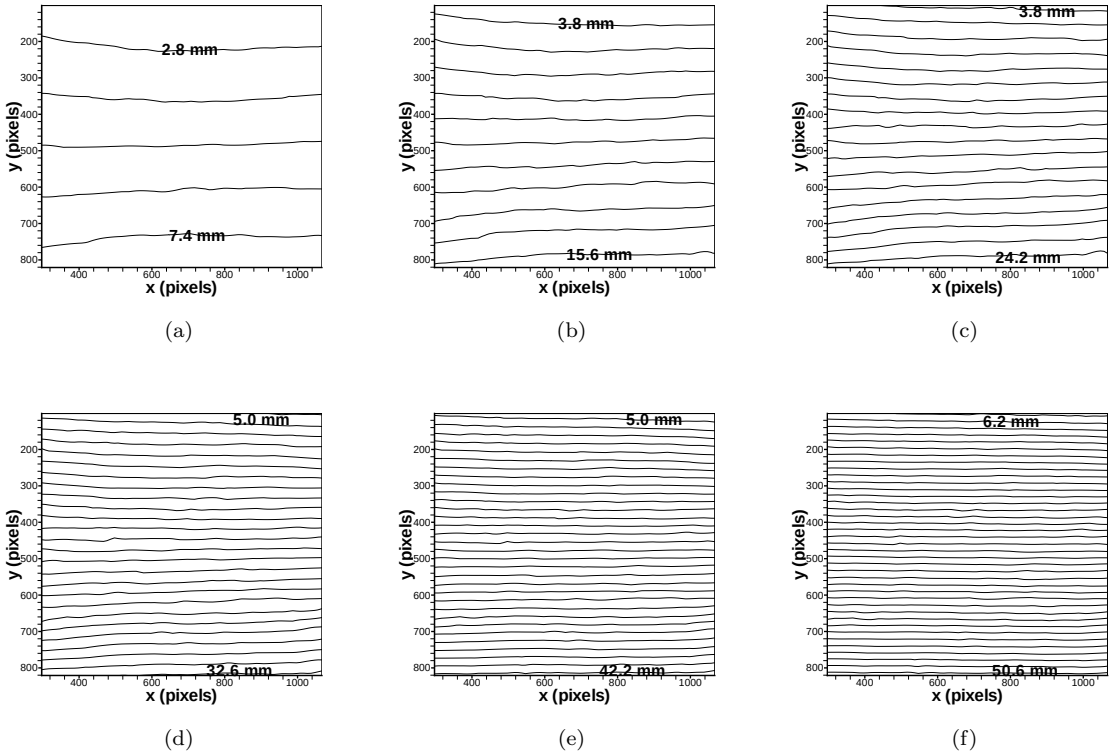

(a) (b) (c)

(d) (e) (f)

Figure 3.14: Displacement field for compression along the transverse direction.

homogeneous strain fields.

3.5.3 Tension

To conduct tension tests, the samples are cut into slender shaped blocks that measure $10\,\text{cm} \times 5\,\text{cm} \times 5\,\text{cm}$, with the longest dimension along the rise direction. We glue two wooden plates to the top and bottom of the specimen and these plates are in turn clamped to the loading plates of the ATS testing machine (Fig. 3.15a).

The loading speed is $0.4\,\text{cm/min}$ which amounts to a strain rate of $0.67 \times 10^{-3}\,/\text{s}$ for all the specimens. The stress-strain results under tension are show in Fig. 3.16. The trend of the tensile response is seen to be similar for low and high-density foams. The response remains almost linear for small axial strains and slowly softens as we go beyond about 5% strain. As the tensile deformation increases we observe indication of microstructural damage on the specimen surface as the solid bars that constitute the microstructure start

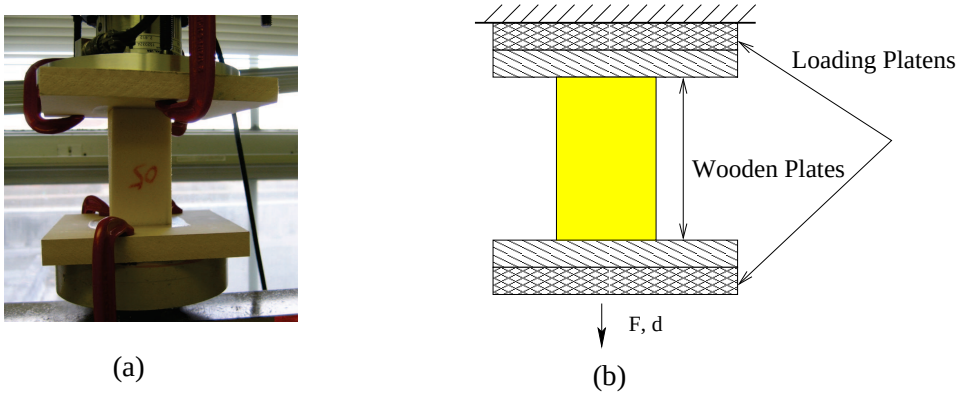

Figure 3.15: (a) Tension test specimen and set up. (b) Sketch of the set up.

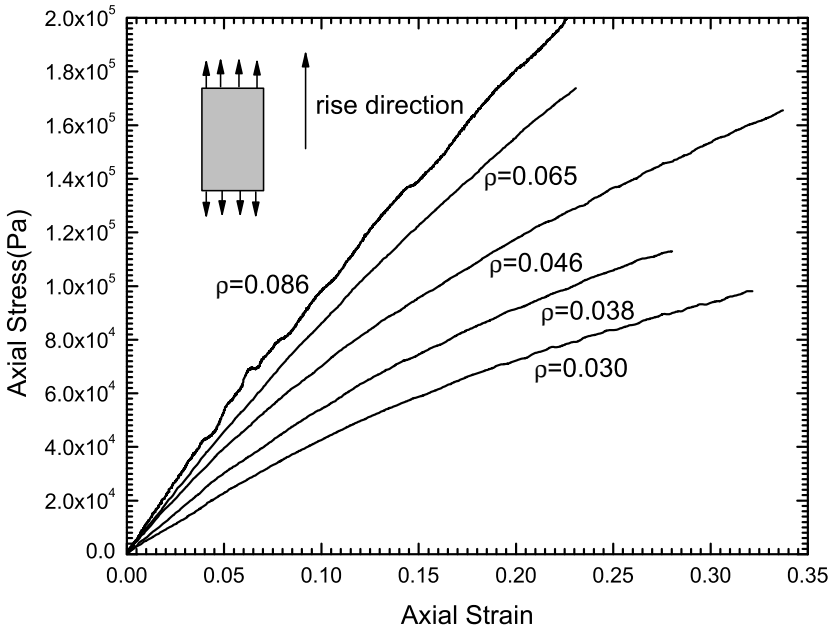

Figure 3.16: Axial stress vs. axial strain of foam specimens of five densities for uniaxial tension along the rise direction.

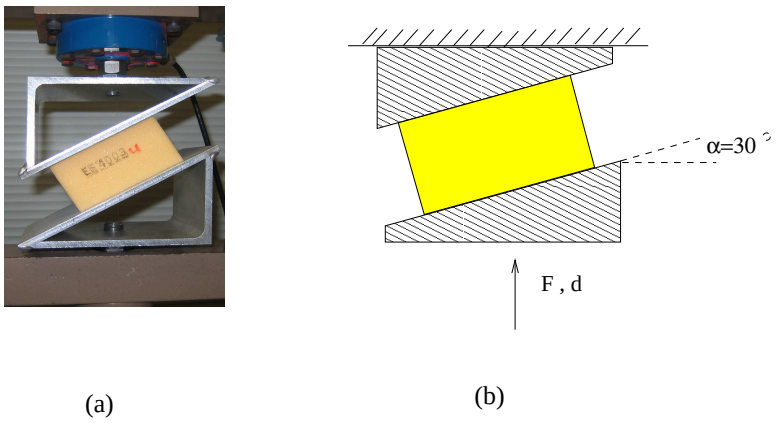

Figure 3.17: (a) Compression loading test set-up. (b) Sketch of the set up

to rupture. As the damage accumulates, a macroscopic crack initiates from the edge and quickly propagates throughout the specimen causing rupture. We assume that the softening in the tensile response might be caused by a combination of material nonlinearity and the damage in the internal microstructure as the solid bars start to break under increasing tensile strains.

From the experimental results in this section, we confirm that the mechanical response of EPP depends not just quantitatively but also qualitatively on the direction of loading. Regardless of the density of the foam, tension does not result in a stress plateau.

3.5.4 Combined compression and shear loading

We obtain experimental results for a biaxial loading case. In this loading case, we subject the foam specimens to a combination of compression along the rise direction and shear along faces in contact. To achieve this, we replace the two flat loading plates of the ATS machine with two wedge-shaped plates (Fig. 3.17). The angle of the wedge-shaped plates is 30 °. As the lower plate is pushed upward, the specimen is subjected to a combination of shearing load and compression along the rise direction.

The specimens are the same as those described earlier for uniaxial compression along the rise direction, and the loading speed is 0.3 cm/min. The vertical force-displacement curves (Fig. 3.18) obtained in this case have a trend reminiscent of the results obtained for

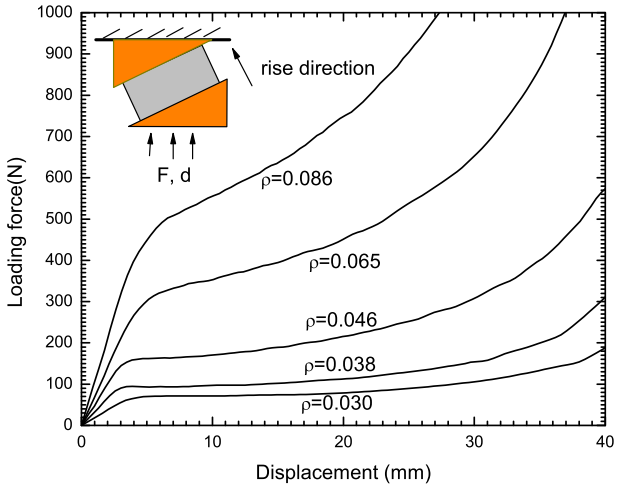

Figure 3.18: Vertical force vs. vertical displacement for foam specimens of five different densities for the compression and shear combined loading.

uniaxial compression along the rise direction. The low-density specimens exhibit a force plateau where the vertical force remains almost constant. This feature is absent in the two high-density specimens.

To obtain DIC data detailing the strain field evolution under combined loading, we use specimens of dimensions 10 cm × 10 cm × 10 cm. For low-density foams with relative density $\rho = 0.038$, the vertical force vs. normalized vertical displacement curves are similar for specimens of two sizes (see 3.19).

We take digital images during the loading process, and use the global DIC code to compute the strain fields for a low-density foam. The contour plots of displacement along the rise direction (also the direction of compression) are shown over a rectangular region of 8.6 cm × 8.3 cm in Fig. 3.20, where x and y are the horizontal and vertical coordinates of the image of the undeformed specimen face with a scale of 1 pixel = 0.1 mm. The displacement increment between the contours is 0.4 mm. The plots (a) to (f) of Fig. 3.20 correspond to a vertical displacement of 3.0 mm, 7.6 mm, 17.3 mm, 23.6 mm, 28.9 mm and 42.1 mm, respectively; they also correspond to the points marked A to F on the force-displacement curve of Fig. 3.19. These results are similar to the results for low-density density foams under

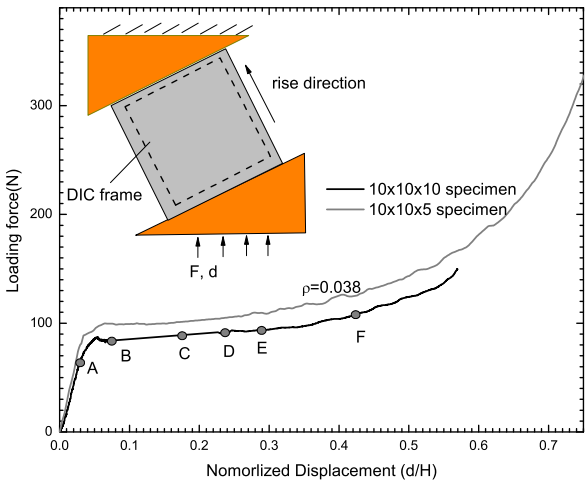

Figure 3.19: Vertical force vs. vertical displacement curves for specimens with dimensions 10 cm $\times$ 10 cm $\times$ 10 cm and 10 cm $\times$ 10 cm $\times$ 5 cm, subjected to compression and shear combined loading. The displacement is normalized by dividing the specimen height.

loading along the rise direction. A stress plateau is accompanied by heterogeneous strain field with two preferred values of strain. The preferred values of strain, which we interpret as characteristic configurational phases of the foam, may be discerned more clearly in Fig. 3.21, where we plot the displacement in the y direction (rise direction) along a straight line on the surface of the specimen (the dashed line shown in Fig. 3.20b).

From the experimental results in this section, we confirm that a stress plateau is accompanied by two-phase strain fields, the lack of a stress plateau by homogeneous strain fields. Fruther, we conclude that the classification of foams into low-density foams (where stress plateaus and two-phase fields are observed) and high-density foams (where neither stress plateaus nor two-phase fields are observed) holds consistently: the same three foams of lower density, and then only those three foams, displayed a stress plateau under both uniaxial compression along the rise direction and combined shear and compression.

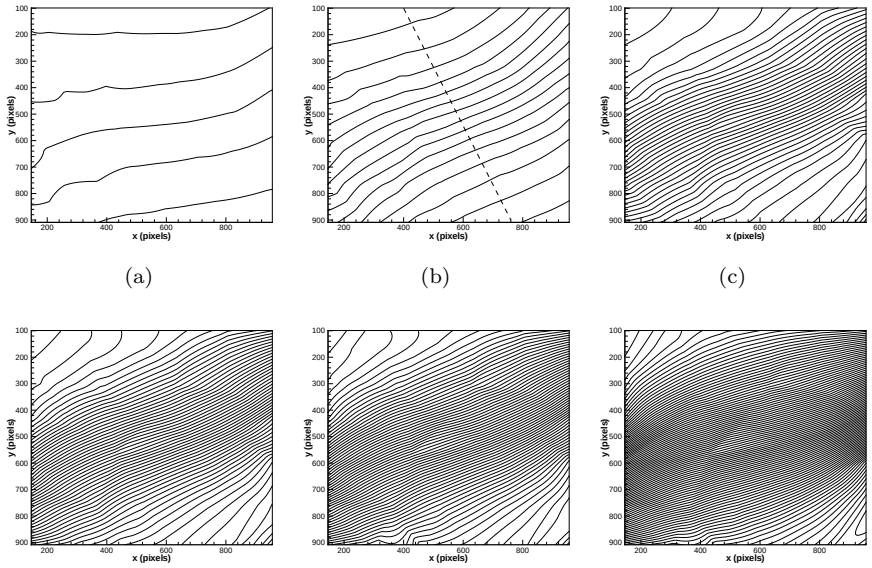

Figure 3.20: Displacement field for compression and shear combined loading of low density foam specimen of size $10\,\text{cm} \times 10\,\text{cm} \times 10\,\text{cm}$

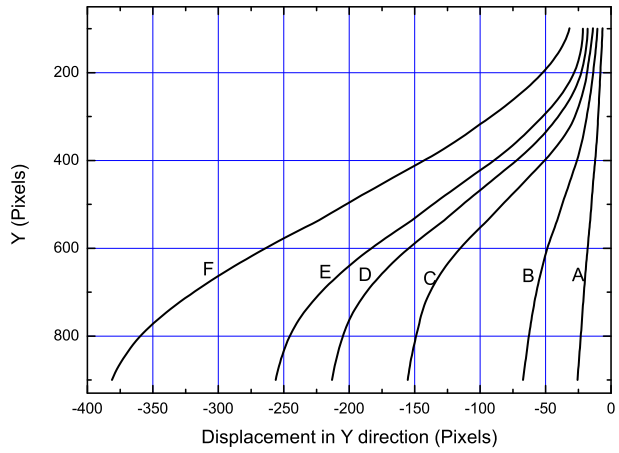

Figure 3.21: Plots of displacements in the y direction of points on the foam surface along the dashed line drawn in Fig. 3.20b, corresponding to strain values of point A to F in Fig. 3.19.

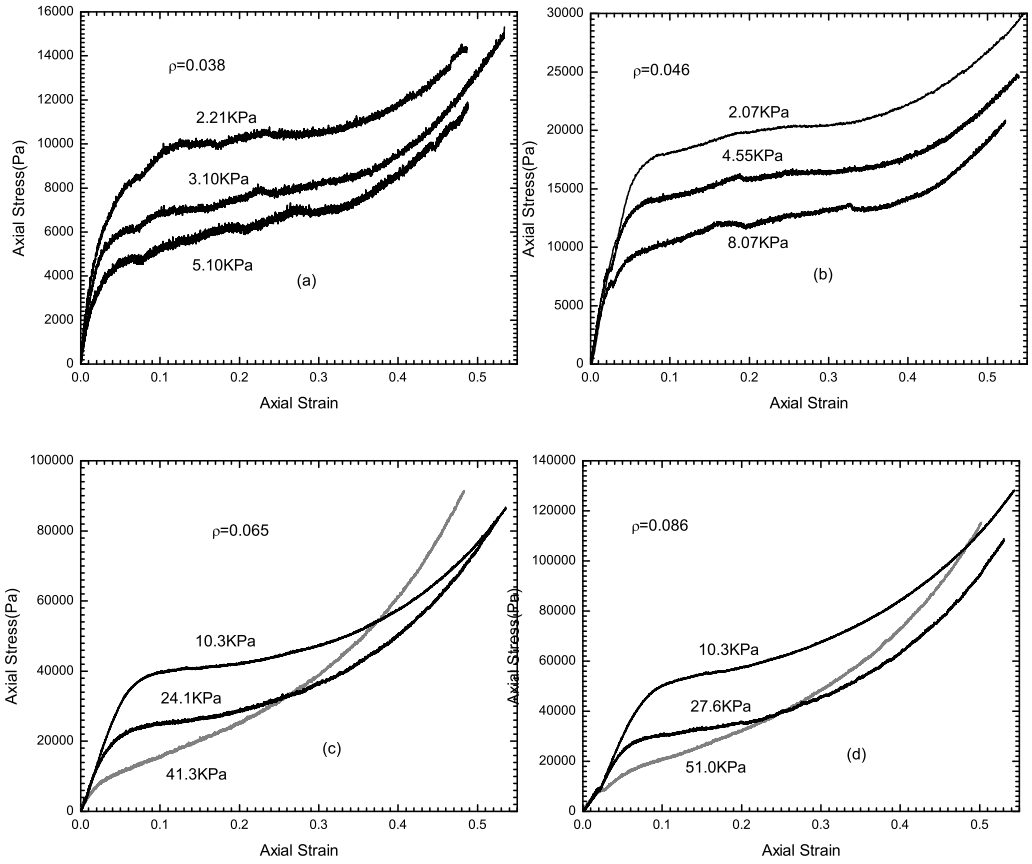

Figure 3.22: Vertical force vs. vertical displacement curves for triaxial loading

3.5.5 Triaxial testing

We use the TruePath Automated Stress Path System with cylindrical specimens of height 4.9 cm along the rise direction and a diameter of 5.1 cm. A specimen is loaded in two steps. First, the specimen is enclosed in a protective membrane and immersed in a chamber filled with oil. The weight of the surrounding oil applies an approximately hydrostatic pressure to the specimen. Due to the specimen height, a pressure gradient exists along the specimen surface. The pressure difference between the top and bottom of the specimen can be calculated from $\Delta p = \rho g \Delta h = 480\,\mathrm{Pa}$, where $\rho = 0.96 \times 10^3\,\mathrm{kg/m^3}$ is the density of the silicon oil used in the chamber, $g = 9.8\,\mathrm{m/s^2}$ is the gravity acceleration and $\Delta h = 5.1\,\mathrm{cm}$ is the height of the specimen. For smaller values of confinement pressure, the pressure gradient results in some deviation from the measured pressure value. For example, for the lowest confinement pressure, the measured value using a pressure gauge placed at a height that corresponds to the center of the specimen is $p = 1.59\,\mathrm{KPa}$. The percentage deviation from the measured value decreases for higher values of confinement pressure.

Second, the specimen is uniaxially compressed along the rise direction by moving up the lower plate. In order to keep the confinement pressure constant during the loading process, we use a very slow loading rate of $0.0127\,\mathrm{cm/min}$ which corresponds to a strain rate of $4.15 \times 10^{-5}\,/\mathrm{s}$.

In the first stage of loading, the only non-zero stress components are $\sigma_{11} = p, \sigma_{22} = p, \sigma_{33} = p$, where p is the confinement pressure. As we compress the specimen while keeping the confinement pressure constant the stress component σ_{11} changes to $\sigma_{11} = p + \sigma$, where σ is obtained by dividing the axial force measured with the internal load cell by the cross section area.

We use three different confinement pressures for each specimen. Plots of the axial stress vs. axial strain are shown in Fig. 3.22.

The results show a consistent trend for all the cases. For a given value of axial strain, the corresponding stress decreases with increasing values of the initial confinement pressure. The

initial confinement pressure leads to a softer response. Very high values of initial confinement pressure seem to change the stress-strain response (curves in gray in Fig. 3.22A, D, and E which correspond to a confinement pressure of 57.9 KPa, 41.3 KPa and 51.0 KPa for for specimens of relative density $\rho = 0.030$, $\rho = 0.065$ and $\rho = 0.086$ respectively).

3.6 The bulging of foam specimens elucidated via the global DIC method

During uniaxial compression tests we have observed a frequent phenomenon of *bulging*, whereby the specimen starts to bend and eventually forms a sharp cusp on one side. The phenomenon occurs only in low-density EPP foams, and only where the compression is along the rise direction For foam specimens of higher densities, there is no bulging.

An example of bulging is shown in Fig. 3.23, where a cubic foam specimen is compressed with a constant loading rate of 0.1 mm/sec (or strain rate of 1×10^{-3}/sec) on the ATS testing machine.

To study the bulging in some detail, we use global DIC to calculate the displacement field of a region of size 7.7 cm $\times$ 8.2 cm on the surface the foam specimen. During loading, we take a series of digital images of the foam surface. Between any two consecutive images, the time interval is 5 seconds, and the displacement of the loading plate is 0.5 mm. We take a total of 140 images.

We then use the global DIC code with 6-node finite elements to compute the displacement field. The finite element size is 130 pixels (about 1.3 cm on the foam surface). The foam specimen and the finite element mesh are shown in Fig. 3.24.

We calculate the displacement field of all 140 steps. A few of the deformed finite element meshes are shown in Fig. 3.25.

The contours of the displacement along the loading direction (vertical direction of Fig. 3.24) are shown in Fig. 3.26, where the displacement contours of (a) to (f) are drawn on the undeformed configuration (Lagrangian coordinates) and correspond to the deformation of

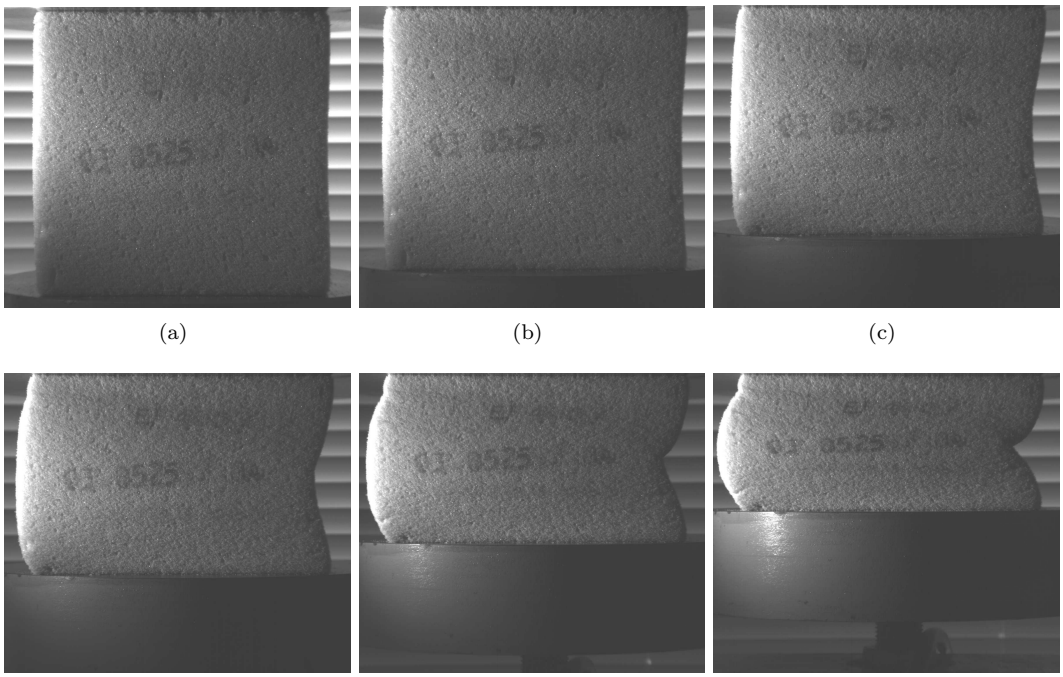

(a) (b) (c)

(d) (e) (f)

Figure 3.23: The bulging that occurs during uniaxial compression of a foam specimen of density $50.3\,\mathrm{kg/m^3}$ and dimensions $10\,\mathrm{cm} \times 10\,\mathrm{cm} \times 10\,\mathrm{cm}$. The pictures in (a) to (e) are the deformed foam surface at average stretch (the height of the deformed specimen divided by the original height) of 1 (undeformed), 0.910, 0.790, 0.701, 0.591 and 0.481, respectively

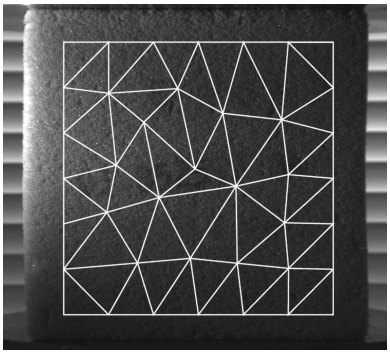

Figure 3.24: The foam specimen and the finite element mesh used for global DIC.

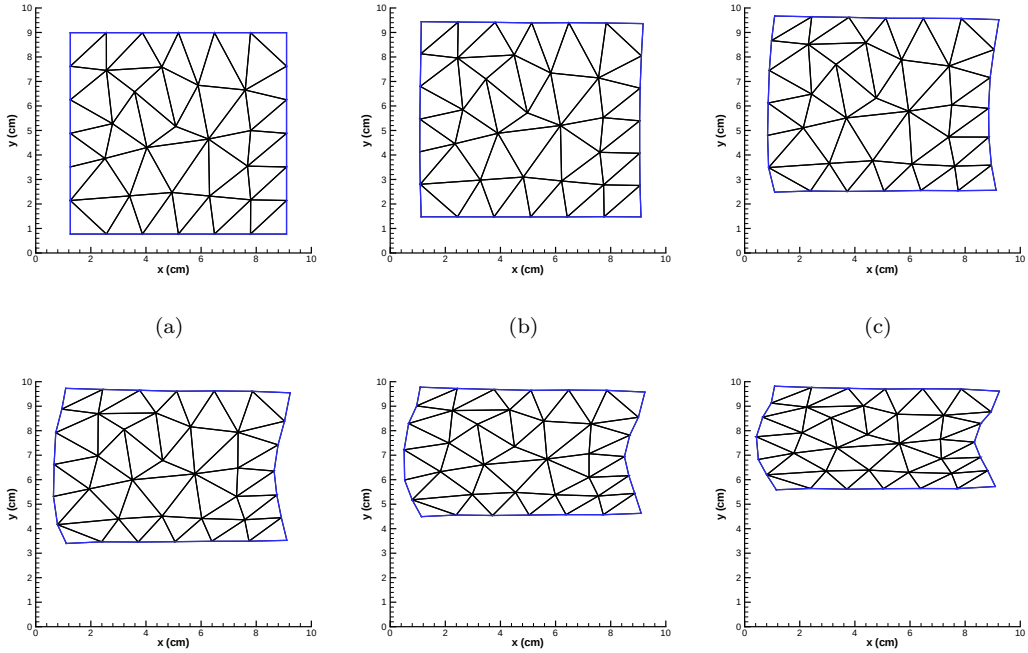

Figure 3.25: The deformed mesh calculated with global DIC. Figures (a) to (e) correspond to the deformed foam surfaces (a) to (e) in Fig. 3.23, respectively

Fig. 3.23(a) to (f), respectively.

In Fig. 3.26(b), the contours are uniformly distributed, indicating that the strain field is initially homogeneous and stratified. From Fig. 3.26(c) to (e), one can see the contours at the top and bottom strata are closer together than those in the central stratum, with the implication that the deformation gradient (or strain) is higher in the top and bottom strata. We interpret the high deformation gradient strata as strata in which the high-density phase prevails, and the low deformation gradient stratum as a stratum in which the low-density phase prevails.

The volume fraction of the high-density phase grows at the expense of the volume fraction of the low-density phase, until all the surface is covered by the high-density phase (Fig. 3.26). Thus the low-density stratum becomes sandwiched between two relatively stiff high-density strata. Then, geometrical imperfections induce horizontal forces which tend to sway the relatively compliant low-density stratum. Actuated by these horizontal forces, the low-density stratum deforms readily in the horizontal direction and causes the specimen to bend

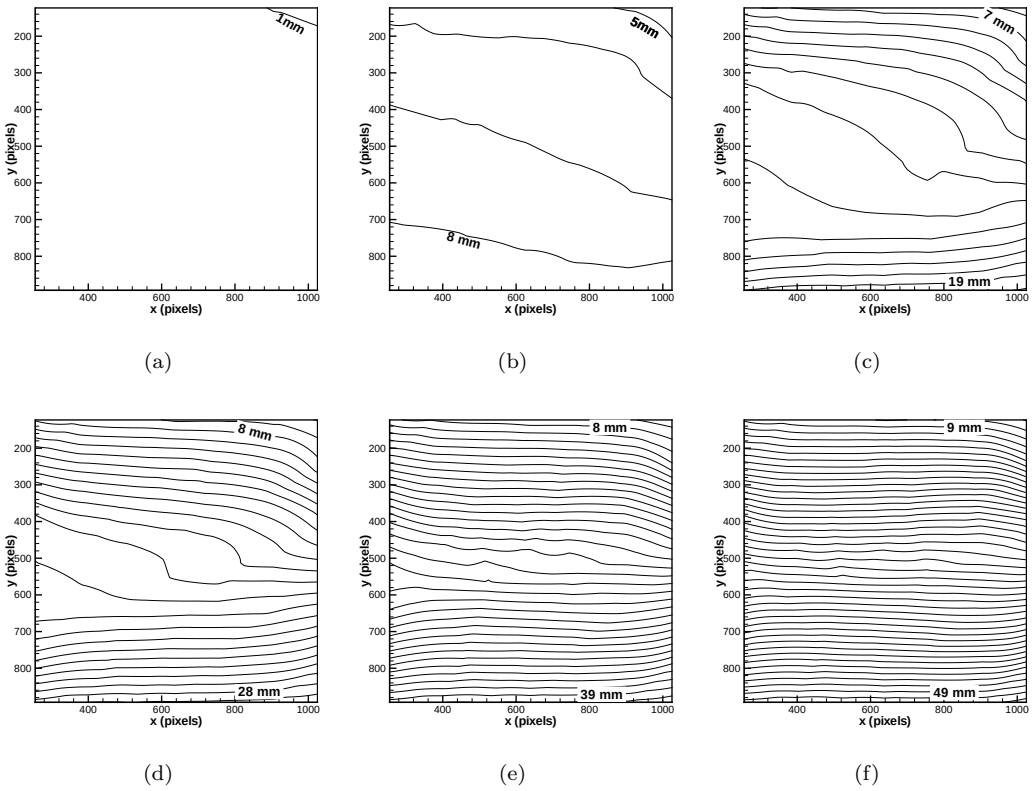

Figure 3.26: Contours of constant displacement in the loading direction. The displacement of one contour differs from the displacement of a contiguous contour by 0.1 cm; the displacement of some of the contours are marked (in cm). The contour plot (a) to (e) corresponds to the deformed foam surface (a) to (e) of Fig. 3.23 respectively

and eventually to form a cusp on one side af the speciment, and a bulge on the other side.

We conclude that bulging is closely associated with the occurrence of a phase transition; to avoid bulging where the direction of loading coincides with the rise direction, one must use specimens that are relatively short in the rise direction (as we have done in Section 3.5).

In this example, the global DIC code with 6-node finite elements is able to capture the very large (up to compression strain of 70%) nonuniform deformation of the bulging foam specimen. It also affords insight into the mechanism of bulging and the formation of cusps in low-density foams.

3.7 Discussion

Four observations about the current state of research on elastic polyether polyurethane (EPP) foams have guided us in designing the experiments of this chapter.

1. Most practical applications of EPP foams involve multiaxial loading, yet there has been scant research on the mechanical response of EPP foams under multiaxial states of stress.

2. The mechanical response of an EPP foam depends not just quantitatively but qualitatively on the relative density of the foam, yet no experiments have been reported for a set of EPP foams of widely differing densities.

3. EPP foams are commonly subjected to large strains under service conditions, yet measurements of complete stress-strain curves have remained scarce and mostly limited to uniaxial tests.

4. A stress plateau appears to be invariably accompanied by heterogeneous strain fields, yet measurements of the strain fields have only been performed in a few uniaxial tests.

With these observations in mind, we have conducted an unprecedented set of experiments on a series of commercially available EPP foams of five apparent densities ranging from 50.3 to 220.5 $\mathrm{kg/m^3}$. Each foam was subjected to five different loading cases, namely, uniaxial

compression along the rise direction, uniaxial compression along the transverse direction, tensile loading, biaxial loading with a combination of shear and compression, and a triaxial loading case which combined hydrostatic pressure with uniaxial compression along the rise direction.

For each test we have reported a complete stress–strain curve or force–displacement curve up to large strains on the order of 0.5. These curves are suitable for use in the calibration of theoretical models of EPP foams.

The mechanical response of EPP foams is transversely isotropic on a plane perpendicular to the rise direction, even under large strains.

A stress plateau occurs only for some types of loading: among the types of loading we have tested, compression along the rise direction and combined shear and compression along the rise direction. For other types of loading, there is no stress plateau, even for the foam of lowest density among those tested. The presence of at least one compressive eigenstress appears to be a necessary, but is not sufficient, condition for the occurrence of a stress plateau.

Fruther, the same three foams of lower density, and then only those three foams, display a stress plateau under both compression along the rise direction and combined shear and compression along the rise direction, with the implication that the classification of EPP foams into low-density foams and high-density foams holds consistently regardless of the type of loading.

For a few loading cases, we have measured the evolution of the strain field using a global DIC technique. The results lend support to the conclusion that a stress plateau is invariably accompanied by the development of heterogeneous two-phase strain fields within the foam specimen, whereas the lack of a stress plateau is invariably accompanied by homogeneous strain fields. This is a constraint that any plausible theoretical model should satisfy, yet its importance has not been recognized. We return to this constraint in Chapter 4, where we use the experimental results of this chapter to calibrate a 3D model of EPP foams.

Chapter 4

A 3D mean-field model of EPP foams

In Chapter 2, we provided a theoretical framework for this research by introducing a number of mean-field models for uniaxial compression. Here we propose a mean-field model for multiaxial stresses and calibrate the model using the experimental results of Chapter 3. Our purpose is to predict the entire multi-axial loading behavior of elastic polyether polyurethane foams in a wide range of densities.

4.1 Introduction

In models of foams, the foam microstructure is frequently idealized as a perfectly regular, periodical network of bars. This periodic network of bars can be constructed from a representative substructure, which is repeated periodically to fill space. The mean field assumption is that the substructure deforms in a way that is affine with the applied mean stretch or strain.

The representative substructure, which can be a single foam cell or an idealized cell vertex, is often called a unit cell. Both two dimensional (Patel and Finnie, 1970; Gibson et al., 1982a; Warren and Kraynik, 1987) and three dimensional unit cell models (Gibson et al., 1982b; Warren and Kraynik, 1988; Zhu et al., 1997; Wang and Cuitiño, 2000; Sullivan et al., 2008) have been proposed. These models have been used to predict the mechanical properties of foams, such as the compressive or shear modulus, and the initial "yield" point for compressive loading. In a few cases (Papka and Kyriakides, 1994; Gong and Kyriakides, 2005), the stress-strain curves predicted by these models have been compared with stress-strain curves measured in uniaxial experiments, but only for a single density or densities in

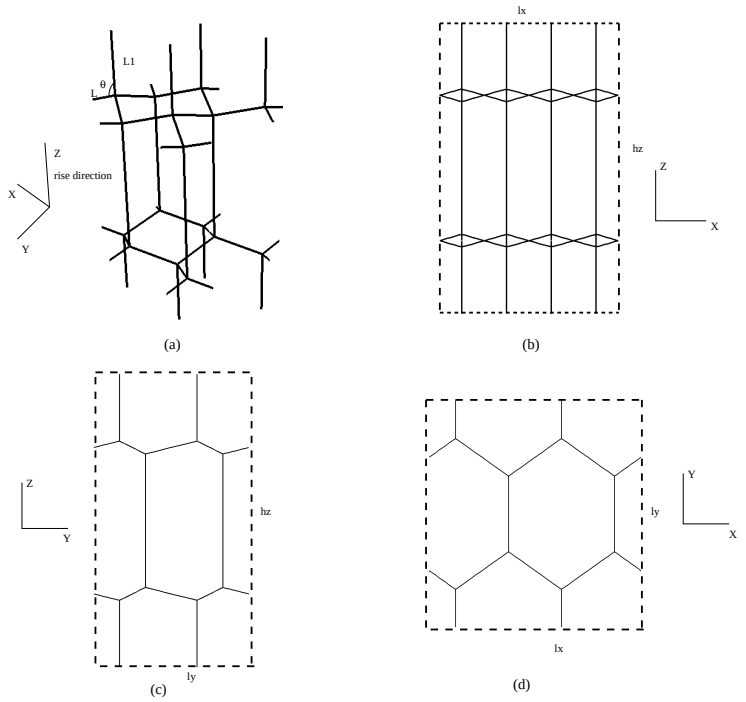

Figure 4.1: The idealized foam representative microstructure. (a) 3D view of the foam microstructure. (b) Front view. (c) Side view. (d) Top view.

a very narrow range.

4.2 Formulation

4.2.1 Geometry of the model

The foam is idealized as a regular network of bars arranged as tetrahedral units (see Fig. 2.1a). In each one of these four-bar tetrahedral cells, one bar of length L_1 is aligned with the rise direction of the foam and the other three bars of length L form an angle θ (in the undeformed cell) with the rise direction (Fig. 4.1a).

The network of bars can be divided into different representative substructures that can be packed to fill space without rotation. For the minimum representative substructure, see Sabuwala et al. (2007); their unit cell contains 2 four-bar tetrahedral units, and occupies a triangular prism in space.

Here we choose a representative substructure containing 16 four-bar tetrahedral units

(Fig. 4.1a). As one can see from the front, side and top views in Fig. 4.1b, c and d, this substructure consists of a parallelepiped. The dimensions of this parallelepiped can be calculated using the following expressions:

$$\begin{aligned} l_x &= 4L\sin(\theta)\cos(\pi/6), \\ l_y &= 3L\sin(\theta), \text{and} \\ h_z &= 2L_1 + 2L\cos(\theta). \end{aligned} \tag{4.1}$$

Assuming the bars in our model have the same cross sectional area A, the relative density of the foam can be calculated as:

$$\rho = \frac{A(L_1 + 3L)}{3\sin^2(\theta)\cos(\pi/6)(L_1 + L\cos\theta)}. \tag{4.2}$$

The moment of inertia of the bars depends on the cross section area A in the form:

$$I_x = I_y = \gamma A^2, \tag{4.3}$$

where the dimensionless coefficient γ can be interpreted as a material constant.

4.2.2 Parameters of the model

The bars are assumed to be elastic beams made of an isotropic linear elastic material of Young's modulus E. Thus the parameters of the model are E, ν, L, L_1, A and γ.

Each one of these parameters has a clear physical meaning, and for any given EPP foam a value can be readily estimated for each parameter. The Young's modulus E and the Poisson's ratio ν can in principle be ascertained by testing small specimens extracted from the miscrostructure of the foam, or at least estimated from bulk specimens of the polyether polyurethane. The geometrical parameters L, L_1, A and γ can be estimated from microphotographs of the microstructure.

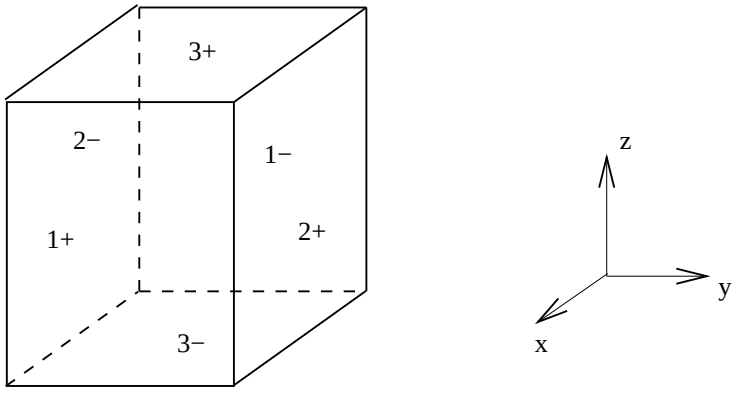

Figure 4.2: The boundary faces of the substructure

4.2.3 Boundary conditions

The substructure is subjected to periodic boundary conditions. In our substructure, the matching nodes are the couple of nodes which are on opposite boundary faces. For each pair of boundary faces (Fig. 4.2), we choose a reference pair of matched nodes. With reference nodes, the general periodic boundary conditions can be expressed as follows:

$$\begin{cases} U_i^{j+} - U_i^{j-} &= U_{iref}^{j+} - U_{iref}^{j-} \\ \phi_i^{j+} - \phi_i^{j-} &= \phi_{iref}^{j+} - \phi_{iref}^{j-} \qquad (i,j = 1,2,3), \end{cases} \tag{4.4}$$

where U is the displacement and ϕ is the rotation of the nodes. The subindex "i" represents the direction of the displacement or rotation, and the prime index "j" represents the boundary faces. Equation 4.4 indicates that on opposite boundary faces, the difference of the displacements and rotations of matched nodes should be the same as that of the reference nodes. A similar discussion of periodic boundary conditions can be found in Laroussi et al. (2002).

4.2.4 Computational implementation

We use the Finite Element Analysis package ABAQUS for the computations. In the finite element model, each bar of the substructure (Fig. 4.1) is represented with 8 beam elements B32, which is a 3-node quadratic beam element. The B32 element allows large axial strains

as well as large rotations. It also allows transverse shear strains; that is, the cross-section may not necessarily remain normal to the beam axis. The transverse shear strain is only likely to be of any importance in the thick bars(Timoshenko, 1956) associated with foams of high density.

4.3 Calibration

In this section we discuss the calibration of the model.

4.3.1 Calibration criteria

We calibrate the model by comparing the mechanical response given by the model against the mechanical response measured in experiments (Chapter 3). For each loading case and each density of the foam, we compare the theoretical and experimental stress-strain curves (or force-displacement curves). If the strain energy function given by the model is nonconvex, the function is properly convexified.

The objective of this calibration is to ascertain the capacity of the model to reproduce the most salient features of the mechanical behavior of the series of commercial foams tested in Chapter 4, over the whole range of relative densities of the foams, with emphasis on the the physical mechanism whereby the deformation is effected at large strains. Therefore, it is of particular importance to us that the model should give a nonconvex strain energy function where (and only where) the experiments exhibit a stress plateau and two-phase strain fields. This amounts to a requirement that the model should embody the correct physics associated with a stress plateau and two-phase strain fields—that is to say, the physics of phase transitions.

On the other hand, we place little emphasis on curve fitting in itself, because attaining a perfect fit would require complicating the model in ways which are unrelated to the basic physics of large-strain deformation in EPP foams. Thus, for example, attaining a good fit at small strains would require the use of a nonlinear constitutive relation for the

polyether polyurethane, a complication which would only have second-order effects on the phase transition, which is intrinsically a geometric phenomenon (the snap-through buckling). In a similar way, attaining a good fit at strains beyond the phase transition would require the formulation of an ad-hoc constitute model for the densification of a collapsed microstruture—an interesting project in itself, but beyond our purpose here.

4.3.2 Calibration parameters

We use $\theta = 76^o$, $\gamma = 0.036$, $L_1 = 2.5L$ and $E = 0.85E_m$, where E_m is the Young's modulus of the polyether polyurethane. The cross sectional area A is related to the density of the foam specimen through (4.2), and for each foam the cross sectional area is listed in table 4.1:

Table 4.1: The cross sectional area A for different foams

Specimen Code	EF4003	EF4004	EF4005	TF5070-10	TF5070-13
Relative Density	0.030	0.038	0.046	0.065	0.086
Cross Section Area A	$0.036L^2$	$0.046L^2$	$0.056L^2$	$0.079L^2$	$0.11L^2$

4.3.3 Uniaxial compression along the rise direction

When the foam specimen is subject to uniaxial compression along the rise direction z, the average deformation gradient is

$$\mathbf{F} = \begin{pmatrix} 1 & 0 & 0 \\ 0 & 1 & 0 \\ 0 & 0 & 1+\bar{\Delta} \end{pmatrix}. \tag{4.5}$$

Here $-1 < \bar{\Delta} \leq 0$ is the average axial strain defined as $\bar{\Delta} = \Delta/h_z$, where Δ is the displacement of the loading platen and h_z is the initial height of the specimen along the rise direction. Accordingly, the difference of displacement in z direction between the matching nodes on boundary faces 3+ and 3- (see Fig. 4.2) is $U_3^{3+} - U_3^{3-} = \bar{\Delta} h_z$.

From eq. (4.4), the periodic boundary conditions for this load case is:

1. For matched nodes on face 1+ and 1-,

$$\begin{cases} U_i^{1+} - U_i^{1-} &= 0 \\ \phi_i^{1+} - \phi_i^{1-} &= 0 \qquad (i = 1, 2, 3). \end{cases}$$

2. For matched nodes on face 2+ and 2-,

$$\begin{cases} U_i^{2+} - U_i^{1-} &= 0 \\ \phi_i^{2+} - \phi_i^{2-} &= 0 \qquad (i = 1, 2, 3). \end{cases}$$

3. For matched nodes on face 3+ and 3-,

$$\begin{cases} U_1^{3+} - U_2^{3-} &= 0 \\ U_2^{3+} - U_2^{3-} &= 0 \\ U_3^{3+} - U_3^{3-} &= \bar{\Delta} h_z \\ \phi_i^{3+} - \phi_i^{3-} &= 0 \qquad (i = 1, 2, 3). \end{cases}$$

To preclude a rigid body motion, the three transitional degrees of freedom of one node on the boundary face 3- are restricted. Displacement controlled loading in negative z direction is applied on the nodes on boundary face 3+.

The deformed shape is shown in Fig. 4.3, where one can see snap-through buckling from the front view and side view.

The average stress is calculated as the reaction force on boundary face 3+ divided by the initial area of face 3+ ($A_{3+} = l_x \times l_y$), and the average axial strain is calculated as the displacement of face 3+ divided by the initial height of the representative structure h_z. For the low-density foams ($\rho = 0.030, 0.038, 0.046$), there occurs the up-down-up stress-strain curve associated with the nonconvex strain energy function and the snap-through buckling, just as in the mean-field models for uniaxial compression in Chapter 2. Using the same approach of Chapter 2 (eq. (2.12)), one can calculate the plateau stress for the low-density foams. The up-down-up stress-strain curve does not occur for high density foams ($\rho = 0.065$ and $\rho = 0.086$). In Fig. 4.4, we superpose the normalized (divide the stress by Young's

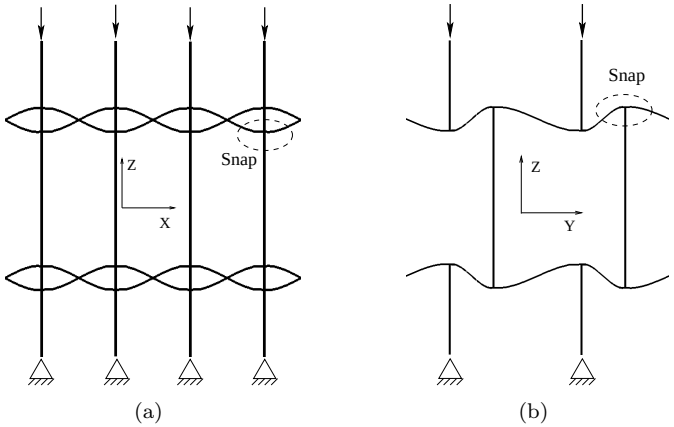

Figure 4.3: The deformed substructure under uniaxial loading along the rise direction (a) Front view. (b) Side view

modulus $E_m = 65\,\mathrm{MPa}$ of the base material) stress-strain curves measured in Chapter 3 to the curves predicted by the model.

From Fig. 4.4, we conclude that the model predicts a stress plateau where and only where a stress plateau was observed in experiments, and the predicted values of the plateau stresses are in remarkable agreement with experiment. Where a stress plateau is predicted, the model also predicts two-phase strain fields, in accord with the DIC measurements of Chapter 3. The predicted stress-strain curves fit the experimental results fairly well up to an average strain of about 14%.

4.3.4 Uniaxial compression along the transverse directions

The responses of our model to the uniaxial loading in both transverse directions are almost indistinguishable, and the EPP foams may be said to be transversely isotropic, in accord with experiments. Here we discuss loading in the y direction.

When the foam specimen is subject to uniaxial compression along the transverse direction (y direction in our model), the average deformation gradient is

$$\mathbf{F} = \begin{pmatrix} 1 & 0 & 0 \\ 0 & 1+\bar{\Delta} & 0 \\ 0 & 0 & 1 \end{pmatrix}. \tag{4.6}$$

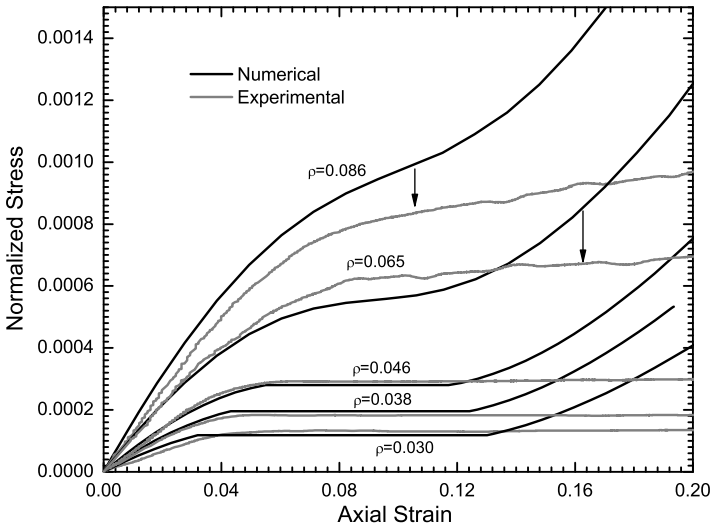

Figure 4.4: The experimental and predicted response of foam specimens for uniaxial compression along the rise direction

Here $-1 < \bar{\Delta} \leq 0$ is the average axial strain defined as $\bar{\Delta} = \Delta / l_y$, where Δ is the compression and l_y is the initial height of the specimen along the rise direction. Accordingly, the difference of displacement in y direction between the matching nodes on boundary faces 2+ and 2- (see Fig. 4.2) is $U_2^{2+} - U_2^{2-} = \bar{\Delta} l_y$.

From eq. (4.4), the periodic boundary conditions for this load case is:

1. For matched nodes on face 1+ and 1-,

$$\begin{cases} U_i^{1+} - U_i^{1-} &= 0 \\ \phi_i^{1+} - \phi_i^{1-} &= 0 \qquad (i = 1, 2, 3). \end{cases}$$

2. For matched nodes on face 2+ and 2-,

$$\begin{cases} U_1^{2+} - U_2^{2-} &= 0 \\ U_2^{2+} - U_2^{2-} &= \bar{\Delta} l_y \\ U_3^{2+} - U_3^{2-} &= 0 \\ \phi_i^{2+} - \phi_i^{2-} &= 0 \qquad (i = 1, 2, 3). \end{cases}$$

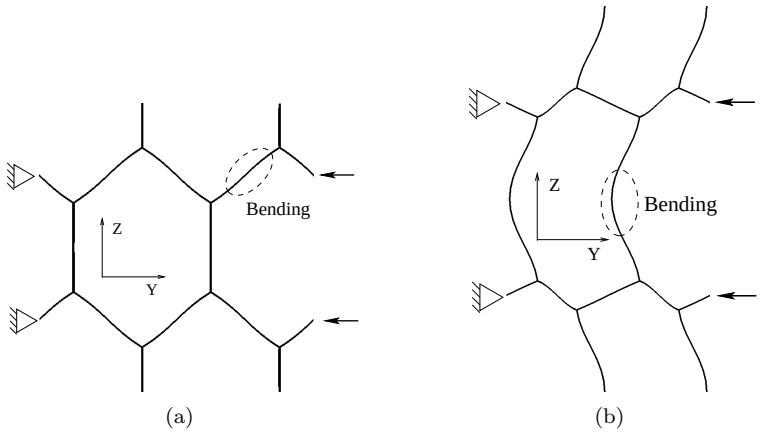

Figure 4.5: The deformed substructure under uniaxial loading along the transverse direction (a) Top view. (b) Side view

3. For matched nodes on face 3+ and 3-,

$$\begin{cases} U_i^{3+} - U_i^{3-} & = 0 \\ \phi_i^{3+} - \phi_i^{3-} & = 0 \qquad (i = 1, 2, 3). \end{cases}$$

To preclude a rigid body motion, the three transitional degrees of freedom of one node on the boundary face 2- are restricted. Displacement controlled loading in negative y direction is applied on the nodes on boundary face 2+.

The deformed shape is shown in Fig. 4.5. Unlike uniaxial compression along the rise direction, there is no snap-through buckling, and the deformation is accounted mostly by bending.

In Fig. 4.6, we superpose the normalized (divide the stress by Young's modulus $E_m = 65MPa$ of the base material) stress-strain curves measured in Chapter 3 to the curves predicted by the model.

From Fig. 4.6, we conclude that the predicted response to uniaxial loading along transverse directions results in no stress plateaus, even for the foam of lowest density, as observed in the experiments. Thus, there is no snap-through buckling, and we have seen that the deformation is accounted mostly by bending. The model also predicts that all strain fields should be homogeneous, consistent with the DIC measurements of Chapter 3. The predicted

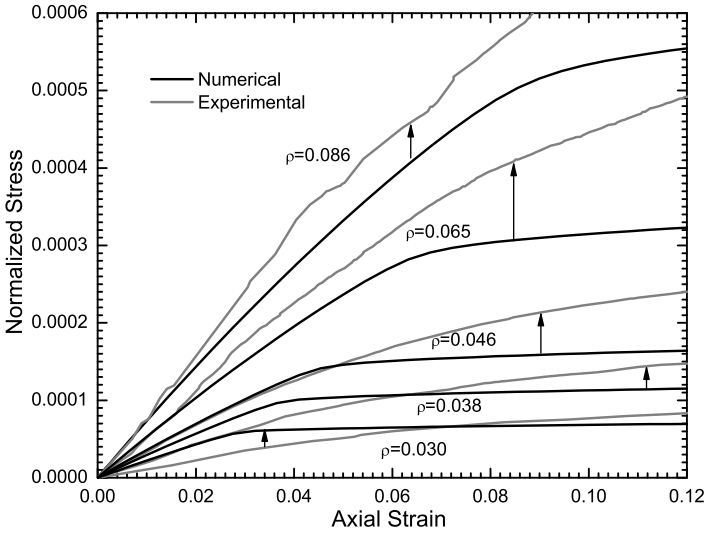

Figure 4.6: The experimental and predicted response of foam specimens for uniaxial compression along one of the transverse direction

stress-strain curves fit the experimental results fairly well up an average strain of about 12%.

4.3.5 Shear combined with compression along the rise direction

When the foam specimen is subject to compression and shear combined loading (the loading case in Chapter 3, Fig. 3.17), the average deformation gradient is

$$\mathbf{F} = \begin{pmatrix} 1 & 0 & 1 + d\sin(\alpha)/l_x \\ 0 & 1 & 0 \\ 1 + d\sin(\alpha)/l_x & 0 & 1 + d\cos(\alpha)/h_z \end{pmatrix}, \tag{4.7}$$

where d is the displacement of the loading platen, and α is the angle of the wedge (Fig. 3.17).

From eq. (4.4), the periodic boundary conditions for this load case are:

1. For matched nodes on face 1+ and 1-,

$$\begin{cases} U_i^{1+} - U_i^{1-} = 0 \\ \phi_i^{1+} - \phi_i^{1-} = 0 \qquad (i = 1, 2, 3). \end{cases}$$

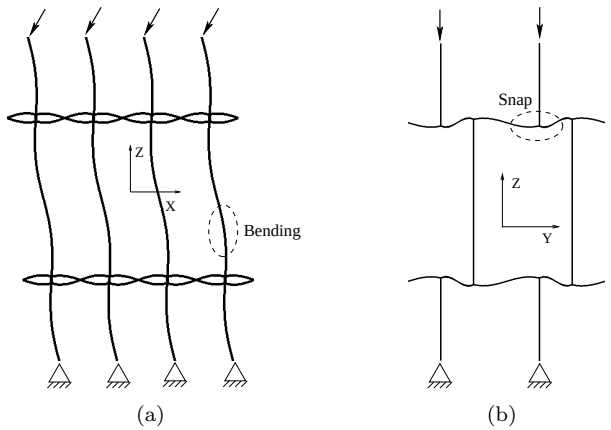

Figure 4.7: The deformed substructure under uniaxial loading along the transverse direction (a) Front view. (b) Side view

2. For matched nodes on face 2+ and 2-,

$$\begin{cases} U_i^{2+} - U_i^{2-} &= 0 \\ \phi_i^{2+} - \phi_i^{2-} &= 0 \qquad (i = 1, 2, 3). \end{cases}$$

3. For matched nodes on face 3+ and 3-,

$$\begin{cases} U_1^{3+} - U_2^{3-} &= d\sin(\alpha) \\ U_2^{3+} - U_2^{3-} &= 0 \\ U_3^{3+} - U_3^{3-} &= d\cos(\alpha) \\ \phi_i^{3+} - \phi_i^{3-} &= 0 \qquad (i = 1, 2, 3). \end{cases}$$

To preclude a rigid body motion, the three transitional degrees of freedom of one node on the boundary face 3- are restricted. Displacement controlled loading in negative x direction and negative z direction is applied on the nodes on boundary face 3+ to simulate the compression and shear combined loading.

The deformed shape is shown in Fig. 4.7, where one can see both snap-through buckling and bending from the front view and side view.

In Fig. 4.8, both calculated loading response and experimental curves are shown. The force-displacement curves predicted by the model fit the experimental curves quite well.

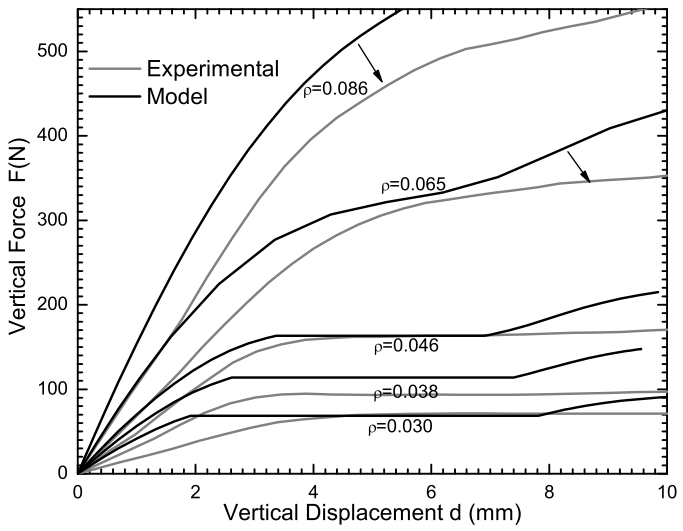

Figure 4.8: The experimental and predicted response of foam specimens for Compression-shear combined loading

4.3.6 Uniaxial tension along the rise direction

For the loading case where the foam specimen is subject to uniaxial tension along the rise direction (z direction in our model), the average deformation gradient is

$$\mathbf{F} = \begin{pmatrix} 1 & 0 & 0 \\ 0 & 1 & 0 \\ 0 & 0 & 1+\bar{\Delta} \end{pmatrix}, \tag{4.8}$$

where $\bar{\Delta} \geq 0$ is the average axial strain. This loading case is very similar to the uniaxial compression along the rise direction, except that the axial strain is positive. Accordingly the boundary conditions are very similar as well, and the only difference is that the nodes on surface 3+ are moved in the positive z direction.

In Fig. 4.9, we superpose the normalized stress-strain curves measured in Chapter 3 to the curves predicted by the model. As expected in the absence of compression, there are no stress plateaus, and the model predicts that all strain fields should be homogeneous. We

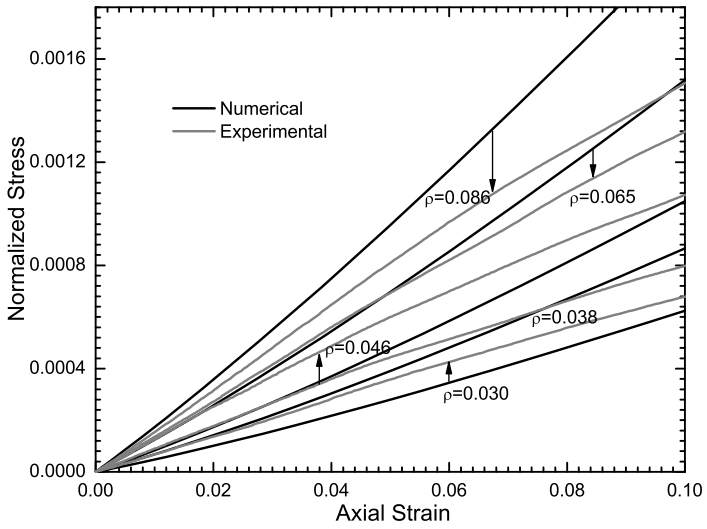

Figure 4.9: The experimental and predicted response for uniaxial tension along the rise direction

interpret the slight softening apparent in the stress-strain curves measured in experiments as signatures of the development of damage in the microstructure of the foams.

4.3.7 Triaxial loading

Similar to experiments, the triaxial loading is modeled as a two-step process. First, confinement hydrostatic pressure is applied. Second, the displacement in x and y directions (transverse directions) of the side surfaces are fixed, while the top surface (surface 3+) is subject to displacement in negative z direction (the compression in the rise direction).

In Fig. 4.10, we compare the measured and predicted axial stress-strain curves. The predicted curves do not fit the experiments as well as the other four loading cases, but the model is able to predict the most notable trends, such as the occurrence of the stress plateaus, and the drop of the plateau stress with the increase of confinement pressure.

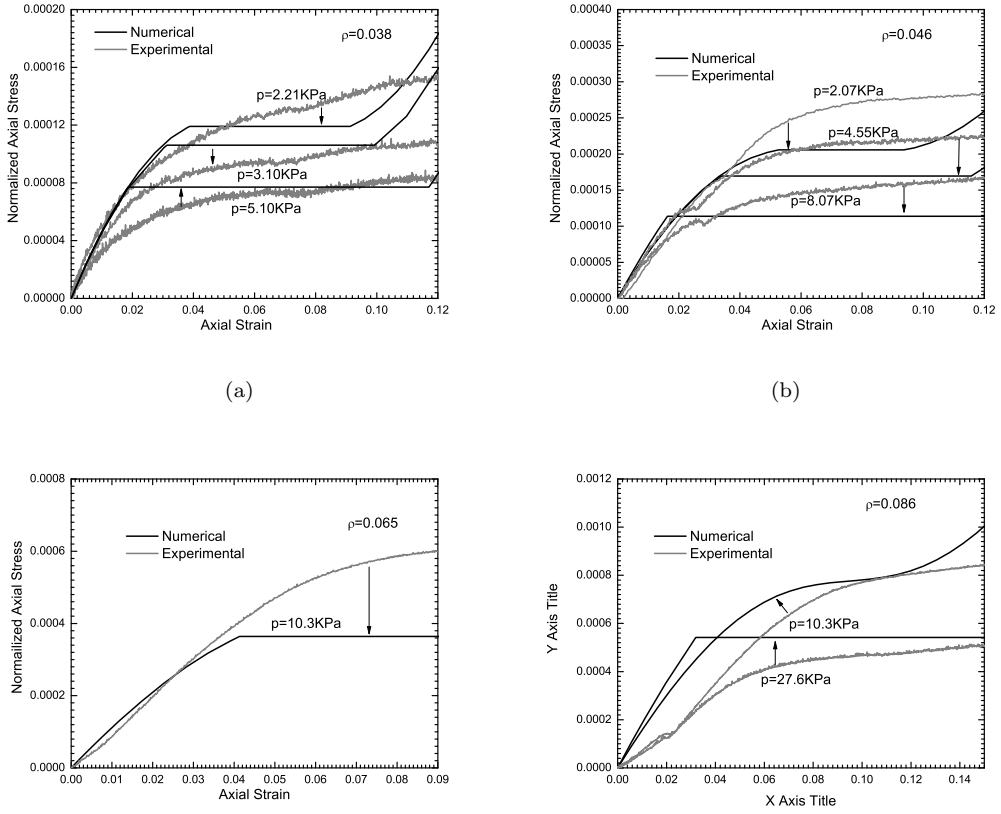

Figure 4.10: The normalized axial stress vs axial strain curves for the triaxial loading case (a) For specimen with relative density $\rho = 0.038$. (b) For specimen with relative density $\rho = 0.046$. (c) For specimen with relative density $\rho = 0.065$. (ed) For specimen with relative density $\rho = 0.086$.

4.4 Discussion

The mechanical behavior of EPP foams under uniaxial stretch exhibits stress plateaus and heterogeneous, two-phase strain fields for low-density foams; a critical point for foams of critical density; and hardening accompanied by homogeneous strain fields for high-density foams. Thus, even under the simplest loading, a vast phenomenological universe accompanies the deformation of EPP foams up to large strains. And yet, as we have shown in Chapter 2, all of the most salient features of this vast phenomenological universe can be described using a simple mean-field model. In this simple mean-field model, an idealized cell of the microstructure of the foam is subjected to displacements affine to the applied mean strain and used to compute a strain energy function. For low-density foams, where the bars that constitute the idealized cell are relatively slender, the cell attains a limit point and undergoes snap-through buckling; as a result, the strain energy function is nonconvex. The nonconvex strain energy function can be convexified using conventional tools of analysis, and the results confer a straightforward theoretical interpretation to the most salient structural features of the mechanical response of EEP foams subjected to uniaxial loading: the stress plateaus, the two-phase strain fields, the critical point, etc. Further, the mean-field model yields theoretical stress-strain curves which fit well the stress-strain curves measured in experiment for a complete series of commercially available EPP foams subjected to uniaxial stretching. In particular, the predicted values of the plateau stresses for foams of different densities are in very good accord with the values measured in experiments.

In this chapter, we have extended the work of Chapter 2 to show that a 3D generalization of the mean-field model of Chapter 2 can account in a similar way for the experimental results Chapter 3, where the mechanical response of EPP foams was measured for five different loading cases. These loading cases are uniaxial compression along the rise direction, uniaxial compression along the transverse directions, compression-shear combined with uniaxial tension along the rise direction, and triaxial loading.

Each of the few geometrical or material parameters of the 3D mean-field model has a

clear physical meaning related to the microstructure of a foam. Using a single set of values of these parameters, we have verified that for all five loading cases and each of the foams in a commercially available series of EPP foams, the model gives a nonconvex strain energy function where (and only where) the experiments exhibit a stress plateau and heterogeneous, two-phase strain fields. These results lend a straightforward theoretical interpretation to the most salient structural features of the mechanical response observed experimentally in EEP foams of a wide range of densities, and for a variety of multiaxial loading cases.

By means of a comparison of the predicted and measured plateau stresses (the sole criterion by which models have been evaluated in the past, invariably for a few foams of similar densities subjected to uniaxial loading), we have shown that the 3D mean-field model gives remarkably accurate predictions of all plateau stresses with the exception of the plateau stresses of the triaxial loading case, where the predicted plateau stresses are off by up to 30% for some foams. Even though we have not made a particular effort at curve fitting (cf. Section 4.3.1), we have seen from an unprecedented comparison of the complete, predicted and measured stress-strain curves for each loading case and each foam, that the model gives a remarkably good fit for most loading cases. The only exception is once more the triaxial loading case, where the fits can be said to be reasonable.

We close this chapter with a few remarks on the evaluation of the goodness of a model of EPP foams. To the best of our knowledge, we are the first to have compared measured and predicted stress-strain curves for numerous loading cases and a complete series of foams of widely differing densities. This practice must become common place if we are to provide a reliable simulation tool for engineering applications. In this respect, our 3D model would benefit from further work aimed, for example, at attaining a better fit at small strains through the introduction of a suitable nonlinear constitutive relation for the polyether polyurethane.

We would like to emphasize, however, that the goodness of a model can hardly consist in the capacity of the model to give excellent fits to numerous stress-strain curves measured in experiments. Instead, the most important criterion of goodness is that a model should embody the correct physics associated with the most salient features of the mechanical

response observed in experiments. For EEP foams, these most salient features are the stress plateaus and the attendant two-phase strain fields.

In this respect, note that a stress plateau can be modeled using continuum plasticity. This has been a common practice in the automotive industry, where continuum plasticity models of EPP foams are customarily used to perform computational simulations of seat–passenger interactions that take place during a crash. And yet, in continuum plasticity a stress plateau is not accompanied by two-phase strain fields.

A stress plateau can also ensue from Euler buckling, and in most models of EPP foams the stress plateaus are associated with a bifurcation of equilibrium of the microstructure of the foam. Where the microstructure of a foam undergoes Euler buckling, the attendant strain field will correspond to an eigenfunction of arbitrary amplitude. As the applied mean strain is increased following buckling, the stress-strain curve traces a stress plateau, and the strain field remains invariant except for the amplitude, which increases to accommodate the applied mean strain. This scenario is inconsistent with the conjunction of a stress plateau and two-phase fields observed in experiments, where an increasing applied mean strain is accommodated by growth of the volume fraction of the high-density phase at the expense of the volume fraction of the low-density phase.

The leitmotif of this chapter has been a focus on the most distinctive structural feature of the mechanical response of EPP foams evinced in experiments: the conjunction of a stress plateau and two-phase fields. This conjunction signals the prevalence of a phase transition, which is the basic physics of large-strain deformation in EPP foams. Thus, in judging the performance of our model, we have emphasized the capacity of the model to give a nonconvex strain energy function—the signature of a phase transition—where (and only where) the experiments exhibit a stress plateau and two-phase strain fields. This emphasis should remain a guiding methodological trait in the design of constitutive models of EPP foams.

Chapter 5

Punching elastic foams in the self-similar regime

5.1 Introduction

Polyether polyurethane foams are used in packaging, for example, to protect merchandize in shipping, transportation, and handling. Polyether polyurethane foams are also used in car seats to provide comfort and safety to car occupants. In these applications and many similar ones, the purpose of the foam is to react to outside forces that impinge on the foam. For example, when a car occupant is seated in a car, his legs, back, and buttocks impinge on the foam of the seat. In this example, the occupant's legs and back may be thought of as cylindrical punches, and the buttocks as spherical punches. Thus, it is of interest to determine what happens when a punch penetrates an elastic foam, and how the foam reacts mechanically.

Here we investigate experimentally the mechanical behavior of polyether polyurethane foams being penetrated by a rigid punch (i.e., a punch made of a material that is much stiffer than the foams). We use two types of punches of simple geometry: a wedge-shaped punch and a conical punch. We also perform a theoretical analysis of the experiments and show the predictions to be in good agreement with the experimental measurements.

5.2 Experimental set-up

The experimental set-up consists of an ATS testing machine (Fig. 3.1) that is used to drive the punch into the foam specimen at a constant velocity. During an experiment, the punch is attached to a load cell whose signal is fed to a computer running the LabView software. This

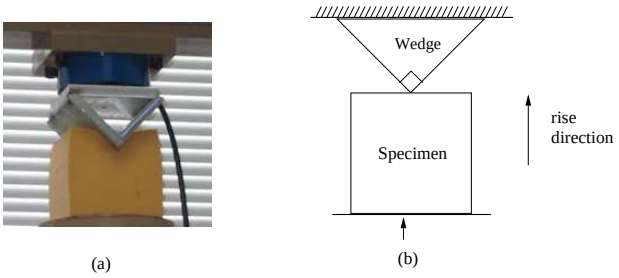

Figure 5.1: Experimental setup for wedge-punching

software computes the force (by multiplying the signal from the load cell by a calibration constant) and the penetration of the punch (by multiplying the signal from a transducer, which is attached to the ATS machine to measure the displacement, by a calibration constant. The load cell and transducer are carefully calibrated to ensure accuracy). After performing these computations, the software displays the force vs. the penetration in graphical form on the screen of the computer in real time. To obtain photographs of the specimen being penetrated by the punch during the experiment, we use a high-resolution digital camera attached to a frame grabber mounted on the same computer.

In our experiments we use cubic specimens of side 10 cm. The specimens are made of polyether polyurethane foams of five different apparent densities: $50.3, 63.0, 77.0, 162.9$ and $220.5\,\mathrm{kg/m^3}$. The relative densities are $\rho = 0.030, 0.038, 0.046, 0.065$, and 0.086. (These foams are known to the manufacturer, General Plastics of Tacoma, WA, by the codes $EF-4003, EF-4004, EF-4005, TF5070-10$ and $TF5070-13$, respectively). In all cases we align the (vertical) axis of the punch with the rise direction of the foam. Note on the rise direction: Polymeric foams are manufactured by promoting the growth of numerous gas bubbles within a solid or liquid layer of polymer. As a result of the growth on these bubbles, the layer expands anisotropically, mostly along the direction normal to the midplane of the layer. This direction is the rise direction. The rise direction of the foam is an axis of transverse anisotropy.

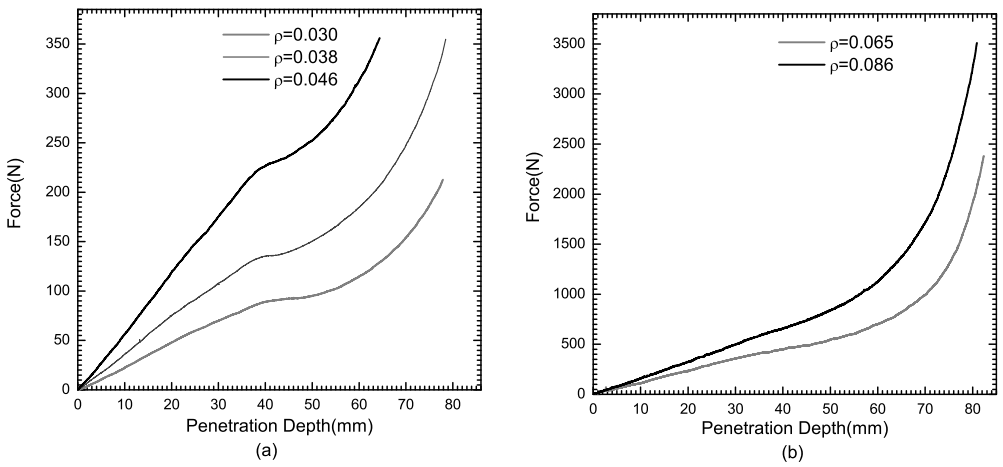

Figure 5.2: Plots of the force vs. the penetration displacement measured in five experiments with the wedge-shaped punch. (a) The three experiments correspond to foams of low densities ($EF-4003, EF-4004, EF-4005$). (b) The two experiments correspond to foams of high densities ($TF5070-10$ and $TF5070-13$). For comparison, the height of the specimen is 10 cm.

5.3 Wedge punching test

Figure 5.1 shows a picture of the wedge-shaped punch penetrating the foam specimen in one of these experiments. The punch is made of aluminum plates, and the wedge angle is 90 °. In the picture, the tip of the punch has penetrated through about 25% of the height of the specimen (or 2.5 cm). It is apparent that large strains and rotations must develop in the foam during these experiments, especially in a vicinity of the tip of the punch.

Figure 5.2 shows plots of the force vs. the penetration for the five foams tested with the wedge-shaped punch. The curves for lower density foams are shown in Fig. 5.2a and those of higher density foams are shown in Fig. 5.2b. It is seen from these plots that the larger the density of the foam, the larger the punching force for any given penetration. The plots of Fig. 5.2a reveal a striking feature of the mechanical response of the low density foams: the force varies linearly with the penetration up to a penetration of about 40% of the height of the specimen; then, there is a sudden change, and the mechanical response becomes nonlinear. But in Fig. 5.2b, for high density foams, there is no such a sudden change, and the slope of each curve increases smoothly. Because of the constitutive nonlinearities and the large strains and rotations that develop during the experiment, the observed linear mechanical

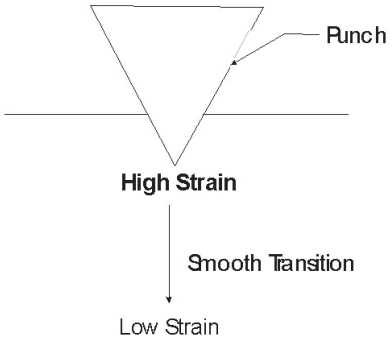

Figure 5.3: Schematic of a strain field with a smooth transition from a high strain close to the tip of the punch to a low strain far from the tip.

response over a broad range of penetrations would seem unimaginable. How to explain it? To answer this question, in the following section we turn to a theoretical analysis of the experiments.

5.4 The self-similar regime

5.4.1 Strain fields and the mechanical behavior of foam cells

Consider once more the picture of Fig. 5.1, which shows the wedge-shaped punch penetrating a foam specimen. Close to the tip of the punch, the strain in the foam is high; far from the tip, it is low. Now we might expect a smooth transition from the high strain that prevails close to the tip to the low strain that prevails far from the tip. Figure 5.3 illustrates this expectation schematically.

Implicit in the expectation illustrated in Fig. 5.3 is the assumption that the foam may be locally subjected to any value of strain. Yet this is not the case. In fact, polyether polyurethane foams (at least foams of low apparent density) have preferred values of strain (Gioia et al., 2001). These foams may be locally subjected to a low value of strain or a high value of strain, but not to intermediate values of strain. The reason for this behavior must be found in the microstructure of the foams. A polyether polyurethane foam consists of a more or less regular array of cells, where each cell consists of a number of slender bars of similar length and cross section (Fig. 5.4a and b). Figure. 5.4c shows an idealized version of

this array of identical cells. Now the cells of a foam subjected to a compressive strain act structurally as slender, shallow arches. When a load is applied to a slender, shallow arch, the deformation of the arch increases smoothly as the load is increased, but only up to a certain limit load. Then, if the load is increased beyond the limit load, the deformation of the arch jumps discontinuously to a much higher level. This mechanical phenomenon, called "snap-through buckling" by structural engineers, implies that foams have two preferred values of strain: a low value of strain associated with the configuration of the cells before snap-through buckling (Fig. 5.4c) and a large value of strain associated with the configuration of the cells after snap-through buckling (Fig. 5.4d). Because they undergo snap-through buckling when compressed, the cells of foams may be termed bi-stable elastic structures. (For a pioneering study of the snap-through bulking in foams, see Lakes et al. (1993)). Even though we may be unaware of it, bi-stable elastic structures are frequently encountered in everyday life. For example, the cap of a shampoo bottle is a bi-stable elastic structure: the cap is always either closed (as in Fig. 5.4e, which should be compared with Fig. 5.4c) or open (as in Fig. 5.4f, which should be compared with Fig. 5.4d), but not partially open or partially closed.

5.4.2 The self-similar regime

Let us now discuss how the sharp interface evolves during an experiment with a wedge-shaped punch. For simplicity, we assume that the sharp interface is a semi-cylinder of radius R, as shown in Fig. 5.5(a). As the penetration increases, we expect that R should increase too (Fig. 5.5(b)). Since there is no characteristic length in the wedge-shaped punch, the only prevailing length scale is the penetration d. Thus the radius R of the sharp interface must be proportional to the penetration d of the punch, as illustrated in Fig. 5.5. As the penetration increases during the test, the radius of the sharp interface increases in direct proportion to the penetration. This we call the self-similar regime, because in this regime the sharp interface remains similar to itself (it is always a semi-cylinder). The self-similar regime prevails until the sharp interface reaches the side or bottom of the specimen. After the sharp interface has reached the side or bottom of the specimen, a new length scale,

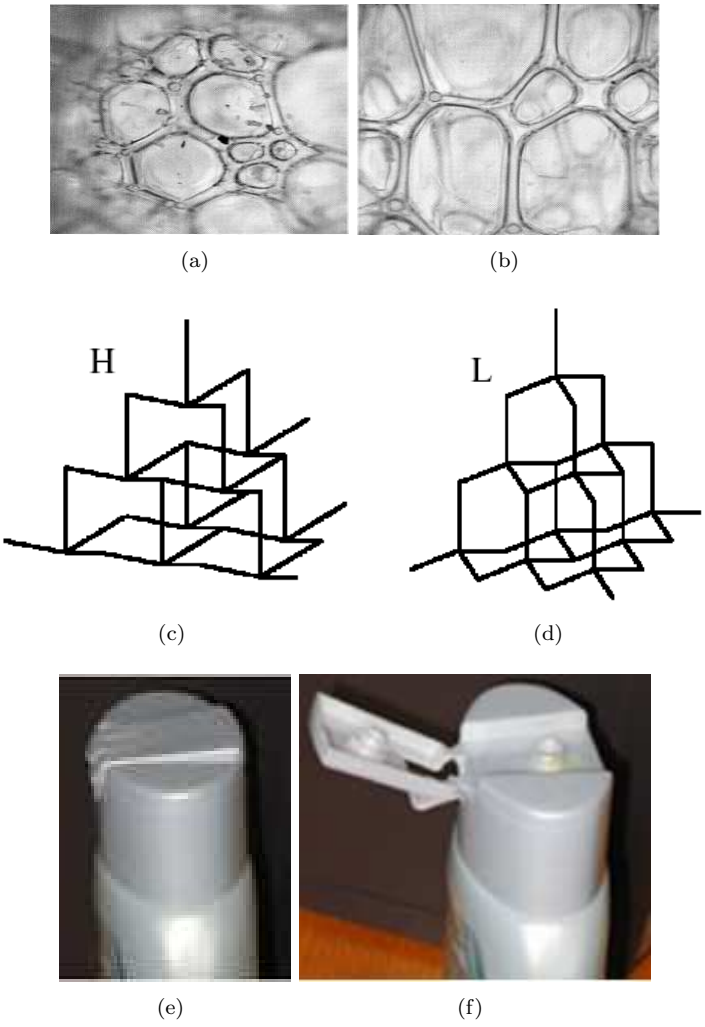

Figure 5.4: Microphotographs of an array of cells in a polyether polyurethane foam and the cap of a shampoo bottle. The cap and a foam cell are examples of bi-stable elastic structures. (a) Plane perpendicular to the rise direction. (b) Plane parallel to the rise direction. (c) An Idealized array of cells. (d) The array of cells after snap-through buckling. (e) Closed cap. (f) Open cap.

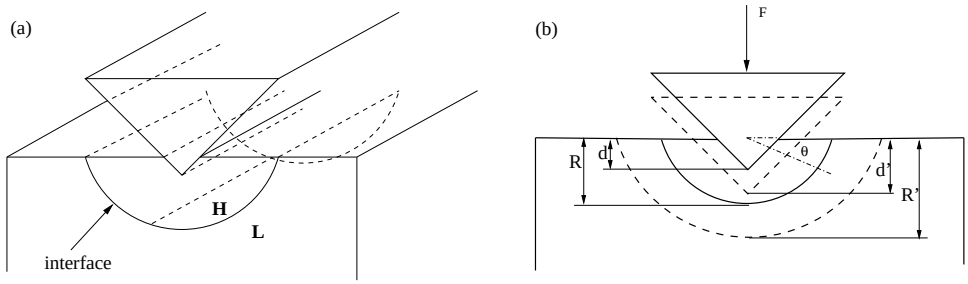

Figure 5.5: Schematic strain field with a sharp transition. (a) 3-D view. (b) Front view. As the penetration increases, the radius of the sharp interface increases proportionally.

provided by the height of the specimen, comes into play. Then, the sharp interface need not (and will not) continue to be a semi-cylinder, the self-similar regime comes to an end, and the mechanical response may undergo a sudden change. We recall that Fig. 5.2a did display a sudden change in mechanical response for a penetration of about 40% of the height of the specimen; we may now ascribe the observed change in mechanical response to the end of the self-similar regime. We may also estimate the higher preferred strain to be close to 0.4.

We now turn to a discussion of how the punching force varies within the self-similar regime. We seek to establish that within the self-similar regime the punching force is proportional to the surface area of the sharp interface. Even though it is possible to prove this rigorously, here we offer only a highly simplified and intuitive plausibility argument, as follows. Consider a point on the sharp interface at any time within the self-similar regime. There is a foam cell on one side of the interface and a foam cell on the other side. One of these cells has already undergone snap-through buckling, whereas the other has not. Because the cells must be in equilibrium with one another, they must both be subjected to a same stress, which we may call the interface stress. Now if both cells are subjected to the same interface stress, but one cell has buckled and the other one has not, then it must be that the interface stress is the buckling stress, which corresponds to the limit load at which the cells undergo snap-through buckling. Given that the limit load is strictly a property of the cells, and therefore the buckling stress strictly a property of the foam, it follows that the interface stress cannot depend on the radius of the sharp interface. Thus we conclude that the interface stress at any point on the sharp interface is independent of the radius of the sharp interface within the self-similar regime.

Consider now the punching force. The punching force can be obtained as an integral of the interface stress over the entire surface of the sharp interface. Because the interface stress does not depend on the radius of the sharp interface, this integral, and therefore the punching force, must be proportional to the surface area of the sharp interface. In conclusion, we have showed that within the self-similar regime the punching force is proportional to the surface area of the sharp interface. In the next paragraph, we apply this result to the special case

of a wedge-shaped punch.

In the case of a wedge-shaped punch in the self-similar regime, the sharp interface is a semi-cylinder, whose surface area is proportional to the radius R. Since R is in turn proportional to the penetration, it follows that the punching force is proportional to the penetration (in the self-similar regime). This is precisely the mechanical response observed experimentally (Fig. 5.2).

5.4.3 Observation of the sharp interface via global DIC

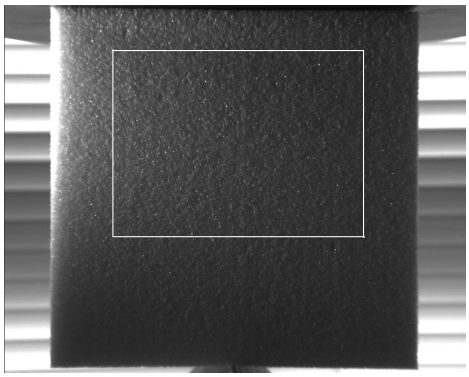

Figure 5.6: DIC frame for wedge punching on a low density ($\rho = 0.038$) cubic specimen

The interface is also observed experimentally. As shown in Fig. 5.6, we fix the wedge on the lower loading plate of the ATS loading machine (Fig. 3.1). We then attach the low-density cubic specimen EF-4004 with dimensions $10\,\text{cm} \times 10\,\text{cm} \times 10\,\text{cm}$ and relative density $\rho = 0.038$ to the upper plate of the ATS loading machine. As the lower plate is driven up at a constant speed by the ATS loading machine, the wedge punches the foam specimen. (Note here the loading setup is a little different than that of section 5.1 for the purpose of taking digital images for DIC.) During the loading process, we take 40 digital images of one lateral face of the specimen at equal intervals of loading path, and use global DIC to correlate the successive images, one pair at a time, to compute the displacement field.

The displacement field of a rectangular region of $6.8\,\text{cm} \times 5.2\,\text{cm}$, which is the region inside the white rectangle in Fig. 5.6, is calculated, and the contour plots of vertical displacement at different values of the penetration depth are shown in Fig. 5.7. In these plots, x_0 and y_0 are

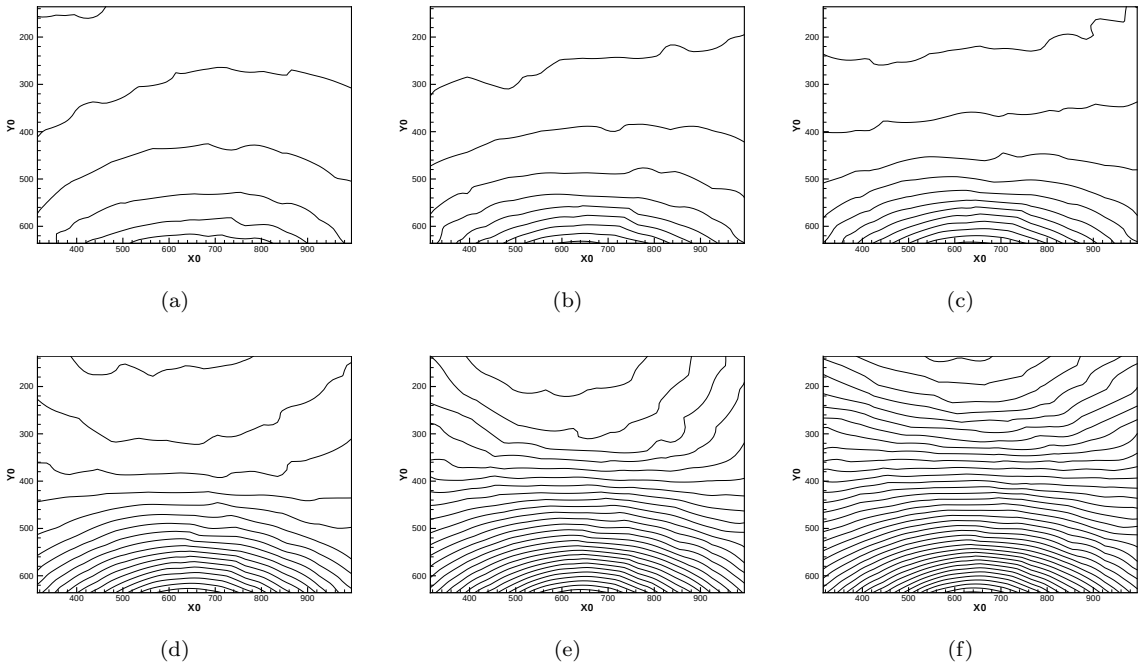

(a) (b) (c)

(d) (e) (f)

Figure 5.7: Contours of displacement along the rise direction for the foam of lower density

the horizontal and vertical (rise direction and also the direction of loading) coordinates of the image of the undeformed specimen face (Lagrangian coordinates), and 1 pixel is according to 0.1 mm. In these plots, the lines are contours of equal displacements with increment of 0.5 mm.

In the figure, (a)-(e) are contours when penetration depth is 2.5, 2.9, 3.1, 3.6, 4.3 and 5.0 cm respectively. We can clearly see two regions of different displacements gradients, and an evolving interface separating the two regions. The shape of the interface remains unchanged during the punching process.

5.4.4 The self-similar regime and the plateau stress

For low density foams, buckling induced configurational phase transitions may occur under certain loading conditions. During uniaxial compression, the buckling happens at defects where the micro structure is weaker. Buckling may happen at different locations and then the high local strain (buckled) phase forms and develops, and hence results in a stratified deformation field (Gioia et al., 2001). But during the wedge punching, the stress is larger in

the region closer to the wedge punch, so the high strain (buckled) phase forms at the punch tip, and grows into the specimen when the punching continues. There should be a sharp interface during the process to separate the two phases (Fig. 5.5a).

The wedge punching process can be simplified to a 2-D problem, since the interface is a part of some kind of cylinder (not necessarily with a circular cross section), and can be represented by a curve (Fig. 5.5b) of function $r(\theta) = R\Theta(\theta)$, where r and θ are polar coordinates and R represents the length scale of the curve, while the dimensionless function $\Theta(\theta)$ gives the shape of the curve. Since during the punching process, the only prevailing length scale is the penetration depth d, R must increase proportionally to d. In Fig. 5.5b, as the penetration increases from d to d', the curve that represents the interface becomes $r'(\theta) = R'\Theta(\theta)$, and $R/d = R'/d' = c_1$, where c_1 is a constant. Note here we have assumed the self-similar evolvement of the interface. (The spatial self-similarity of contact for isotropic linear elastic materials was established by (Galanov, 1981) and (Borodich, 1983), for non-linear power-law materials, it was discovered by (Galanov, 1981) and (Borodich, 1989) in isotropic and anisotropic cases respectively.)

We know that in the uniaxial case the configurational phase transition occurs when the condition $\sigma = \sigma_p$ is satisfied. We can assume a similar buckling condition for multiaxial cases, $f(\sigma_1, \sigma_2, \sigma_3) = \sigma_y$, where σ_y is a material constant, σ_1, σ_2, and σ_3 are principal stresses, and $f(\sigma_1, \sigma_2, \sigma_3)$ is a homogeneous function of order one on the magnitude of the stress tensor $|\boldsymbol{\sigma}|$, i.e., $f(n\sigma_1, n\sigma_2, n\sigma_3) = nf(\sigma_1, \sigma_2, \sigma_3)$, where n is a constant scalar. Due to self similarity, at points (r, θ) and (r', θ) on the two interfaces shown in Fig. 5.5, the stress tensors should be different only by a scalar factor, or $\boldsymbol{\sigma}(r, \theta) = \lambda\boldsymbol{\sigma}(r', \theta)$, where λ is a scalar. So $\sigma_i(r, \theta) = \lambda\sigma_i(r', \theta)$, where i=1, 2, 3. Thus we have the phase transition criterion:

$$f(\sigma_1, \sigma_2, \sigma_3)|_{r',\theta} = f(\lambda\sigma_1, \lambda\sigma_2, \lambda\sigma_3)|_{r,\theta} = \lambda f(\sigma_1, \sigma_2, \sigma_3)|_{r,\theta} = \\ = f(\sigma_1, \sigma_2, \sigma_3)|_{r,\theta} = \sigma_y. \tag{5.1}$$

From eq. (5.1), we can tell $\lambda = 1$, i.e. on the interfaces, $\boldsymbol{\sigma}(r, \theta) = \boldsymbol{\sigma}(r', \theta) = \boldsymbol{\sigma}(\theta)$. So

the stress on the interface is independent of the length scale of the interface R. The loading force equals the integration of the vertical components of the stress over the interface and should be proportional to the area of the interface. For this cylindrical surface, the area is proportional to the length scale R. So the force should be proportional to the penetration depth d. We can calculate the loading force F when the penetration depth is d,

$$F(d) = \int_0^{\pi} (\sigma_{rr}(\theta) \sin\theta + \sigma_{r\theta}(\theta) \cos\theta) R\Theta(\theta) d\theta, \tag{5.2}$$

where $\sigma_{rr}(\theta)$ and $\sigma_{r\theta}(\theta)$ are normal and shear components of $\boldsymbol{\sigma}(\theta)$, and are all functions of θ. We know R stands for the length scale of the curve, which is proportional to the penetration depth d, $R = c_1 d$, so the eq. (5.2) can be written as,

$$F(d) = Cd, \qquad (C \equiv c_1 \int_0^{\pi} (\sigma_{rr}(\theta) \sin\theta + \sigma_{r\theta}(\theta) \cos\theta)\Theta(\theta) d\theta). \tag{5.3}$$

Equation 5.3 clearly shows that the loading force is proportional to the penetration depth when there is an interface, as shown in Fig. 5.2a and Fig. 5.9a.

The coefficient C in eq. (5.3) is related to the material constant σ_y, since $\sigma_{rr}(\theta)$ and $\sigma_{r\theta}(\theta)$ in the integral must be related to σ_y. It is very likely that σ_y is proportional to the plateau stress σ_p during uniaxial compression.

5.4.5 Predictions for the self-similar regime

With the self-similar regime discussed above, we can make several predictions:

1) For low density foams under punching, the loading force F is proportional to penetration depth d: $F = Cd$, and the coefficient C should be proportional to the plateau stress for uniaxial compression. If the loading force is normalized by the plateaus stress, the normalized force-deflection curves of low density foams should collapse to one.

To verify this prediction, we can normalize the force deflections curves of the wedge punching tests. As discussed before, for low density foams, there is a stress plateau on the stress-stretch curve when compressed along the rise direction. We define Maxwell force

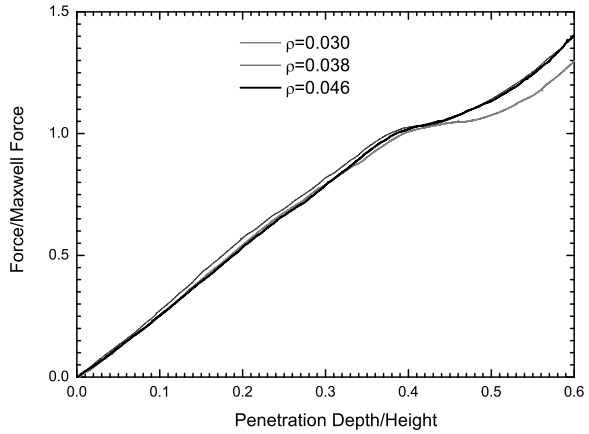

Figure 5.8: The normalized force-penetration depth curves for low density cubic foam specimens

$f_m = \sigma_p \times S$, where s is the cross section area of the specimen, and σ_p is the plateau stress during uniaixal compression. We measure the Maxwell force for low density specimens in uniaxial experiments, and the values are 88.4 N, 131.8 N and 222.6 N for foams of relative density $\rho = 0.030, 0.038$, and 0.046 respectively. We can use the Maxwell force to normalize the loading force, and the specimen height to normalize the penetration depth. Figure 5.8 gives the normalized force-penetration depth curves. In the figure, we can see the linear parts of the three curves are very close to each other.

2) We can also explain the change of slope of the force vs. penetration depth curves (Fig. 5.2a) with the propagation of the interface. For the cubic specimens, at certain point, the interface touches the left and right sides of the specimen and the interface shape will change, so eq. (5.3) is not valid any more. Since the left and right sides are free, there will be some kind of stress release. That is why the slope suddenly drops at the kink (Fig. 5.2a). For high density foams, there is no such propagating interface and hence no sudden change of slope (Fig. 5.2b). When we punch the shorter specimens, the interface may touch the bottom first. Since the bottom is constrained by the loading platen, the slope should have a sudden increase.

To verify this prediction, we carry punching experiments on low density specimens of a different geometry: a cross-section of 10 cm × 10 cm and a height of 5.0 cm (rise direction).

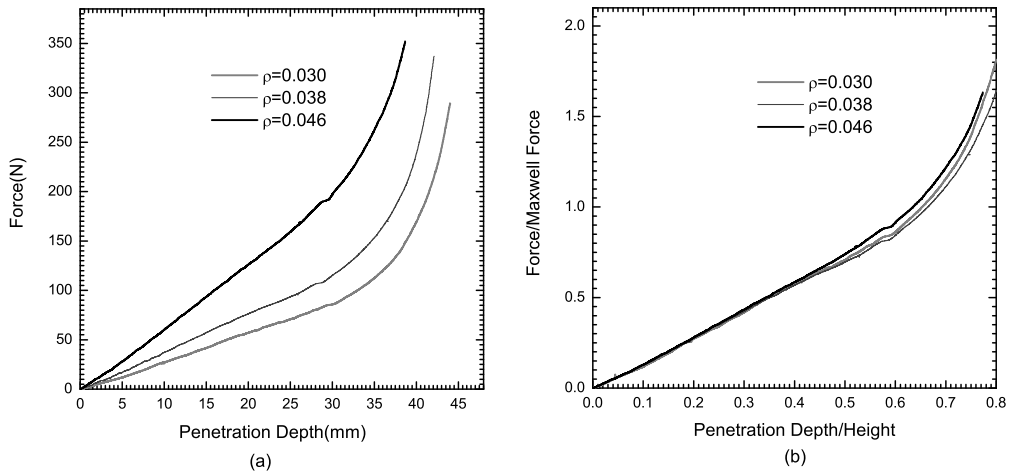

Figure 5.9: The curves of loading force vs. the penetration depth for wedge punching on low density foam specimens with a geometry of a cross section 10 cm × 10 cm and a height of 5.0 cm. (a) Force vs. indentation depth curves. (b) Normalized curves

The Maxwell force are measured in uniaxial compression tests to be 101.8, 131.8 and 215.5 N respectively. The curves of loading force vs. penetration depth are shown in Fig. 5.9a and corresponding normalized curves are shown in Fig. 5.9b.

In Fig. 5.9, we can clearly see the kinks occurring at the penetration depth of about 28 mm. But unlike in cubic specimens, here at the kink the slopes have a sudden increase, exactly as predicted. In Fig. 5.9b, the linear parts of the normalized curves almost collapse to one.

3)In wedge punching, the interface is a part of a cylinder and can be represented by a 2-D curve. But for the conical punching, the interface is an axisymmetric surface, and the punching can not be simplified as a 2-D problem.

The 3-D interface can be represented by a function $r(\theta, \phi) = R\Theta(\theta, \phi)$, where r, θ and ϕ are the spherical coordinates (Fig. 5.10), and R is the length scale of this interface (Fig. 5.10) while the dimensionless function $\Theta(\theta, \phi)$ gives the shape of the interface. The length scale R is proportional to the penetration depth d, $R = c_1 d$, where c_1 is a constant. Similar to previous analysis, the stress tensor on the interface $\boldsymbol{\sigma}(\theta, \phi)$ does not depend on the length scale of the interface R. The loading force is proportional to the area of the interface while the interface is axisymmetric and has a quadratic relationship with the length scale R. So

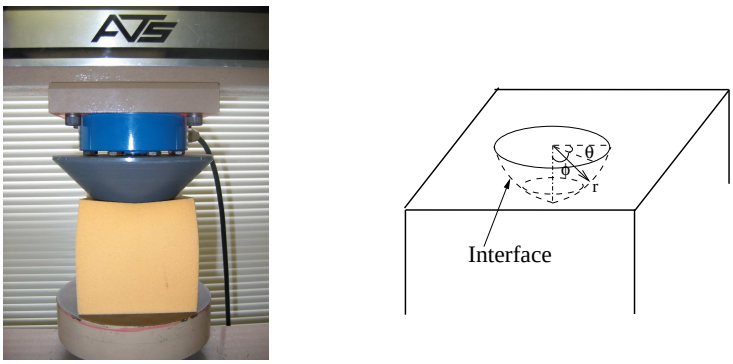

(a) (b)

Figure 5.10: (a) Conical punching experimental setting. (b) Sketch of the 3-D interface

we can expect the loading force has a quadratic relationship with the penetration depth d. We can get the relationship between the loading force and the penetration depth

$$f(d) = Cd^2, \qquad (C = \int_0^{\pi} \int_0^{2\pi} \boldsymbol{\sigma}(\theta, \phi)\boldsymbol{n} \cdot \boldsymbol{e_3}\Theta(\theta, \phi)d\theta d\phi). \tag{5.4}$$

In eq. (5.4), $\boldsymbol{n}$ is the normal of the surface and $\boldsymbol{e_3}$ is the vertical direction. This equation predicts that the loading force is quadratic with penetration depth.

To verify this prediction, we carry punching tests with cone shaped punch, and details are given in the following section.

5.5 Conical punching test

Using the same experimental setup with a cone punch of right angle, we performed conical punching tests on low density foams ($\rho = 0.030, 0.038$, and 0.046). Both cubic specimens and shorter specimens are tested. Fig. 5.10 gives the cone punching picture and the sketch of the 3-D interface.

For the cubic specimens, the curves of loading force vs. penetration depth are shown in Fig. 5.11a; corresponding normalized curves are shown in Fig. 5.11b (using the Maxwell forces 88.4 N, 131.8 N and 222.6 N for specimens of density $\rho = 0.030, 0.038$, and 0.046 respectively).

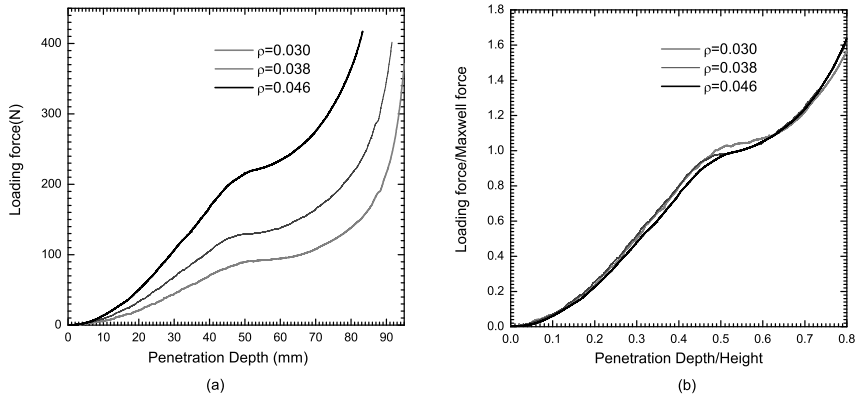

Figure 5.11: Conical punching on cubic specimens. (a) Loading force vs. penetration depth curves. (b) Corresponding normalized curves

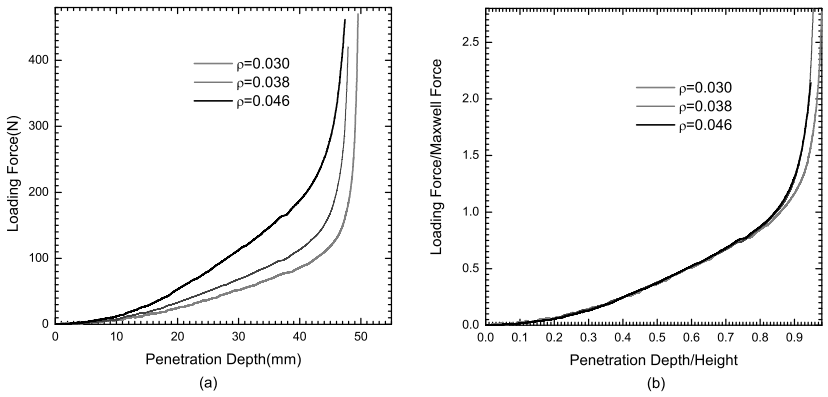

Figure 5.12: Conical punching on shorter specimens. (a) Loading force vs. penetration depth curves. (b) Corresponding normalized curves

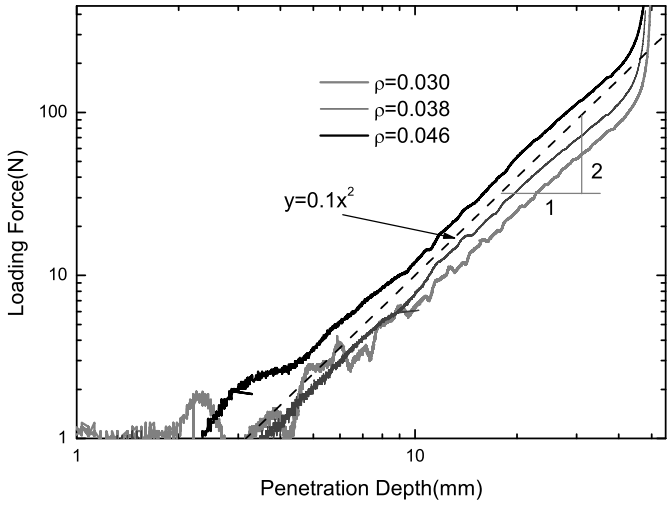

Figure 5.13: Loading force vs. penetration depth curve in log-log space for conical punching on short specimens

Unlike wedge punching, there is no linear part in the curves, but there are still kinks. The slope drop at the kinks shows the interface touches the free surface on the side. The normalized curves are very close to each other, consistent with the first prediction.

For the shorter specimens (cross section 10 cm × 10 cm, height 5 cm), the curves of loading force vs. penetration depth are shown in Fig. 5.12a; corresponding normalized curves are shown in Fig. 5.12b (using the Maxwell forces 101.8 N, 131.8 N and 215.5 N for specimens of density $\rho = 0.030$, 0.038 and 0.046 respectively). We can see kinks in Fig. 5.11. The sudden slope jump at the kinks shows that the interface touches the bottom, consistent with prediction 1. The normalized curves almost collapse to one curve, consistent with prediction 2.

The initial parts in Fig. 5.11 and Fig. 5.12 look like parabola, in accord with eq. (5.4). To be more accurate, we draw Fig. 5.12a in the log-log space. Fig. 5.13 clearly shows the quadratic relationship between the loading force and penetration depth, exactly as eq. (5.4) predicts.

5.6 Discussion

The surprising mechanical response observed in experiments with wedge-shaped and conical punches may be traced to the behavior of the basic microstructural components of a polyether polyurethane foam: the foam cells. Because the foam cells are bi-stable elastic structures, the foam has two preferred values of strain, and the strain field consists of a high-strain region and a low-strain region separated by a sharp interface. The strain jumps from one preferred value of strain to the other preferred value of strain across the sharp interface. As the penetration of the punch increases during an experiment, the preferred values of strain do not change (since they are strictly properties of the foams); therefore, for the strain field to accommodate the increasing penetration, the interface must expand. For lack of a characteristic length other that the penetration, the sharp interface must expand in a self-similar manner and in direct proportion to the penetration, in what we have termed the self-similar regime. The geometrical simplicity of the self-similar regime makes the punching experiments unexpectedly amenable to analytical treatment. The analysis indicates that the mechanical response depends only on the dimensionality of the punch. For a two-dimensional, wedge-shaped punch the response is linear whereas for a three-dimensional, conical punch the response is quadratic. These straightforward predictions are in accord with the experimental results.

Part II

Initial yielding of ultrathin films

Chapter 6

Surface stress and reversing size effect in the initial yielding of ultrathin films

6.1 Introduction

The mechanical behavior of tiny metallic bodies has long been known to be subject to size effects (Bazant et al., 1997). For example, the yield stress of crystalline whiskers may exceed the yield stress of large crystals of the same material by a factor of 10 or more (Brenner, 1956). With the development of nano technologies in recent years, much new research has been devoted to elucidating size effects in polycrystalline ultrathin films.

One size effect that has drawn much attention pertains to the large strain gradients that arise, for example, in films subjected to bending. This size effect has been ascribed to the high density of geometrically necessary dislocations induced by the strain gradient (Fleck et al., 1994, 1997). Another size effect pertains to the texture (or preferential grain orientation) that is characteristic of thin films grown on crystalline substrates. Because a texture frequently leads to a higher yield stress (Lejeck and Sima, 1983; Grant et al., 1988), this size effect can be readily explained. Still another size effect pertains to the grain size, which in annealed films tends to scale with the thickness of the film (Lejeck and Sima, 1983; Grant et al., 1988). Because smaller grains lead to a higher yield stress, the so-called Hall–Petch relation (Griffin et al., 1987; Venkatraman and Bravman, 1992; Thompson, 1993), or perhaps to a lower yield stress, the reverse Hall–Petch relation, valid for grains smaller than about 10 nm (Schiotz and Jacobsen, 2003), this size effect can be readily explained.

In a recent experimental study (Espinosa et al., 2004), the yield stress of gold films of constant texture and grain size subjected to uniaxial applied tension showed a peculiar size effect. The yield stress increased with diminishing film thickness, up to a thickness

$h = 500\,\text{nm}$. Then, for $h = 300\,\text{nm}$, the yield stress appeared to have remained the same as for $h = 500\,\text{nm}$, indicating that the yield stress had attained a maximum value for $h \approx 400\,\text{nm}$. In another recent, similar experimental study (Saif, 2004), the yield stress of pure aluminum films increased up to a thickness $h = 100\,\text{nm}$; then, for $h < 100\,\text{nm}$, the yield stress started to decrease. This reversing (first hardening, then softening) size effect cannot be explained by any of the models proposed so far, because those models predict a hardening size effect (for constant grain size).

Here we model the film using continuum mechanics. We start by establishing expressions for the compressive stresses induced in the film by the surface stress. After adding these stresses to the applied stress, we use the von Mises yield condition to ascertain the value of the applied stress at initial yielding or *apparent yield stress*. Our results indicate that in films subjected to uniaxial applied tension the surface stress causes a reversing size effect on the apparent tensile yield stress. Using the values of surface stress determined via atomistic methods (Wan et al., 1999), we estimate that this size effect reverses for a thickness on the order of 100 nm, in accord with the experimental results summarized above.

Then, we use the well-known failure criterion proposed Hancock and Mackenzie (1976) to ascertain the mode of failure of the film. Our results indicate that the mode of failure changes from ductile to brittle for thicknesses close to the thickness for which the size effect reverses. These results are in accord with the experimental results of Espinosa et al. (2004).

Last, we show that the surface stress may lead to entirely disparate size effects depending on the applied stress. In particular, we find that in films subjected to biaxial applied tension the surface stress does not lead to a reversing size effect. This finding reconciles the recent experimental results summarized above with J. W. Beams's experiments on gold and silver films, in which the size effect did not reverse even for $h = 20\,\text{nm}$ (Beams, 1959; Menter and Pashley, 1959).

Our work joins a growing body of research in which the surface stress has been found to play a crucial role in several problems at ultrasmall length scales, including the blunting of a crack tip (Carlsson and Thomson, 1988) and the nanoindentation of a crystal (Knap and

Ortiz, 2003).

6.2 Surface stress

The surface stress is a second-rank tensor, $T_{\alpha\beta}$, where the indices α and β run from 1 to 2 and denote in-plane coordinates defined on the surface. (For detailed discussions of the surface stress see, for example, Herring (1953); Cammarata (1994).) To relate the surface stress to the surface energy, γ, using Eulerian coordinates (Nix and Gao, 1998), consider an element of surface of area A that is stretched by an in-plane *elastic* strain $\varepsilon_{\alpha\beta}$. Then, the work performed by the surface stress is $dW = AT_{\alpha\beta}\varepsilon_{\alpha\beta}$, and the energy of the element of surface, γA, changes by $d(\gamma A) = \gamma dA + Ad\gamma = \gamma A\varepsilon_{\mu\mu} + A(\partial\gamma/\partial\varepsilon_{\alpha\beta})\varepsilon_{\alpha\beta}$, where repeated indices imply summation. Equating dW to $d(\gamma A)$ results in the desired expression for the surface stress, $T_{\alpha\beta} = \gamma\delta_{\alpha\beta} + \partial\gamma/\partial\varepsilon_{\alpha\beta}$, where $\delta_{\alpha\beta}$ is the second-rank Krönecker delta. The second term in the expression for $T_{\alpha\beta}$ represents the change in surface energy associated with the elastic stretching of the surface. When the area of a liquid surface is increased, the surface does not stretch elastically, because the atoms in the interior of the liquid are mobile and may readily migrate to the surface. Thus in liquids the second term in the expression for $T_{\alpha\beta}$ vanishes, and the surface stress is isotropic and equal to the surface energy. This is not the case in solids, because in solids the long-range order in the positions of the atoms makes it infeasible for the atoms to migrate to the surface, in particular when the strain applied to the surface amounts to a displacement of a small fraction of the lattice constant. Thus in solids the second term in the expression for $T_{\alpha\beta}$ may not necessarily vanish, and the surface stress is in general anisotropic.

Consider now the crystalline surface of a free-standing crystal. The surface accommodates the lattice constant of the bulk of the material by means of a spontaneous elastic stretching. If the crystalline surface possesses a threefold or higher rotational axial symmetry, then in the expression for $T_{\alpha\beta}$ the term $\partial\gamma/\partial\varepsilon_{\alpha\beta}$ associated with this elastic stretching is isotropic (Wan et al., 1999). That is the case for (111) surfaces in FCC metals. In the experiments

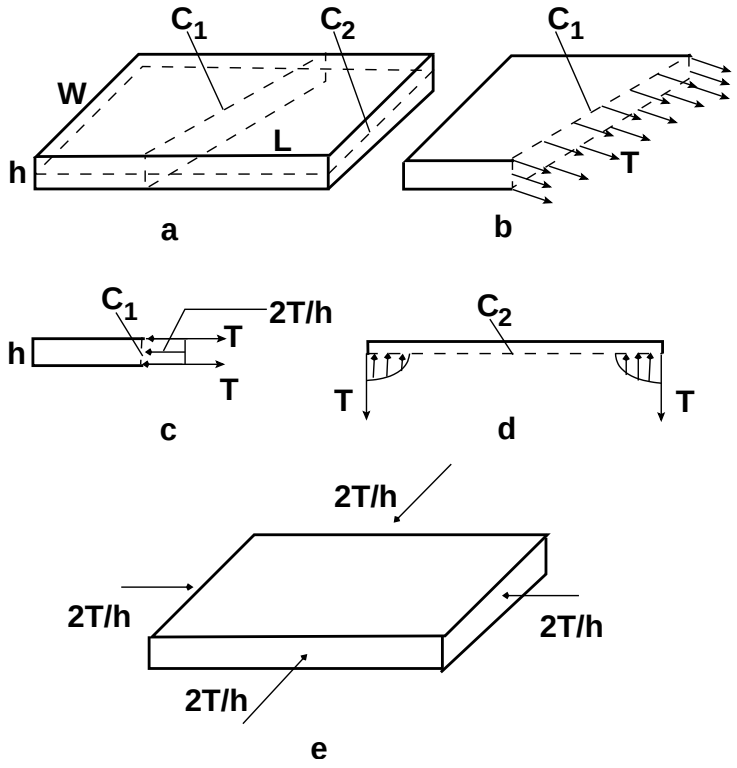

Figure 6.1: (a) A free-standing thin film. C_1 and C_2 are cuts performed for stress analysis. (b) The surface stress T acting on the perimeter of C_1. (c) The compressive stress induced by T on the surface of C_1. (d) The compressive stress induced by T on the surface of C_2. (e) Applied traction that gives the same stresses as T.

of interest here the films had a preferred $\langle 111 \rangle$ crystallographic texture normal to the faces of the films, and we are justified in assuming an isotropic surface stress, $T_{\alpha\beta} = T\delta_{\alpha\beta}$. The surface stress may in principle be either positive (tensile) or negative, but it is positive for FCC metals.

6.3 The surface stress in thin films

Consider a free-standing film of length $L \gg h$ and width $W \gg h$ (Fig. 6.1a). Suppose that the film is severed through its thickness along an arbitrary in-plane direction. (The cut is marked C_1 in Fig. 6.1a.) Then, the surface stress, which we assume to be positive and isotropic, becomes manifest as a tensile force T per unit length of the perimeter of the cut, acting normal to the surface of the cut, as indicated in Fig. 6.1b. If the severed parts of the film are to remain in equilibrium, the surface stress must induce a compressive stress on the

surface of the cut; because the film is very thin, the induced stress is uniform and of value $-2T/h$ on the surface of the cut (Fig. 6.1c). Thus the surface stress induces a compressive stress of value $-2T/h$ in all in-plane directions (Herring, 1953).

Suppose now that the film is severed parallel to its upper and lower faces. (The cut is marked C_2 in Fig. 6.1a.) Then, the surface stress must again induce a compressive stress on the surface of the cut, but now the stress is confined to a very narrow strip (of width $\sim h$) parallel to the lateral edges of the film, as indicated in Fig. 6.1d. Thus in most of the film the surface stress induces no stress in the direction of the thickness of the film.

From our discussion so far, we conclude that in a film of thickness h the stresses induced by the surface stress may be approximately simulated by (i) applying an in-plane compressive traction of value $-2T/h$ on all the lateral edges of the film and (ii) leaving the upper and lower faces of the film traction-free (Fig. 6.1e). This conclusion is valid where the film is thin, i.e., where $L \gg h$ and $W \gg h$.

6.4 Apparent yield stress

Consider now a free-standing thin film to which a uniaxial stress σ_a is applied in the direction of the length of the film. Then, the film is uniformly subjected to principal stresses $\sigma_1 = \sigma_a - 2T/h$, $\sigma_2 = -2T/h$, and $\sigma_3 = 0$ in the direction of the length, the width, and the thickness, respectively. We may ascertain the value of the applied stress at initial yielding or *apparent yield stress*, σ_a^y, by substituting the principal stresses in the von Mises yield condition, $2\sigma_y^2 = (\sigma_1 - \sigma_2)^2 + (\sigma_2 - \sigma_3)^2 + (\sigma_3 - \sigma_1)^2$, where σ_y is the yield stress (Calladine, 2000). The result is

$$\frac{\sigma_a^y}{\sigma_y} = \frac{T}{h\sigma_y} \pm \sqrt{1 - 3\left(\frac{T}{h\sigma_y}\right)^2}. \tag{6.1}$$

Figure 6.2 shows a graphical rendition of (6.1) in the form of a plot of the dimensionless apparent yield stress, σ_a^y/σ_y, vs. the dimensionless thickness, $h\sigma_y/T$. In the plot there is a single curve separating the elastic region (which the curve embraces) from the plastic region. The curve consists of two branches touching at their leftmost points (marked M in Fig. 6.2).

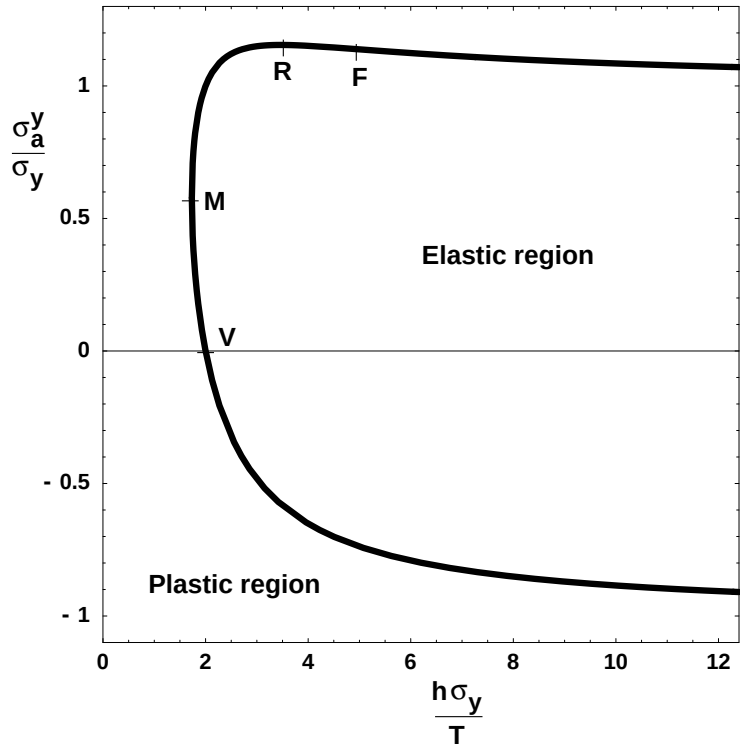

Figure 6.2: A plot of the dimensionless apparent yield stress σ_a^y/σ_y vs. the dimensionless thickness $h\sigma_y/T$. See eq. (6.1). The points F, R, M, and V are referred to in the text. The size effect of the apparent tensile yield stress reverses from hardening to softening at the point R.

The upper branch corresponds to the + sign in (6.1) and gives the apparent tensile yield stress. On the other hand, the lower branch corresponds to the − sign in (6.1) and gives the apparent compressive yield stress. The branches are supported on $h \geq h_M \equiv \sqrt{3}\,T/\sigma_y$ (because the discriminant of (6.1) is negative for $h < h_M$). Therefore, a film of thickness $h < h_M$ cannot be poised between the elastic region and the plastic region, regardless of the applied stress; such a film is always in the plastic region.

Figure 6.2 indicates that for $h \gg T/\sigma_y$ the apparent tensile yield stress is σ_y, and the apparent compressive yield stress $-\sigma_y$. Thus for $h \gg T/\sigma_y$ the initial yielding may be attained by applying a tensile stress σ_y or a compressive stress $-\sigma_y$. This is the expected asymptotic behavior.

Next, we discuss in turn the two branches of Fig. 6.2. Consider first the lower branch, starting with a thin film of thickness $h \gg T/\sigma_y$. If the thickness of the film diminishes, the absolute value of the apparent compressive yield stress decreases (i.e., $d|\sigma_a^y|/dh < 0$), and we say that there is a softening size effect. If the thickness continues to diminish, then, for a thickness $h = h_V \equiv 2\,T/\sigma_y$, the apparent compressive yield stress vanishes, $\sigma_a^y = 0$ (point V in Fig. 6.2). Thus a free-standing film of thickness $h = h_V$ spontaneously attains the initial yielding by virtue of the compressive stresses induced by the surface stress. When a tensile stress is applied to this free-standing film, the film departs from the initial yielding, enters the elastic region, and re-attains the initial yielding at the apparent tensile yield stress given by the upper branch of Fig. 6.2. If the thickness continues to diminish beyond h_V, the apparent compressive yield stress becomes *positive* (i.e., the lower branch of Fig. 6.2 gives a *positive* value of σ_a^y). This positive value of σ_a^y is the minimum tensile stress that must be applied to the film if the film is not to yield by virtue of the *compressive* stresses induced by the surface stress. (Therefore, the name "apparent *compressive* yield stress" remains appropriate, even though this stress is positive.) Last, for a thickness $h = h_M \equiv \sqrt{3}\,T/\sigma_y$, we reach the leftmost point of the lower branch.

Consider now the upper branch of Fig. 6.2, starting with a thin film of thickness $h \gg T/\sigma_y$. If the thickness of the film diminishes, the apparent tensile yield stress increases

(i.e., $d|\sigma_a^y|/dh < 0$), and we say that there is a hardening size effect. If the thickness of the film continues to diminish, then, for a thickness $h = h_F \approx 5\,T/\sigma_y$, the size effect is at its most hardening (i.e., $d^2|\sigma_a^y|/dh^2 = 0$; point F in Fig. 6.2). If the thickness continues to diminish beyond h_F, then the hardening size effect starts to lessen (i.e., $d|\sigma_a^y|/dh$ starts to become less negative). Eventually, for a thickness $h = h_R \equiv 2\sqrt{3}\,T/\sigma_y \approx 3.5\,T/\sigma_y$, the apparent tensile yield stress attains its maximum value, $\sigma_a^y = \sigma_{aR}^y \equiv 2\sigma_y/\sqrt{3} \approx 1.15\,\sigma_y$, and the size effect vanishes (i.e., $d|\sigma_a^y|/dh = 0$; point R in Fig. 6.2). If the thickness continues to diminish beyond h_R, the apparent tensile yield stress decreases (i.e., $d|\sigma_a^y|/dh > 0$), and we say that there is a softening size effect. Thus for a thickness $h = h_V \equiv 2\,T/\sigma_y$ the apparent tensile yield stress equals its original value, $\sigma_a^y = \sigma_y$. Last, for a thickness $h = h_M \equiv \sqrt{3}\,T/\sigma_y \approx 1.73\,T/\sigma_y$, the apparent tensile yield stress equals its minimum value, $\sigma_a^y = \sigma_{aM}^y \equiv \sigma_y/\sqrt{3} \approx 0.58\,\sigma_y$, and we reach the leftmost point of the upper branch.

From our discussion of Fig. 6.2 we conclude that the surface stress causes a size effect on the apparent tensile yield stress. For thin films of thickness $h \gg T/\sigma_y$ there is a hardening size effect, but the size effect reverses from hardening to softening for a thickness $h_R \equiv 2\sqrt{3}\,T/\sigma_y$. Thus the stresses induced in a thin film by the surface stress lead to a size effect of the type recently observed in experiments.

6.4.1 Size effects and the yield condition

We have predicated (6.1) on the von Mises yield condition, $\sigma_e = \sigma_y$. Here σ_e, the *equivalent stress*, quantifies the forcing that tends to produce plastic deformation; it is defined by the expression $2\sigma_e^2 \equiv (\sigma_1 - \sigma_2)^2 + (\sigma_2 - \sigma_3)^2 + (\sigma_3 - \sigma_1)^2$, where σ_1, σ_2, and σ_3 are the principal stresses. This expression for σ_e suitably quantifies the forcing if the plastic deformation occurs by the relative slip of adjacent planes in the material, regardless of the specific mechanisms whereby the slip is effected. (The slip need not be effected by dislocation motion, for example.) In fact, it is the yield stress, σ_y, and not the equivalent stress, σ_e, that depends on the specific mechanisms whereby the slip is effected. Thus the elucidation of size effects consists in determining the dependence of σ_y on the size. Yet this is not the

case for the size effect caused by the surface stress, because this size effect is unrelated to the material. Instead, it is related to the stresses that act *on the bulk of the material* and to the fact that these stresses differ from the applied stresses. The elucidation of this size effect is not a problem in materials science, but rather a problem in solid mechanics.

In (6.1) the size effect caused by the surface stress is coupled to other size effects only through the value of σ_y. Therefore, *in (6.1) the yield stress σ_y is not the yield stress of the bulk material, but the yield stress of the bulk material enhanced by any pertinent size effects other than the size effect caused by the surface stress*.

6.4.2 Comparison with experiments

In Section 6.4, we concluded that the size effect caused by the surface stress reverses from hardening to softening for a thickness $h_R \equiv 2\sqrt{3}\,T/\sigma_y$. To compare the predicted value of h_R with the experimental results, we recall that for $h = h_R$ the (maximum) apparent tensile yield stress is $\sigma^y_{aR} \equiv 2\sigma_y/\sqrt{3}$, and write an expression for h_R in terms of σ^y_{aR}, with the result $h_R = 4T/\sigma^y_{aR}$.

(Note that $\sigma_y = \sigma^y_{aR}\sqrt{3}/2$ is the yield stress of the bulk material enhanced by any size effects other than the size effect caused by the surface stress; see Section 6.4.1. Note also that the expression $h_R = 4T/\sigma^y_{aR}$ can give only a rough estimate of the thickness for which the observed size effect reverses, not only because we have predicated this expression on a number of simplifying assumptions, but also because (a) the value of T may be strongly affected by subtle changes in environmental conditions and (b) σ^y_{aR} is difficult to measure, and tends to be overestimated both in experiments and in atomistic simulations; see, e.g., Schiotz et al. (1999).)

For the pure gold films of the experimental study of reference Espinosa et al. (2004), the reported maximum apparent tensile yield stress was $\sigma^y_{aR} = 170\,\text{MPa}$. Using the surface stress of gold given in reference (Wan et al., 1999), $T = 3.41\,\text{N/m}$, we compute $h_R = 80\,\text{nm}$, which is on the order of magnitude of the thickness for which the observed size effect reversed in that study, $h \approx 400\,\text{nm}$.

For the pure aluminum thin films of the experimental study of Saif (2004), the reported *peak* stress was $\sigma_a^p = 750\,\mathrm{MPa}$, and we estimate $\sigma_{aR}^y = \sigma_a^p/2 = 375\,\mathrm{MPa}$. Using the surface stress of aluminum given in Wan et al. (1999), $T = 2.29\,\mathrm{N/m}$, we compute $h_R = 24\,\mathrm{nm}$, which is on the order of magnitude of the thickness for which the observed size effect reversed in that study, $h \approx 100\,\mathrm{nm}$.

6.4.3 A note on the values of the surface stress used in the comparison with experiments

In the calculations above, we have use the (111) unrelaxed surface stress computed by the modified embedded atom method and reported in Wan et al. (1999). (In this useful reference, the surface stresses and surface energies obtained by a number of methods are given for all FCC metals: Cu, Ag, Au, Ni, Pd, Pt, Al, and Pb. Different methods lead to comparable results, and the results are in good agreement with the few available experimental measurements.) Note that this surface stress corresponds to a free-standing crystal and does not account for the additional elastic stretching undergone by the surface (as well as by the bulk of the material) as the film is stressed to the initial yielding. The required correction is negligible, however. In fact, a straightforward application of the atomistic model of Nix and Gao (1998) allows us to estimate the required correction as $\Delta T \approx 2E\varepsilon a$, where E is the Young's modulus, ε is the strain associated with the additional elastic stretching, and a is the lattice constant; for gold we use $E\varepsilon = \sigma_y = 170\,\mathrm{MPa}$ and $a = 0.3\,\mathrm{nm}$, with the result $\Delta T \approx 0.11\,\mathrm{N/m} \ll T = 3.41\,\mathrm{N/m}$.

Note also that a small increment in the *plastic* deformation brings additional atoms to the surface of the film but does not cause an additional elastic stretching of the surface (or of the bulk of the material) (Nix and Gao, 1998). We conclude that the area of the surface of a film may change as a result of a small increment in plastic deformation, but the surface retains the same structure and remains equally stretched, so that the energy of the surface changes by TdA, where T is the surface stress of the free-standing film, and dA is the change in surface area. As an example of application of this conclusion, consider a film

that undergoes plastic strain increments $d\varepsilon_1$, $d\varepsilon_2$, and $d\varepsilon_3$ in the direction of L, W, and h, respectively, where $d\varepsilon_3 = -(d\varepsilon_1 + d\varepsilon_2)$. The energy of the surface changes by $dW_s = TdA = T\left(2LW(d\varepsilon_1 + d\varepsilon_2) + 2(L+W)hd\varepsilon_3\right) = 2T\left(LW - (L+W)h\right)(d\varepsilon_1 + d\varepsilon_2)$, the stresses in the bulk of the film perform a plastic work $dW_p = (\sigma_1 d\varepsilon_1 + \sigma_2 d\varepsilon_2 + \sigma_3 d\varepsilon_3)LWh$, and the applied traction performs a work $dW_a = \sigma_a LWhd\varepsilon_1$. Equating $dW_a = dW_s + dW_p$ leads to $\sigma_1 = \sigma_a - 2T/h\left(1 - (1 + L/W)h/L\right)$, $\sigma_2 = -2T/h\left(1 - (1 + L/W)h/L\right)$, and $\sigma_3 = 0$, which under the assumption $h/L \ll 1$ simplifies to $\sigma_1 = \sigma_a - 2T/h$, $\sigma_2 = -2T/h$, and $\sigma_3 = 0$, as we concluded before under the same assumption.

6.5 Failure and the ductile-to-brittle transition

Upon attaining the initial yielding, the bulk of the film undergoes permanent deformation in the form of plastic strain increments $\Delta\varepsilon_1 = s_1\,\Delta\lambda$, $\Delta\varepsilon_2 = s_2\,\Delta\lambda$, and $\Delta\varepsilon_3 = s_3\,\Delta\lambda$ in the direction of the length, the width, and the thickness of the film, respectively (Calladine, 2000). Here $\Delta\lambda$ is a dimensionless scalar factor, $s_1 = (\sigma_1 - p)/\sigma_y$, $s_2 = (\sigma_2 - p)/\sigma_y$, $s_3 = (\sigma_3 - p)/\sigma_y$, and $p = (\sigma_1 + \sigma_2 + \sigma_3)/3$. (Note that the plastic deformation is isochoric, $\Delta\varepsilon_1 + \Delta\varepsilon_2 + \Delta\varepsilon_3 = 0$.) By substituting $\sigma_1 = \sigma_a - 2T/h$, $\sigma_2 = -2T/h$, $\sigma_3 = 0$, and $\sigma_a = \sigma_a^y$ (where σ_a^y is the apparent tensile yield stress given by the upper branch of Fig. 6.2), we obtain

$$s_1 = \frac{2}{3}\sqrt{1 - 3\left(\frac{T}{h\sigma_y}\right)^2}, \tag{6.2}$$

$$s_2 = -\frac{T}{h\sigma_y} - \frac{1}{3}\sqrt{1 - 3\left(\frac{T}{h\sigma_y}\right)^2}, \quad \text{and} \tag{6.3}$$

$$s_3 = \frac{T}{h\sigma_y} - \frac{1}{3}\sqrt{1 - 3\left(\frac{T}{h\sigma_y}\right)^2}. \tag{6.4}$$

Figure 6.3 shows a graphical rendition of (6.2–6.4) in the form of plots of the dimensionless quantities s_1, s_2, and s_3 vs. the dimensionless thickness, $h\sigma_y/T$. As was the case for Fig. 6.2, the plots in Fig. 6.3 are supported on $h \geq h_M \equiv \sqrt{3}\,T/\sigma_y$.

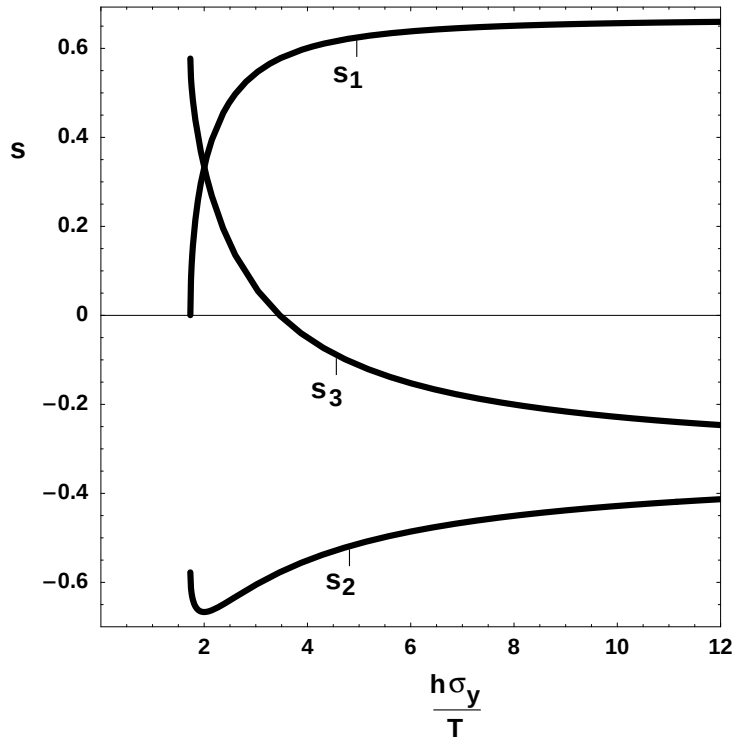

Figure 6.3: A plot of the dimensionless quantities s_1, s_2, and s_3 vs. the dimensionless thickness, $h\sigma_y/T$. See eqs. (6.2–6.4).

Consider now the process whereby the film accumulates plastic deformation, eventually leading to failure in the form of fracture. According to a well-known failure criterion (Hancock and Mackenzie, 1976), the onset of failure occurs when the *equivalent plastic strain*, ε_e, attains a critical value, ε_{ef}, that depends on the triaxiality of the stress in the form

$$\varepsilon_{ef} = \varepsilon_0 \exp\left(-p/\sigma_e\right), \tag{6.5}$$

where the subscript "f" stands for "at failure," ε_0 is a dimensionless constant, p/σ_e is a measure of the triaxiality of the stress, and the equivalent plastic strain is defined by the expression $9\,\varepsilon_e^2/2 = (\Delta\varepsilon_1 - \Delta\varepsilon_2)^2 + (\Delta\varepsilon_2 - \Delta\varepsilon_3)^2 + (\Delta\varepsilon_3 - \Delta\varepsilon_1)^2$. By evaluating ε_e with $\Delta\varepsilon_1 = s_1\,\Delta\lambda$, $\Delta\varepsilon_2 = s_2\,\Delta\lambda$, $\Delta\varepsilon_3 = s_3\,\Delta\lambda$, and the expressions for s_1, s_2, and s_3 given by (6.2–6.4), we obtain $\varepsilon_e = 2\,\Delta\lambda/3$; therefore, the value of $\Delta\lambda$ at failure is $\Delta\lambda_f = 3\,\varepsilon_{ef}/2$. On the other hand, by setting $\sigma_e = \sigma_y$ and evaluating p with $\sigma_1 = \sigma_a - 2T/h$, $\sigma_2 = -2T/h$, $\sigma_3 = 0$, and $\sigma_a = \sigma_a^y$ (where σ_a^y is the apparent tensile yield stress given by the upper branch

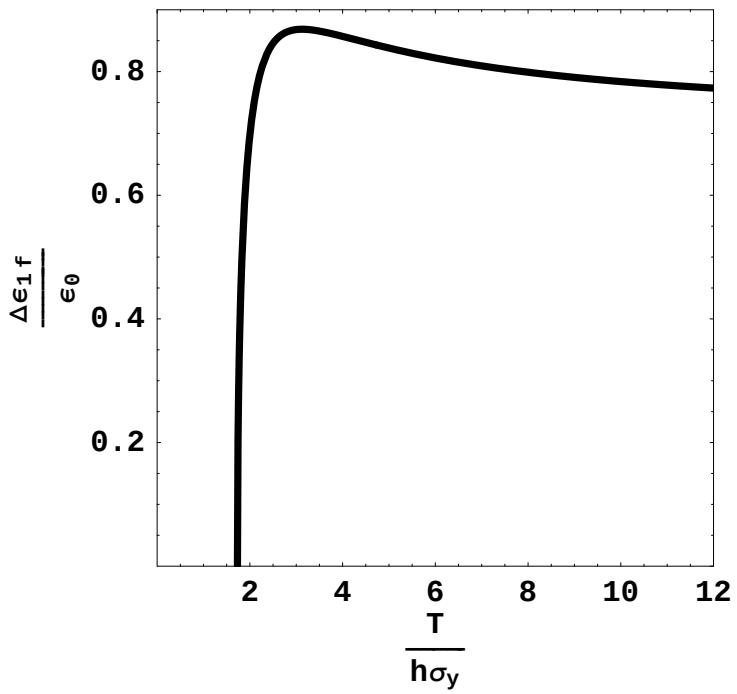

Figure 6.4: A plot of the normalized plastic strain at failure in the direction of the applied stress vs. the dimensionless thickness, $h\sigma_y/T$. See eq. (6.6).

of Fig. 6.2), we obtain $p/\sigma_e = -s_3$. Since $\Delta\lambda_f = 3\,\varepsilon_{ef}/2$ and $p/\sigma_e = -s_3$, we can recast (6.5) in the form $\Delta\lambda_f = (3/2)\,\varepsilon_0 \exp(s_3)$, and write an expression for the plastic strain at failure *in the direction of the applied stress*, $\Delta\varepsilon_{1f}$, as follows:

$$\Delta\varepsilon_{1f} = (3/2)\,\varepsilon_0\, s_1 \exp(s_3). \tag{6.6}$$

Fig. 6.4 shows a graphical rendition of (6.6) in the form a plot of $\Delta\varepsilon_{1f}/\varepsilon_0$ vs. the dimensionless thickness, $h\sigma_y/T$. From the plot in Fig. 6.4, we conclude that the plastic strain at failure in the direction of the applied stress (a measure of the apparent ductility of the film) reaches a maximum thickness $h = h_R$, it diminishes as the film becomes thinner, and it vanishes for a thickness $h = h_m$.

In other words, the failure becomes increasingly brittle as the film becomes thinner. Further, the rate of embrittlement becomes very strong for thicknesses close to the thickness for which the size effect reverses, $h_R = 2\sqrt{3}\,T/\sigma_y$.

Our conclusions from the previous paragraph are in accord with the results of recent experiments on gold films (Espinosa et al., 2004), in which a ductile-to-brittle transition was documented for a thickness on the order of 100 nm.

6.6 Biaxial loading

To inquire further into the size effect caused by the surface stress, we now consider a type of experiment known as the *bulge test*. In the bulge test, a film of thickness h is placed across the open end of a circular tube of radius $R \gg h$. Then, the pressure of the air in the tube is increased to a value p, whereupon the film deflects to form a bulge of height $b \ll R$. As a result, the film is subjected to a *biaxial*, in-plane isotropic applied stress $\sigma_a = pR^2/4bh \gg p$. In a classic experimental study, J. W. Beams used the bulge test to determine the apparent yield stress of polycrystalline gold and silver films of thicknesses in the range of 200 to 20 nm (Beams, 1959). He concluded that the apparent yield stress increased monotonically with diminishing film thickness. Thus, in contrast with the recent experimental studies summarized above, a reversing size effect was *not* observed in Beam's classical experimental study.

To understand this discrepancy, we substitute the principal stresses of the bulge test ($\sigma_1 = \sigma_a - 2T/h$, $\sigma_2 = \sigma_a - 2T/h$, and $\sigma_3 = 0$) in the von Mises yield condition, with the result

$$\frac{\sigma_a^y}{\sigma_y} = \pm 1 + 2\frac{T}{h\sigma_y}, \tag{6.7}$$

where σ_a^y is the apparent yield stress. It is straightforward to show that this same size effect is valid for wires. For atomistic simulations in ultrathin wires, see, for example,Gall et al. (2004). Equation (6.7) predicts a hardening size effect in the apparent tensile yield stress measured in bulge tests, as expected. In a 1959 review paper (Menter and Pashley, 1959), Beams is said to have first ascribed the hardening size effect observed in his experiments to the surface *energy*. In the same paper, a plot is shown and attributed to Beams which might be a graphical rendition of (6.7). Unfortunately, Beams appears not to have published the

equations leading to this plot. (He subsequently came to the conclusion that the size effect observed in his experiments could not be ascribed to the surface energy, because for relatively thick thin films the predicted size effect fell short of the observed size effect (Menter and Pashley, 1959). It was thought at the time that the observed size effect should be ascribed to a *single* reason.)

From our discussion of the bulge test we conclude that, in contrast with our results for thin films subjected to a uniaxial applied stress, the surface stress does not lead to a reversing size effect in thin films subjected to a biaxial, isotropic applied stress.

6.7 Discussion

Recent experiments (Espinosa et al., 2004) indicate that the yield stress of thin films of constant texture and grain size subjected to uniaxial applied tension is subject to a peculiar size effect. At first, the yield stress increases with diminishing film thickness. Then, the yield stress is observed to attain a maximum value, whereupon a further decrease in the thickness of the film leads to a decrease in the yield stress. In this chapter, we have been concerned with this reversing (first hardening, then softening) size effect.

We have formulated a continuum model model which has allowed us to conclude that in ultrathin, polycrystalline metallic films of constant grain size the surface stress leads to a size effect in the initial yielding. This size effect depends strongly on the applied stress. Where the applied stress is uniaxial, we have predicted that the size effect reverses for a film thickness h_R that can be estimated using values of the surface stress determined via atomistic methods. The result, $h_R \approx 100\,\text{nm}$, is in accord with experiments. In addition, we have predicted that the mode of failure of the film changes from ductile to brittle for thicknesses close to h_R, also in accord with experiments.

Where the applied stress in biaxial, we have predicted a strong size effect, but the size effect remains hardening for any film thickness, so that there should be no size-effect reversal. This prediction is in accord with little-known but remarkable experiments performed 50 years

ago by J. W. Beams (Beams, 1959). In these biaxial experiments with gold and silver films, the size effect did not reverse even for a film thickness as low as 20 nm.

Our work joins a body of research in which the surface stress has been found to play a crucial role in several problems at ultrasmall length scales, including the blunting of a crack tip (Carlsson and Thomson, 1988) and the nanoindentation of a crystal (Knap and Ortiz, 2003). Given that the film thickness for which the size effect reverses is only about 100 times a typical lattice parameter, our conclusions add to a growing realization of the robustness of continuum mechanics at ultra-small length scales, a realization that has been commented upon by a number of authors (for a recent, eloquent example from the field of microfluidics, see Sharp and Adrian (2004)).

Chapter 7

Summary and conclusions

In the first part of this work, we have studied the mechanical behavior of elastic polyether polyurethane (EPP) foams by means of experiments, theory, and models. We designed our experiments with four observations in mind.

1. In most engineering applications of EPP foams, the foams are subjected to multiaxial loading, yet there has been scant research on the mechanical response of EPP foams under multiaxial states of stress.

2. The mechanical response of an EPP foam depends not just quantitatively but also qualitatively on the relative density of the foam, yet no experiments have been reported for a series of EPP foams of widely differing densities.

3. EPP foams are commonly subjected to large strains under service conditions, yet there have been few measurements of complete stress-strain curves, and these measurements have been mostly limited to uniaxial tests.

4. In tests in which the stress field is spatially homogeneous, a stress plateau is a frequent occurrence and appears to be invariably accompanied by heterogeneous strain fields, yet measurements of the strain fields have only been performed in a few uniaxial tests.

We have conducted an unprecedented set of experiments on a commercial series of EPP foams. This commercial series of EPP foams consists of five different foams covering the entire range of densities commonly used in applications. We have tested each foam under five different loading cases including uniaxial, biaxial, and triaxial loading cases. In each test we have measured a complete stress–strain curve up to large strains on the order of 50%.

For several tests we have also used a global digital image correlation method to ascertain the nature of the strain fields.

Consistent with earlier experimental results, we have found that EPP foams can be classified into low-density foams and high-density foams on the basis of the stress-strain curves measured under uniaxial compression along the rise direction. The stress-strain curves of low-density foams exhibit a stress plateau whereas the stress-strain curves of high-density foams harden monotonically. Among the foams of our experiments, we have found the three foams of lower density to be low-density foams.

We have determined that the classification of foams into low-density foams and high-density foams holds consistently for all loading cases. The same three foams of lower density, and then only those three foams, gave a stress plateau under every loading case in which stress plateaus were observed.

We have confirmed that a stress plateau in the mechanical response of a low-density foam is invariably accompanied by heterogeneous strain fields. These heterogeneous strain fields display two preferred values of strain; an increase in the applied mean strain is accommodated by growth of the volume fraction of one of the preferred values of strain at the expense of the volume fraction of other preferred value of strain.

Our experimental findings are inconsistent with currently available models of elastic foams. In these models, the microstructure of a foam undergoes a bifurcation of equilibrium (Euler buckling); the plateau stress corresponds to an eigenvalue; and the attendant strain field corresponds to an eigenfunction of arbitrary amplitude. As the applied mean strain is increased following buckling, the stress-strain curve traces a stress plateau. The strain field remains invariant except for its amplitude, which increases to accommodate the applied mean strain. But a strain field that remains invariant except for its amplitude cannot be reconciled with the experiments, where the strain fields display two fixed, preferred values of strain, and an increase in the applied mean strain is accommodated by growth of the volume fraction of one of the preferred values of strain at the expense of the volume fraction of other preferred value of strain.

We have argued that the conjunction of stress plateaus and strain fields with two preferred values of strain indicates that at large strains the deformation of EPP foams is dominated by a phase transition. Thus we have ascribed the preferred values of strain observed in experiments to two configurational phases of the foam, and identified the strain fields observed in experiments and the attendant plateau stress with two-phase strain fields and a Maxwell stress, respectively.

We have formulated a 3D model of EPP foams. In this model, a unit cell composed of several bars is cut off from an idealized, perfectly periodic foam microstructure. The tips of the bars of the unit cell are subjected to a set of displacements affine with the applied mean deformation gradient, and left to rotate freely. This is, therefore, a mean-field model.

The unit cell is characterized using a few physically meaningful material and geometric parameters whose values may be readily estimated for any given foam. As we have been mostly interested in the mechanical response at large strains, we have adopted for the sake of simplicity a linear elastic model for the polyether polyurethane.

We have verified that for uniaxial compressive loading along the rise direction the model predicts configurational phase transitions, stress plateaus, and two-phase strain fields for low-density foams; a critical point for foams of critical density; and monotonically hardening stress-strain curves and homogeneous strain fields for high-density foams. The critical exponents associated with the critical point are the same as in other mean-field models such as the Van der Walls model of a fluid. These predictions are consistent with, and provide a straightforward theoretical interpretation to, the experimental results.

From an analysis of the model, we have concluded that the mechanical response of EPP foams is dominated at large strains by either one of two mechanisms.

1. Snap-through buckling of a foam cell, a mechanism that entails nonconvex strain energy functions, stress plateaus, and two-phase strain fields. Snap-through buckling represents the attainment of a limit point. In contrast to Euler buckling, a global mechanism in which the entire microstructure of a foam is engaged at once, snap-through buckling is

a local mechanism that sweeps progressively through the microstructure of the foam. Here a foam cell is slender and undergoes a discontinuous transition between two characteristic configurational phases, without bifurcation of equilibrium.

2. Bending of a foam cell, a mechanism that entails convex strain energy functions, monotonically increasing stresses, and homogeneous strain fields. Here a foam cell is thickset and deforms continuously and in concert with all the other cells.

We have calibrated the model and shown that with a suitable choice of parameters, the model gives predictions in good accord with all our experiments.

To the best of our knowledge, we are the first to have compared experimental and predicted stress-strain curves for numerous loading cases and a complete series of foams of widely differing densities. We have shown that the model is capable of reproducing all the trends evinced in the experimental stress-strain curves. Further, even though we have not made a special effort at curve fitting, the model gives good fits for all loading cases with the exception of the triaxial loading case, where the fits can be said to be reasonable.

We have noted, however, that the goodness of a model of EPP foams cannot consist in the capacity of the model to give close fits to numerous stress-strain curves measured in experiments. The model should be able to account for all the relevant experimental evidence, and our experiments indicate that in EPP foams the character of a stress-strain curve is closely linked to the character of the attendant strain fields, which have hardly been the subject of any research.

Thus, in judging the performance of our model, we have highlighted the capacity of the model to give a nonconvex strain energy function—the signature of a phase transition, which entails the conjunction of a stress plateau and two-phase strain fields—where and only where our experiments evinced a stress plateau and two-phase strain fields. We have submitted that this should remain a fundamental criterion of goodness in the evaluation of constitutive models of EPP foams.

We have performed an extensive experimental and theoretical study of punching in EPP foams. The motivation for this study has been the fact that EPP foams are widely used in packaging, helmets, car seats, sandwich panels, and other applications where an EPP foam is subjected to punching.

In experiments in which a low-density EPP foam specimen was penetrated with a wedge-shaped punch, we have found that the force–penetration curve remained linear up to a penetration of the punch of about 40% of the height of the specimen. Then, as the penetration proceeded, the mechanical response became nonlinear and might evince an abrupt lessening or increase in stiffness, depending on the aspect ratio of the specimen.

To explain these surprising experimental results, we have proposed that in a foam specimen subjected to punching the strain field consists of a high-strain phase in a region close to the tip, where a phase transition has already taken place, and a low-strain phase in a region far from the tip, where the phase transition is yet to take place. The two configurational phases must be separated by a sharp interface, and we have used a global DIC method to trace the sharp interface as it grew and swept through a specimen during a test.

By studying theoretically the self-similar growth of the sharp interface between the two configurational phases of a foam, we have predicted a linear response within the self-similar regime, in accord with the experimental observations. We have also shown that the force-penetration curves for foams of different densities can be made to collapse onto a single curve within the self-similar regime, provided that each individual curve is scaled by the plateau stress of the corresponding foam.

We have argued that the self-similar regime ends when the sharp interface reaches one of the boundaries of the specimen. Depending on the aspect ratio of the specimen, the sharp interface will first reach either a lateral boundary or the lower boundary. If a lateral, unsupported boundary is reached first, the mechanical response will display a momentary loss of stiffness. If the lower, fixed boundary is reached first, the mechanical response will display a sizable increase in stiffness. We have shown these predictions to be in accord with our experimental results.

By applying the same theory to the case of a conical punch, we have predicted a quadratic response within the self-similar regime and verified our prediction by performing experiments with a conical punch.

We have concluded that in the self-similar regime the mechanical response is ruled entirely by geometry, and depends only on the dimensionality of the punch and the plateau stress of the low-density foam. Thus the self-similar regime is a direct manifestation of the occurrence of a phase transition.

In the second part of this thesis, we have undertaken a theoretical study of the initial yielding of ultrathin metallic films. It has recently been found that in free-standing metallic films of constant grain size the initial yield stress increases as the film becomes thinner, it peaks for a thickness on the order of 100 nm, and then starts to decrease. This reversing (first hardening, then softening) size effect has posed two challenges: (1) It cannot be explained using currently available models and (2) it appears to contradict the classical experimental results of J. W. Beams [1959], in which the size effect in bulge tests did not reverse even for a thickness of 20 nm.

We have shown that the reversing size effect can be explained and the contradiction dispelled by taking into account the effect of the surface stress on the initial yielding. We have used a simple continuum model to predict that the mode of failure of a film changes from ductile to brittle for a thickness on the order of 100 nm, in accord with experimental measurements.

We have concluded that our successful application of methods of continuum mechanics to films as thin as 100 times a typical lattice parameter adds to a growing realization of the robustness of these methods at ultrasmall length scales.

References

Artavia L. D. and Macosko C. W., 1994, "Polyurethane flexible foam formation," in *Low density cellular plastics: Physical basis of behavior*, edited by Hilyard N. C. and Cunningham A. (Chapman and Hall, London), pp. 22–55.

Bart-Smith, H., Bastawros, A. F., Mumm, D. R., Evans, A. G., Sypeck, D. J., Wadley, H. N. G., 1998, "Compressive deformation and yielding mechanisms in cellular Al alloys determined using X-ray tomography and surface strain mapping," Acta. Mater., **46**, pp. 3583–3592.

Bastawros, A. F., Bart-Smith, H., Evans, A. G., 2000, "Experimental analysis of deformation mechanisms in a closed-cell aluminum alloy foam," J. Mech. Phys. Solids, **48**, pp. 301–322.

Bayer, O., 1947, "Das di-isocyanat-polyadditionsverfahren (polyurethane)," Angewandte Chemie, **59**, pp. 257–272.

Bazant, Z. P., and Chen, E. P., 1997, "Scaling of Structural Failure," Appl. Mech. Reviews, **10**, pp. 593–527.

Beams, J. W., 1959, "Mechanical Properties of Thin Films of Gold and Silver," in *Structure and Properties of Thin Films*, edited by Neugebauer, C. A., Newkirk, C. A., and Vermilyea, D. A. (John Willey & Sons, New York), pp. 183–198.

Berfield T. A., Patel J. K., Shimmin R. G., Braun P. V., Lambros J., and Sottos N. R., 2006, "Fluorescent Image Correlation for Nanoscale Deformation Measurements," Small **2**, pp. 631–635.

Borodich F. M., 1983, "Similarity in the problem of contact between elastic bodies," J. Appl. Math. Mech., **47**, pp. 519–521.

Borodich F. M., 1989, "Hertz contact problems for an anisotropic physically nonlinear elastic medium," Strength. Mater., **12**, pp. 1668–1676.

Brakke K., "The surface evolver," Experimental Mathematics, **1**, pp. 141–165.

Brenner, S. S., 1956, "Tensile Strength of Whiskers," J. Applied Phys., **27**, pp. 1484–1491.

Brydona A. D., Bardenhagena S. G., Millerb E. A., and Seidlerb G. T., 2005, "Simulation of the densification of real open-celled foam microstructures," J. Mech. Phys. Solids, **53**, pp. 2638–2660.

Cammarata, R. C., 1994, "Surface and Interface Stress Effects in Thin-Films," Prog. Surf. Sci., **46**, pp. 1–38.

Calladine, C. R., *Plasticity* (Horwood Publishing Ltd., Chichester, UK, 2000), p. 48.

Cao, Y., Bly, R., Moore, W., Gao, Z., Cuitiño, A. M., Soboyejo, W. O., 2006, "Investigation of viscoelasticity of human osteosarcoma cells using shear assay experiments," J. Mater. Res., **21**, pp. 1922–1930.

Cao, Y., Bly R., Moore W., Gao Z., Cuitiño A. M., Soboyejo W. O., 2007, "On the measurement of human osteosarcoma cell elastic modulus using shear assay experiments," J. Mater. Sci. Mater. Med., **18**, pp. 103–109.

Carlsson, A. E. and Thomson, R., 1988, "Fracture Toughness of Materials: From Atomistics to Continuum Theory," Solid State Phys., **51**, pp. 233–280.

Cardenas-Garcia, J. F., Yao, H., Zheng, S., Zartman, R. E., 1998, "Digital image correlation procedure to characterize soil surface layer cracking," Agronomy J., **90**, pp. 438–441.

Chao, Y. J., Luo, P. F., Kalthoff, J. F., 1998, "An experimental study of the deformation fields around a propagating crack tip," Exp. Mech., **38**, pp. 79–85.

Chen, C., Lu, T. J. and Fleck, N. A., 1999, "Effect of imperfections on the yielding of two-dimensional foams," J. Mech. Phys. Solids, **47**, pp. 2235–2272.

Chung, J. and Waas, A. M., 2002, "Compressive response of circular cell polycarbonate honeycombs under inplane biaxial static and dynamic loading. Part I: experiments," Int. J. Impact Eng., **27**, pp. 729–754.

Chung, J. and Waas, A. M., 2002, "Compressive response of circular cell polycarbonate honeycombs under inplane biaxial static and dynamic loading - Part II: simulations," Int. J. Impact Eng., **27**, pp. 1015–1047.

Coniglio, A., Fierro, A., Nicodemi M., Pica Ciamarra M. and Tarzia M. , 2005, "Statistical mechanics of dense granular media," J. Phys. Condens. Matter, **17**, pp. 2557–2572.

Dai, X., and Gioia, G., 2008, "Critical exponents in elastic foams," Proceedings of the 10th Pan American Congress of Applied Mechanics (PACAM X), pp. 331–334.

Daxner, T., 2003, *Multi-Scale modeling and simulation of metallic foams*, PhD thesis, by VDI Verlag

Deshpande, V. S. and Fleck, N. A., 2001, "Multi-axial Yield Behaviour of Polymer Foams," Acta mater., **49**, pp. 1859–1866.

Espinosa, H. D., Prorok, B. C., and Peng, B., 2004, "Plasticity Size Effects in Free-Standing Submicron Polycrystalline FCC Films Subjected to Pure Tension," J. Mech. Phys. Solids, **52**, pp. 667–689.

Fleck, N. A., Muller, G. M., Ashby, M. F., Hutchinson, J. W., 1994, "Strain Gradient Plasticity: Theory and Experiment," Acta Metall. Mater., **42**, pp. 475–487.

Fleck, N. A., and Hutchinson, J. W., 1997, "Strain Gradient Plasticity," Adv. Appl. Mech., **33**, pp. 295–261.

Galanov, B. A., 1981, "Approximate solution to some problems of elastic contact of two bodies," Mech. Solids, **16** pp. 61–67.

Gall, K., Diao, J., and Dunn, M. L., 2004, "The Strength of Gold Nanowires," Nanoletters, **4**, pp. 2431–2436.

Gao, Z., Wang, Y., Gioia, G., and Cuitiño, A. M. 2002, "A Global Approach for Digital Speckle Correlation," Proceedings of the 2002 SEM Annual Conference & Exposition on Experimental and Applied Mechanics, Society for Experimental Mechanics, pp. 250–254.

Gao, Z. and Desai, J. P., 2009, "Estimating zero-strain states of very soft tissue under gravity loading using digital image correlation," Med. Image Anal., **14**, pp. 126–137.

Gdoutos E. E., Daniel I. M. and Wang K. A., 2002, "Failure of Cellular Foams under Multiaxial Loading," Compos. A: Appl. Sci. Manuf., **33**, pp. 163–176.

Gent, A. N., Thomas, A. G., 1963, "Mechanics of foamed elastic materials," Rubber Chem. Tech., **36**, pp. 597–610.

Gibson L. J., Ashby M. F., Schajer, G. S. and Robertson, C. I., 1982, "The mechanics of two-dimensional cellular materials," Proc. R. Soc. Lond, **A382**, pp. 25–42.

Gibson L. J and Ashby M. F., 1982, "The mechanics of three-dimensional cellular materials," Proc. R. Soc. Lond, **A382**, pp. 43–59.

Gibson, L. J. and Ashby, M. F., 1997, *Cellular Solids: Structure and Properties*, 2nd ed. Cambridge University Press, UK

Gioia, G., Wang, Y. and Cuitiño, A. M., 2001, "The energetics of heterogeneous deformation in open-cell solid foams," Proc. R. Soc. Lond. A, **457**, pp. 1079–1096.

Global Industry Analyst, Inc., 2008 "Polymeric foams: a global strategic business report", CODE: MCP-1174

Goldenfeld, N., 1992, *Lectures on Phase Transition and the Renormalization Group (Frontiers in Physics, 85)*, by Westview Press.

Gong, L., Kyrikides, S., and Jang W. Y., 2005, "Compressive response of open-cell foams, part i: Morphology and elastic properties," Int. J. Solid. Struct., **42**, pp. 1355–1379.

Gong, L., and Kyriakides, S., 2005, "Compressive response of open cell foams, Part II: Initiation and evolution of crushing," Int. J. Solid. Struct., **42**, pp. 1381–1399.

Gong, L., 2005, *The compressive response of open-cell foams*, PhD thesis, The University of Texas at Austin

Grant, E. M., Hansen, N., Jensen, D. J., Ralph, B., Stobbs, W. M., 1988, "Texture Development During Grain Growth in Thin Films," in *Proceedings of the Eighth International Conference on Texture of Materials*, edited by Kallend, J. S., and Gottstein, G. (Springer-Verlag, New York).

Griffin, A. J., Brotzen, F. R., and Dunn, C. F., 1987, "Mechanical-Properties and Microstructures of Al-1-Percent-Si Thin-Film Metallizations," Thin Solid Films, **150**, pp. 237–244.

Hancock, J. W., and Mackenzie, A. C., 1976, "On the Mechanisms of Ductile Failure in High-Strength Steels Subjected to Multi-Axial Stress States," J. Mech. Phys. Solids, **24**, pp. 147–169.

He, Z. H., Sutton, M. A., Ranson, W. F., and Peters, W. H., 1984, "Two-dimensional fluid-velocity measurements by use of digital-speckle correlation techniques," Exp. Mech., **24**, pp. 117–121.

Herring, C., 1953, in *Structure and Properties of Solid Surfaces*, edited by Gomer, R. and Smith, C. S. (The University of Chicago Press).

Jang W. Y., Kraynik A. M., and Kyriakides S., 2008, "On the microstructure of open-cell foams and its effect on elastic properties," Int. J. Solid. Struct., **45**, pp. 1845–1875.

Knap, J. and Ortiz, M., 2003, "Effect of Indenter-Radius Size on Au(001) Nanoindentation," Phys. Rev. Lett., **90**, 226102.

Lakes, R., Rosakis, P., and Ruina A., 1993, "Microbuckling Instability in Elastomeric Cellular Solids," J. Mater. Sci. **28**, pp. 667–4672.

Laroussi M., Sab A., and Alaoui A., 2002, "Foam mechanics: nonlinear response of an elastic 3D-periodic microstructure," Int. J. Solid. Struct., **39**, pp. 3599–3623.

Lejeck P., and Sima, V., 1983, "Orientational Relationships in the Secondary Recrystallization of Pure Nickel," Mater. Sci. Eng., **60**, pp. 121–124.

Lockwood, W. D. and Reynolds, A. P., 1999, "Use and verification of digital image correlation for automated 3-D surface characterization in the scanning electron microscope," Mater. Characterization, **42**, pp. 123–134.

Lu, H., 1998, "Applications of digital speckle correlation to microscopic strain measurement and materials property characterization," J. Electron. Packag., **120**, pp. 275–279.

Maire E., Fazekasb A., Salvob L., Dendievelb R., Youssefa S., Cloetensc P. and Letangd J. M., 2003, "X-ray tomography applied to the characterization of cellular materials Related finite element modeling problems," Compos. Sci. Tech., **63**, pp. 2431–2443.

Ma, l., Zhou, J. et al, 2002, "Self-similarity simplification approaches for the modeling and anlysis of Rockwell hardness indentation," J. Res. Natl. Inst. Stand. Technol., **107**, pp. 401–412.

Magnenet, V., Rahouadj R., Bacher P., and Cunat C., 2008, "Inelastic constitutive relations for foamed materials: A statistical approach and its application to open-cell melamine," Mech. Mater., **40**, pp. 673–684.

Mehta A and Edwards S. F., 1989, "Statistical mechanics of powder mixtures," Physica A, **157**, pp. 1091–1097.

Maji A. k, Schreyer H. l, Donald S, Zuo Q and Satpathi D, 1995, "Mechanical Properties of Polyurethane Foam Impact Limiters," J. Eng. Mech., **121**, pp. 528–540.

Makse, H. A. and Kurchan J., 2002, "Testing the thermodynamic approach to granular matter with a numerical model of a decisive experiment," Nature, **415**, pp. 614–616.

Menges G., Knipschild F., 1975, "Estimation of mechanical-properties for rigid polyurethane foams," Polymer Eng. Sci., **15**, pp. 623–627

Menter, J. W. and Pashley, D. W., 1959, "The Microstructure and Mechanical Properties of Thin Films," in *Structure and Properties of Thin Films*, edited by Neugebauer, C. A., Newkirk, C. A., and Vermilyea, D. A. (John Willey & Sons, New York), pp. 111–150.

MILLS, N. J., 1997, "Time dependence of the compressive response of polypropylene bead foam," CELLULAR POLYMERS, **16**, pp. 194–215.

MILLS, N. J., FITZGERALD, C., GILCHRIST, A. and VERDEJO R, 2003, "Polymer foams for personal protection: cushions, shoes and helmets," Compos. Sci. Tech., **63**, pp. 2389–2400.

Mizuno, Y., Kawasaki, A. and Watanabe, R., 1995, "In situ measurement of sintering shrinkage in powder compacts by digital image correlation method," Powder Metallurgy, **38**, pp. 191–195.

Mohr, D. and Doyoyo, M. A., 2003, "New Method for the Biaxial Testing of Cellular Solids," Exp. Mech., **43**, pp. 173–182.

Mullins L., 1969, "Softening of rubber by deformation," Rub. Chem. Technol., **42**, pp. 339–362.

Myriam L., Karam S. and Amina A., 2002, "Foam mechanics: nonlinear response of an elastic 3D-Peiodicmicrostructure," Int. J. Solid. Struct., **39**, pp. 3599–3623.

Nix, W. D. and Gao, H., 1998, "An Atomistic Interpretation of Interface Stress," Scripta Mater., **39**, pp. 1653–1661.

Okumura D., Ohno N. and Noguchi H., 2004, "Elastoplastic microscopic bifurcation and post-bifurcation behavior of periodic cellular solids," J. Mech. Phys. Solids, **52**, pp. 641–666.

Overaker D. W., Cuitiño A. M. and Langrana N. A., 1998, "Elastoplastic micromechanical modeling of two-dimensional irregular convex and nonconvex (re-entrant) hexagonal foams," Trans. ASME J. Appl. Mech., **65**, pp. 748–757.

Papka S. D. and Kyriakides S., 1994, "In-plane compressive response and crushing of honeycomb," J. Mech. Phys. Solids, **42**, pp. 1499–1532.

Papka, S. D. and Kyriakides, S., 1999, "Biaxial crushing of honeycombs - Part I: Experiments," Int. J. Solid. Struct., **36**, pp. 4367–4396.

Papka, S. D. and Kyriakides, S., 1999, "In-plane biaxial crushing of honeycombs - Part II: Analysis," Int. J. Solid. Struct., **36**, pp. 4397–4423.

Patel N. R. and Finnie I., 1970, "Structural features and mechanical properties of rigid cellular plastics," J. Mater., **5**, pp. 909–932.

Plateau J. A. F., 1873, *Statique Expérimentale et Théorique des Liquides soumis aux Seules Forces Moléculaires*, (Gauthier-Villars, Paris) .

Reyes, A., Hopperstad, O. S., Berstad, T., Hanssen, A. G. and Langseth, M., 2003, "Constitutive modeling of aluminum foam including fracture and statistical variation of density," Eur. J. Mech. A Solids, **22**, pp. 815–835.

Sabuwala T., Dai X., and Gioia G., Large Deformation Behavior of Low Density Open Cell Foams. 2007 ASME Applied Mechanics and Materials Conference, Austin, Texas

Saif, T., 2004, "Scaling the Depths," Mech. Engr., **126**, pp. 8–11. See also Haque, A., 2002, "Length-Scale Effects on Nano-Scale Materials Behavior," PhD Thesis, Department of Mechanical Engineering, University of Illinois at Urbana-Champaign.

Schiotz, J., Vegge, T., Di Tolla, F. D., and Jacobsen, K. W., 1999, "Atomic-scale Simulations of the Mechanical Deformation on Nanocrystalline Metals," Phys. Rev. B, **60**, pp. 11971–11983.

Schiotz, J. and Jacobsen, K. W., 2003, "A Maximum in the Strength of Nanocrystalline Copper," Science, **301**, pp. 1357–1359.

Schraad M. W., and Harlow F. H., 2006, "A stochastic constitutive model for disordered cellular materials: Finite-strain uni-axial compression," Int. J. Solid. Struct., **43**, pp. 3542–3568.

Sharp, K. V., and Adrian R. J., 2004, "Transition from Laminar to Turbulent Flow in Liquid Filled Microtubes," Exp. Fluids, **36**, pp. 741–747.

Shaw, M. C., and Sata, T., 1966, "The Plastic Behavior of Cellular Materials," Int. J. Mech. Sci., **8**, pp. 469–478.

Sudheer Kumar, P., Ramachandra S. and Ramamurty U., 2003, "Effect of displacement-rate on the indentation behavior of an aluminum foam," Mater. Sci. Eng. A, **347**, pp. 330–337.

Sullivan R. M., Ghosn L. J. and Lerch B. A., 2008, "A general tetrakaidecahedron model for open-celled foams," Int. J. Solid. Struct., **45**, pp. 1754–1765.

Timoshenko, S. P., 1956, *Strength of Materials; Part III, Advanced Theory and Problems*, (D. Van Nostrand Co., Princeton, New Jersey, Third Edition edition)

Thompson, W. (Lord Kelvin), 1887, "On the division of space with minimal partitional area," Phil. Mag., **24**, pp. 503–514.

Thompson, C. V., 1993, "The Yield Stress of Polycrytalline Thin Films," J. Mater. Res., **8**, pp. 237–238.

Triantafillou, T. C., Zhang, J. ,Shercliff, T. L., Gibson, L. J. and Ashby, M. F., 1989, "Failure Surfaces for Cellular Materials under Multiaxial Loads–II. Comparison of Models with Experiment," Int. J. Mech. Sci., **31**, pp. 665–678.

Triantafyllidis, N. and Schraad, M. W., 1998, "Onset of failure in aluminum honeycombs under general in-plane loading," J. Mech. Phys. Solids, **46**, pp. 1089–1124.

Venkatraman, R., and Bravman, J. C., 1992, "Separation of Film Thickness and Grain Boundary Strengthening Effects in Al Thin Films on Si," J. Mater. Res. **7**, pp. 2040–2048.

Viot P., 2009, "Hydrostatic Compression on Polypropylene Foam," Int. J. Impact Eng., **36**, pp. 975–989.

Wan, J., Fan, Y. L., Gong, D. W., Shen, S .G., and Fan, X. Q., 1999, " Surface Relaxation and Stress of FCC Metals: Cu, Ag, Au, Ni, Pd, Pt, Al and Pb," Modelling Simul. Matr. Sci. Eng., **7**, pp. 189–206.

Wang, Y. and Cuitiño, A. M., 2000, "Three-dimensional nonlinear open-cell foams with large deformations," J. Mech. Phys. Solids, **48**, pp. 961–988.

Wang Y., 2001, *The mechanics of open-cell solid foams: Modelling, simulation, and experiment*, PhD thesis, Rutgers, State University of New Jersy

Wang Y. and Cuitiño, 2002, "Full-field measurements of heterogeneous deformation patterns on polymeric foams using digital image correlation," Int. J. Solid Struct., **39**, pp. 3777–3796.

Warren W. E. and Kraynik A. M., 1987, "Foam mechanics: the linear elastic response of two-dimensional spatially periodic cellular materials," Mech. Mater., **6**, pp. 27–37.

Warren W. E. and Kraynik A. M., 1988, "The linear elastic properties of open foams," Trans. ASME J. Appl. Mech., **55**, pp. 341–346.

Warren, W. E., Kraynik, A. M. and Stone, C.M., 1989, "A constitutive model for two-dimensional nonlinear elastic foams," J. Mech. Phys. Solids, **37**, pp. 717–733.

Warren, W. E. and Kraynik, A. M., 1991, "The nonlinear elastic behavior of open-cell foams," Trans. ASME J. Appl. Mech., **58**, pp. 376–381.

Warren, W. E. and Kraynik, A. M., 1997, "Linear elastic behavior of a low-density Kelvin foam with open cells," Trans. ASME J. Appl. Mech., **64**, pp. 787–794.

Wissuchek, D. J., Mackin, T. J., DeGraef, M., Lucas, G. E. and Evans, A. G., 1996, "A simple method for measuring surface strains around cracks," Exp. Mech., **36**, pp. 173–179.

Weaire D. and Phelan R., 1994, "A counterexample to Kelvin's conjecture on minimal surfaces," Phil. Mag. Lett., **69**, pp. 107–110.

Wearie D. and Hutzler S., 1999, *The physics of foams* (Clarendon press, Oxford).

Yongqi, S., Corletto, C., Bradley, W. L., and Tian, J., 1996, "Direct measurement of microscopic strain distribution near a crack tip," Exp. Mech., **36**, pp. 193–198.

Zaslawsk, M. l, 1973, "Multiaxial-Stress Studies on Rigid Polyurethane Foam," Exp. Mech., **13**, pp. 70–76.

Zenkert D., Shipsha A. and Persson K., 2004, "Static indentation and unloading response of sandwich beams," Composites: Part B, **35**, pp. 511–522.

Zhang, J., Lin, Z., Wong, A., Kikuchi, N., Li, V. C., Yee, A. F. and Nusholtz, G. S., 1997, "Constitutive Modeling and Material Characterization of Polymeric Foams," Trans. ASME J. Eng. Maters. Tech., **119**, pp. 284–291.

Zhang, D., Zhang, X. and Cheng, G., 1999, "Compression strain measurement by digital speckle correlation," Exp. Mech., **39**, pp. 62–65.

Zhou, J., Gao, Z., Cuitiño, A. M. and Soboyejo, W. O. 2004, "Effects of heat treatment on the compressive deformation behavior of open cell aluminum foams," Mater. Sci. Eng., **386**, pp. 118–128.

Zhou J, Gao Z, Cuitiño A. M. and Soboyejo, W. O. 2005, "Fatigue of As-fabricated open cell aluminum foams," Trans. ASME J. Eng. Maters. Tech., **127**, pp. 40–45.

Zhou, J., Gao, Z., Allameh, S., Akpan, E., Cuitiño A. M. and Soboyejo, W. O. 2005, "Multiscale Deformation of Open Cell Aluminum Foams," Mech. Adv. Mater. Struct., **12**, pp. 201–216.

Zhu, H. X., Knott, J. F. and Mills, N. J., 1997, "Analysis of the Elastic Properties of Open-Cell Foams with Tetrakaidecahedral Cells," J. Mech. Phys. Solids, **45**, pp. 319–343.

Zhu, H. X., Hobdell, J. R. and Windle, A. H., 2000, "Effects of cell irregularity on the elastic properties of open-cell foams," Acta Materialia, **48**, pp. 4893–4900.

Zhu, H. X., Windle A. H., 2002, "Effects of cell irregularity on the high strain compression of open-cell foams," Acta Materialia, **50**, pp. 1041–1052.

Zhu, H. X., Hobdell J. R. and Windle A. H., 2001, "Effects of cell irregularity on the elastic properties of 2D Voronoi honeycombs," J. Mech. Phys. Solids, **49**, pp. 857–870.

Zhu, H. X., Thorpe, S. M. and Windle A. H., 2006, "The effect of cell irregularity on the high strain compression of 2D Voronoi honeycombs," Int. J. Impact Eng., **43**, pp. 1061–1078.